Leakage Current and Resistive Switching Mechanisms in $SrTiO_3$

Shahin Ameiryan Mojarad

Doctor of Philosophy

Submitted in partial fulfilment of the requirements for the degree of
Doctor of Philosophy in Electrical and Electronic Engineering

August 2013

Abstract

Resistive switching random access memory devices have attracted considerable attention due to exhibiting fast programming, non-destructive readout, low power-consumption, high-density integration, and low fabrication-cost. Resistive switching has been observed in a wide range of materials but the underpinning mechanisms still have not been understood completely.

This thesis presents a study of the leakage current and resistive switching mechanisms of $SrTiO_3$ metal-insulator-metal devices fabricated using atomic layer deposition and pulse laser deposition techniques. First, the conduction mechanisms in $SrTiO_3$ are investigated. The leakage current characteristics are highly sensitive to the polarity and magnitude of applied voltage bias, punctuated by sharp increases at high field. The characteristics are also asymmetric with bias and the negative to positive current crossover point always occurs at a negative voltage bias. A model comprising thermionic field emission and tunnelling phenomena is proposed to explain

the dependence of leakage current upon the device parameters quantitatively.

$SrTiO_3$ also demonstrates bipolar switching behaviour where the current-density versus voltage (*J*-*V*) characteristics show asymmetry at all temperatures examined, with resistive switching behaviour observed at elevated temperatures. The asymmetry is explained by the relative lack of electron traps at one electrode, which is determined from the symmetric *J*-*V* curve obtained at room temperature due to the redistribution of the dominant electrical defects in the film. Evidence is presented for a model of resistive switching that originates from defect diffusion (possibly oxygen vacancies) at high temperatures.

Finally, a peculiar resistive switching behaviour was observed in pulse laser deposited $SrTiO_3$. This switching depends on both the amplitude and polarity of the applied voltage, and cannot be described as either bipolar or unipolar resistive switching. This behaviour is termed antipolar due to the opposite polarity of the set voltage relative to the previous reset voltage. The proposed model based on electron injection by tunnelling at interfaces and a Poole-Frenkel mechanism through the bulk is extended to explain the antipolar resistive switching behaviour. This model is quantified by use of a simple mathematical equation to simulate the experimental results.

Acknowledgments

I would like to thank my supervisors Prof. Anthony O'Neill and Dr. Jonathan Goss for all their guidance, support and patience. I have been privileged to work under their supervision, and I truly appreciate their infinite help and encouragement.

In addition, special thanks to Mrs. Gillian Webber for her kindness, administrative support and help. And a thank you to our school receptionist Deborah Alexander, for her nice personality and sense of humour. I would also like to thank all my friends who made my PhD journey a pleasant one, those who are in my heart and not on paper. I want to express acknowledgement to the EPSRC for providing the necessary funds during my PhD and School of Electrical and Electronic Engineering and Newcastle University for their generous financial support through numerous awards and scholarships. I would like to express my gratitude to Len Shaw for helping me with the details that only a sharp eye could spot.

I am grateful to my Aunt and Uncle, Tahereh and Reza, for their kindness and constant support during my studies. Last but not least, I would like to thank my beloved parents and sister for their never-fading love, support and encouragement.

Contents

Abstract . . . . . **i**

Acknowledgements . . . . . **iii**

Contents. . . . . **iv**

List of Published Papers . . . . . **vii**

List of Tables . . . . . **viii**

List of Figures . . . . . **ix**

Chapter 1 **Introduction** **1**

Chapter 2 **Resistive switching memory**. **6**

2.1 Introduction 6

2.2 Resistive switching RAMs. 11

2.3 History 14

2.4 Resistive switching mechanisms 16

2.4.1 Electro-chemical mechanism 17

2.4.2 Valence-change mechanism 18

2.4.3 Thermo-chemical mechanism 21

2.5 Strontium titanate 23

2.6 Fabrication 24

2.6.1 Atomic layer deposition 24

2.6.2 Pulse laser deposition 26

2.7 Characterisation. 27

2.7.1 X-ray diffraction 27

2.7.2 X-ray photoelectron spectroscopy 28

2.7.3 *J*–*V* characterisation 29

2.7.4 Conductive atomic force microscopy. 30

2.8 Conclusions 31

Chapter 3 **Conduction mechanisms 32**
3.1 Introduction 32
3.2 Thermionic emission theory 34
3.3 Quantum tunnelling theory 35
3.4 Interface conduction mechanisms 36
3.4.1 Schottky emission. 36
3.4.2 Fowler-Nordheim tunnelling 40
3.5 Bulk conduction mechanisms 41
3.5.1 Poole-Frenkel emission 41
3.5.2 Trap-assisted-tunnelling 44
3.6 Leakage current modelling 45
3.6.1 Thermionic-emission vs. tunnelling 46
3.6.2 Schottky vs. Poole-Frenkel 48
3.6.3 Fowler-Nordheim vs. trap-assisted-tunnelling . . .49
3.7 Conclusions 50
Chapter 4 **Leakage current behaviour of $SrTiO_3$ 51**
4.1 Introduction 51
4.2 Experiment 55
4.3 Electrical results 56
4.4 Modelling the leakage current 57
4.5 C-AFM 66
4.6 Positive charge trapped at the interface 68
4.7 Conclusions 70
Chapter 5 **Bipolar behaviour of $SrTiO_3$ 71**
5.1 Introduction 71
5.2 ALD $SrTiO_3$ 73
5.2.1 Electrical results 73
5.2.2 Modelling the bipolar behaviour 74
5.2.3 Trap states of oxygen vacancies 80
5.2.4 Activation energy of oxygen vacancies 83
5.3 PLD $SrTiO_3$ 86
5.3.1 Experiment. 87
5.3.2 Electrical results 88
5.3.3 Modelling. 90
5.3.4 Carbon as a positive charge trapped 94
5.3.5 C-AFM 98
5.4 Conclusions 100

Chapter 6 **Antipolar behaviour of $SrTiO_3$ 101**
6.1 Introduction 101
6.2 Experiment 105
6.3 Electrical results 106
6.4 Modelling the antipolar resistive switching 110
6.5 Charge movement calculation 115
6.6 Antipolar modelling results. 118
6.7 Schottky and Poole-Frenkel behaviour 123
6.8 Origin of antipolar resistive switching 126
6.9 Three-state RRAM 131
6.10 Conductions 133
Chapter 7 **Summary 134**
Appendix A **Resistive Switching periodic table 139**
References 143

List of Published Papers

Oxygen vacancy migration in compressively strained $SrTiO_3$
R. A. S. Al-Hamadany, J. P. Goss, P. R Briddon, S. A. Mojarad, Meaad Al-Hadidi, M. J. Rayson and A. O'Neill, *J. Appl. Phys*. 113, art. No. 024108 (2013).

Diffusion of oxygen vacancies in ferroelectric and anti-ferroelectric [001]-strained $SrTiO_3$
R.A. S. AL-Hamadany, J. P. Goss, S. A. Mojarad, M. AL-Hadidi, P. Briddon, A. O'Neill and Mark. J. Rayson, *Ferroelectrics UK 2013*, 17-18 January 2013, University of Sheffield, Sheffield, UK.

Anomalous resistive switching phenomenon
S. A. Mojarad, J. P. Goss, Kelvin S. K. Kwa, Peter K. Petrov, Bin Zou, Neil Alford and A. O'Neill, *J. Appl. Phys*. 112, art. No. 124516 (2012).

Leakage current asymmetry and resistive switching behaviour of $SrTiO_3$
S. A. Mojarad, J. P. Goss, K. S. K. Kwa, Z. Zhou, R. A. S. Al-Hamadany, D. J. R. Appleby, N. K. Ponon and A. O'Neill, *Appl. Phys. Lett.* 101, art. No. 173507 (2012).

A comprehensive study on the leakage current mechanisms of $Pt/SrTiO_3/Pt$
S. A. Mojarad, K. S. K. Kwa, J. P. Goss, Z. Zhou, N. K. Ponon, D. J. R. Appleby, R. A. S. Al-Hamadany and A. O'Neill, *J. Appl. Phys*. 111, art. No. 014503 (2012).

Microscopic investigations of oxygen vacancy migration in strained $SrTiO_3$
R. A. S. AL-Hamadany, J. P. Goss, S. A. Mojarad, M. AL-Hadidi, P. Briddon, A. O'Neill and M. J. Rayson, *19th Workshop on Oxide Electronics*, Septermber 30-October 3, 2012, Paleis't Loo, Apeldoorn, Netherlands.

Remote Plasma Atomic Layer Deposition of Strontium Titanate Films Using $Sr(iPr_3CP)_2$ and $Ti(OiPr)_4$
G. Dilliway, M. Oliver, K. Kwa, Z. Zhou, S. A. Mojarad, J. Goss and A. O'Neill, *219th ECS meeting abstract* (2011).

List of Tables

Chapter 2

2.1 Comparison of SRAM, DRAM, Flash and RRAM [17]. **8**

2.2 Elements that have been used as electrodes (blue), and those whose oxides have demonstrated bipolar (red) and unipolar (yellow) resistive switching behaviour. **13**

Chapter 3

3.1 The main conduction mechanisms of MIM structures. **33**

Chapter 4

4.1 Calculated parameters used in Equation 4.6. . . . . **65**

Chapter 6

6.1 Characteristics of bipolar, unipolar and antipolar resistive switching in terms of the conditions required to set the devices to the low resistance state, and reset to the high resistance state. . **104**

Appendix A

A.1 Elements that have been used as electrodes (blue), and those whose oxides have demonstrated bipolar (red) and unipolar (yellow) resistive switching behaviour. **139**

A.2 Bipolar and unipolar resistive switching behaviour in different oxides. **140**

List of Figures

Chapter 2

2.1 (a) Classification of semiconductor memory. (b) Capacity of memory fabs by segments (SEMI World Fab Database Reports, Sept. 2011). **7**

2.2 Characteristics of semiconductor memory [15]. **7**

2.3 The crossbar architecture of RRAM [23] and typical RRAM cell. **11**

2.4 (a) Bipolar and (b) unipolar behaviour of resistive switching. **12**

2.5 (a) Negative resistance in $Al/Al_2O_3/Al$ [25]; (b) the memristor as the fourth missing circuit element [28]. **14**

2.6 Proposed resistive switching mechanisms [32]. **16**

2.7 (a) Initial state of insulator; (b) growth of conductive filament; (c) formation of conductive filament; (d) rupture of conductive filament. **17**

2.8 Cell structure in the valence-change mechanism when the cell is in (a) the high resistance state and (b) low resistance state. **19**

2.9 Resistive switching behaviour in the valence-change mechanism. **20**

2.10 Formation process by increasing the voltage to higher values until the current suddenly increases which is limited by current compliance (CC). **21**

2.11 Resistive switching behaviour in the thermo-chemical mechanism. **22**

2.12 Perovskite structure of $SrTiO_3$. **23**

2.13 Schematic illustration of the deposition cycle in ALD growth: (a) exposure to the first precursor, (b) purge of residual precursors from the reaction chamber, (c) exposure to the second precursor, and (d) evacuation of the reaction chamber; (e) deposited thin films with the desired thickness. **25**

2.14 Scheme of pulse laser deposition. **26**

2.15 The interference of the photons from the crystal planes. **27**
2.16 Illustration of an XPS instrument. **28**
2.17 (a) Picture of probe station; (b) top and bottom electrodes; (c) *J-V* characteristics of MIM structure; (d) sweeping the voltage on top electrode. **29**
2.18 Illustration of the C-AFM apparatus. **30**

Chapter 3

3.1 Electron penetration through a rectangular potential barrier. **35**
3.2 Formation of Schottky barrier when a metal is in contact with an insulator. **37**
3.3 Effect of external electric field on the Schottky barrier of a metal and semiconductor interface. **38**
3.4 (a) Step potential and (b) the effect of strong electric field on the step potential barrier which might result in carriers tunnelling through the barrier. **40**
3.5 The effect of external electric field on the potential barrier between the trap state and the conduction band. **42**
3.6 (a) Trapped electrons in trap states below the conduction band; (b) electron escaping from the trap state to the conduction band in a weak electric field (Poole-Frenkel); (c) electron tunnelling from trap state to the conduction band in a strong electric field (trap-assisted-tunnelling). **44**
3.7 (a) Modelling the MIM device by three regions where the leakage current can be attributed to either (b) interface or (c) bulk. **45**
3.8 (a) *J-E* characteristics of thermionic emission (blue) and tunnelling mechanism (red); (b) ln(*J*) vs $\sqrt{E}$ where the thermionic emission curve shows linearity; (c) ln(*J*) vs *1/E* where the tunnelling curve is linear. **47**
3.9 (a) Increasing the leakage current by temperature; (b) Arrhenius plot of leakage current in different electric fields. **48**
3.10 The potential that electrons are face in: (a) Schottky; (b) Poole-Frenkel. **49**

Chapter 4

4.1 Scheme of thermionic field emission of electrons (a) between the oxygen vacancies in bulk that can be modelled by Poole-Frenkel emission equation, and (b) over the effective Schottky barrier that can be modelled by the Schottky emission equation. **52**
4.2 The XRD results of $SrTiO_3$ before and after 600 °C annealing. .**55**
4.3 *J–E* characteristics of Pt/$SrTiO_3$/Pt structure for both negative and positive voltage biases over temperature range 300 K to 380 K. .**56**
4.4 Schematic of leakage current mechanisms through $SrTiO_3$. **58**

4.5 Extracting the parameters of Poole-Frenkel equations in the temperature range of 300–380 K from ln(*J*) vs 1/E (Poole-Frenkel plot). **59**
4.6 Extracting the parameters of trap-assisted-tunnelling equations in the temperature range of 300–380 K from ln(*J*) vs 1/E (trap-assisted-tunnelling plot). **60**
4.7 The calculated values of *A* as a function of 1/kT. **61**
4.8 The relationship between the electric field and tunnelling current which shows how the injection of electrons to the vacancies is changed by electric field. **63**
4.9 (a) Results of experimental matching based on Equation 4.6 at negative and positive voltage. (b) Negative voltage bias at top electrode and low injection of electrons to the bottom electrode due to high distance of oxygen vacancies from bottom electrode. (c) Positive voltage bias at top electrode and high injection of electrons to vacancies due to small distance between oxygen vacancies and bottom electrode. **65**
4.10 (a) The current image of SrTiO3 surface, showing filamentary conduction through the film. (b) The topography image. **66**
4.11 (a) Schematic path of leakage current through the aligned oxygen vacancies. (b) *I–V* characteristic of a single-point by sweeping the voltage on top of leaky and non-leaky points. **67**
4.12 Different direction of current where the minimum of leakage current lie at negative voltage. **68**

Chapter 5

5.1 *J–V* characteristics for the $SrTiO_3$ MIM structures from 280 to 400 K. **73**
5.2 Illustrations of conduction mechanism under different voltage polarities. **74**
5.3 A model for the displacement of oxygen vacancies near the bottom electrode interface under an applied voltage at low temperature. **75**
5.4 A model for the migration of oxygen vacancies near the bottom electrode interface under an applied voltage at high temperature relative to the onset of migration of oxygen vacancies. **76**
5.5 The leakage-current density at +4 V during the temperature variation from 300 K→400 K→300 K. **77**
5.6 The leakage current at 300 K before and after the annealing cycle, and at the peak temperature of 400 K. Inset are illustrations of the model involving oxygen vacancies in relation to the bottom electrode. **78**
5.7 Oxygen vacancies locations in relation to the bottom electrode before and after annealing cycle. **79**
5.8 (a) The Arrhenius plot for figure 5.1 at voltage −4 and +4 V. (b) The activation energy plot. **81**

5.9 Effect of temperature on the leakage current density after annealing the MIM device at 400 K under a positive dc bias of +4 V. **83**
5.10 The leakage current variation by increasing temperature when the voltage of −4 V is applied on top electrode. **84**
5.11 The sample sturture of 13 nm PLD $SrTiO_3$. **87**
5.12 *J–V* characteristics for the 13 nm $SrTiO_3$ MIM structure at 300 K. **88**
5.13 *J–V* charactersitics of $SrTiO_3$ for 50 consecutive sweeping loops. **89**
5.14 A model for the migration of oxygen vacancy near the bottom electrode interface when the voltage is swept from zero to positive values. **91**
5.15 Migration of oxygen vacancy away from the bottom electrode interface when the voltage is swept from positive values to zero.**92**
5.16 XPS depth profile result through the $SrTiO_3$ and Pt bottom electrode. **94**
5.17 (a) Absence and (b) presence of carbon contamination at the bottom electrode interface. **95**
5.18 Illustration of oxygen vacancies migration only at the bottom electrode. **97**
5.19 *J–V* characteristics for the SrTiO3 MIM structures from 280 to 400 K. **98**
5.20 The electrical resistance of individual leaky and non-leaky points by sweeping the voltage from −10 V and +10 V. **99**

Chapter 6

6.1 Schematic representations of the ideal *I–V* and *R–V* hysteresis behaviour of (a) bipolar resistive switching (b) unipolar resistive switching, and (c) antipolar resistive switching. **103**
6.2 The sample sturture of 25 nm PLD $SrTiO_3$. **105**
6.3 *J-V* characteristics of $SrTiO_3$ for 100 consecutive sweeping loops between –3 and +3 V. **106**
6.4 The *I–V* characteristcs in the antipolar resistive switching behaviour of the Pt/$SrTiO_3$/Pt MIM structure. **107**
6.5 Current-density–voltage characteristics for 25 cycles under different conditions: positive bias (red curves), negative bias (green curves) and $-1 < V < +1$ V (blue curves). **108**
6.6 Confirmation of the resistive state in each case from Figure 6.5 via variation of the bias in the $-0.2 < V < +0.2$ V range, as described in the text. **109**
6.7 The electron injection (a) from an electrode to the bulk and (b) from the bulk to the opposite electrode at different voltage polarities. **112**

6.8 A simple model with square barriers between the oxygen vacancies and interfaces. **113**
6.9 Two fixed point charges of q_1 and q_5 *which* confine three mobile charges of q_2, q_3 and q_4. . . . . **115**
6.10 The optimum location of mobile point charge of (a) q_2, (b) q_3, and (c) q_4 where the resultant force on the point charge is minimum. **117**
6.11 Schematic of the location of the deep traps within the oxide film under different voltage biases. **118**
6.12 The varition of injection current due the movement of oxygen vacancies. **119**
6.13 Specification of the injection probability, Pinjection, as a function of the bias magnitude and polarity. **120**
6.14 The simulation results based on the calculated values of $P_{\text{injection}}$. **121**
6.15 Scheme movement of oxygen vacancies through the $SrTiO_3$ at different voltage bias by including the threshold values. **122**
6.16 The resistive switching behaviour of metal oxides when oxygen vacancies act as the (a) mobile donors and (b) mobile traps. . . . **124**
6.17 (a) Migration of oxygen vacancies near the top and bottom electrode interfaces. (b) Low concentration of oxygen vacancies near the electrodes which might be originated from the carbon contamination at the interfaces. **127**
6.18 Modelling the MIM structure by two memristors of M_{BE} and M_{TE} (representing two interfaces) and R_{Bulk} which represents bulk resistance. **128**
6.19 (a-d) Schematic of different states of MIM structure which depend on the resistance states of top and bottom electrodes. (e) The antipolar resistive switching of MIM structure originating from migration of oxygen vacancies in vicinity of the top and bottom electrode interfaces. **130**
6.20 Three stable states of RRAM: (a) low resistance state, (b) positive high resistance state, and (c) negative high resistance state. . . . **132**

Chapter 7

7.1 Summary of the study on leakage current and resistive switching mechanisms of $SrTiO_3$. **135**

Chapter 1

Introduction

> *'All of physics is either impossible or trivial. It is impossible until you understand it, and then it becomes trivial'*
>
> *Ernest Rutherford*

In modern silicon-based technology, the dimensions of metal-oxide-semiconductor field effect transistors (MOSFETs) have been rapidly scaled down due to the increased demand for faster circuit speed, higher packing density, and lower power dissipation. The density of transistors on chips has doubled about every 18-24 months, as predicted by Moore's Law in 1965 [1]. In order to keep up with the required continuing performance enhancements through the scaling of the dimensions of devices [2, 3], the thickness of silicon dioxide must be also reduced. However, in the mid-1990s, the thickness of silicon dioxide reached its critical level of < 2 nm [4], where a high leakage of current occurs due to quantum mechanical tunnelling. It was proposed that this physical limitation could be solved by using metal oxides with high dielectric constants (high-k), which would allow the scaling of the MOSFET with a much larger dielectric thickness [5], but smaller effective oxide thickness (EOT).

However, although larger dielectric thicknesses solved the physical quantum tunnelling limitation, there was still a high leakage of current due to the poor quality of the metal oxide used [6, 7]. The leakage of current through metal oxides was then actively investigated and different models were proposed to explain it [8]. These models helped in understanding the impact of different parameters such as film thickness, electrode materials and annealing temperature on the leakage current. Fabrication methods were substantially improved [9, 10] and finally, in 2007, the first 45 nm commercial microprocessor using a high-k dielectric was fabricated by Intel.

While metal oxides were most actively pursued for gate stack applications from 1995 to 2006, a resistive switching phenomenon was frequently observed. This caused renewed interest in and funding for research into metal oxides. The resistive switching phenomenon occurs in materials which switch between two stable resistivity states upon the application of different voltages [11].

The resistive switching phenomenon can be exploited in non-volatile memory devices, which are called resistive switching random access memories (RRAMs) [12]. The basic component of RRAM is a metal/insulator/metal (MIM) structure, where the insulator is typically made of metal oxide materials. The current-density–voltage (J–V) characteristics of devices exhibit pronounced hysteresis behaviour due to the change in resistance of metal oxides caused by sweeping the

voltage. In order to improve the reliability of RRAM, the underpinning conduction mechanisms of the leakage current through MIM devices must be elucidated.

In this thesis, the conduction mechanisms of $SrTiO_3$, which is one of the promising materials for high-k and RRAM applications are investigated. The leakage of current through the $SrTiO_3$ had been investigated and at low voltages the *J*–*V* characteristics showed very low leakage which increased abruptly when the voltage was increased. By investigating previous models, it has been realised that the abrupt transition in *J*–*V* characteristics can be modelled using the tunnelling equations where the relationship between the current-density and voltage is given by:

$$J \sim \exp\left(-\frac{1}{V}\right) \tag{1.1}$$

However the leakage current increases with temperature, which could not be explained by the tunnelling equations alone, as they are independent of temperature. This counterintuitive observation suggests that the leakage current is simultaneously controlled by both thermionic and tunnelling emission. A model was developed based on the combination of thermionic and tunnelling equations which could be used to precisely model the observed *J*–*V* characteristics of $SrTiO_3$.

An observation of bipolar resistive switching behaviour led to the consideration of $SrTiO_3$ as having potential for RRAM applications. The bipolar behaviour of the *J*–*V* characteristics was elucidated using the previous model which developed to explain the conduction mechanism of $SrTiO_3$.

The leakage of current through $SrTiO_3$ fabricated by the pulsed laser deposition technique was also investigated. The *J–V* characteristics showed resistive switching behaviour, which was first thought to be unipolar behaviour. Further analysis of the hysteresis curves proved that the resistive switching of $SrTiO_3$ cannot be grouped as the either unipolar or bipolar. A third category was therefore introduced called antipolar resistive switching which can be explained by the conduction mechanisms proposed previously.

This thesis aims to elucidate the underpinning mechanisms of leakage current and the bipolar and antipolar behaviour of $SrTiO_3$. Chapter 2 discusses metal oxide materials. The background of the study is explained and the concept of resistive switching presented, along with an overall view of the materials which demonstrate resistive switching behaviour. The main conduction mechanisms in resistive switching are also explained.

In chapter 3 leakage current mechanisms are reviewed. The physical concepts and conduction equations are described, and a conventional method of leakage current modelling is presented.

Chapter 4 is devoted to the modelling of leakage current in $SrTiO_3$. The *J–V* characteristics of $SrTiO_3$ are presented. The conduction equation is derived and explained in detail.

Chapter 5 deals with the bipolar behaviour of $SrTiO_3$, firstly giving an introduction to previous models. The bipolar *J*–*V* characteristics of $SrTiO_3$ are presented and an experiment conducted to examine the model explained.

The antipolar behaviour of $SrTiO_3$ is introduced in chapter 6. The *J*–*V* hysteresis curves of $SrTiO_3$ are compared with bipolar and unipolar behaviour. A simple mathematical model is proposed based on the concepts introduced in the model proposed in chapter 4. Finally the summary of the study is presented in chapter 7.

Chapter 2

Resistive Switching Memory

'Without memory, there is no culture. Without memory, there would be no civilization, no society, no future.'

Elie Wiesel

2.1 Introduction

Semiconductor memory plays a crucial role in today's electronic devices. Many of them, and in particular mobile devices, require high-speed, high-density and low-power memory for faster and longer performance. Figure 2.1(a) shows the classification of semiconductor memory into read write memory (RWM), non-volatile RWM (NVRWM) and read only memory (ROM). RWM can be divided into two groups: random access memory (RAM) and non-random access memory. The former include dynamic RAM (DRAM) or static RAM (SRAM), and examples of the latter is shift register. In NVRWM the information stores even when the power supply is disconnected such as FLASH and erasable programmable ROM (EPROM) [13]. An example of ROM is one-time programmable ROM (OTPROM) where data stored cannot be modified [14].

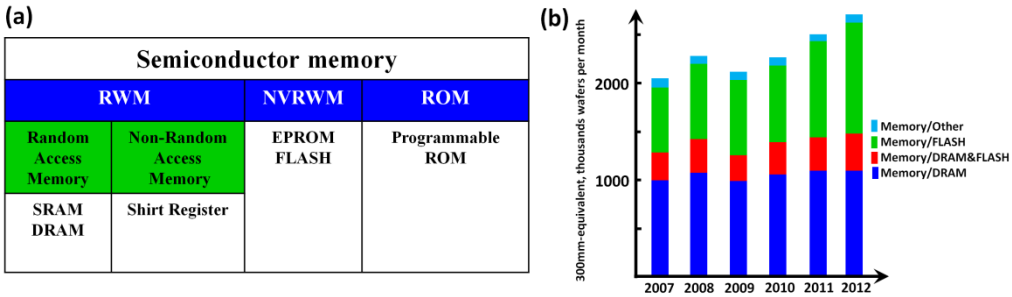

Figure 2.1: (a) Classification of semiconductor memory. (b) Capacity of memory fabs by segments (SEMI World Fab Database Reports, Sept. 2011).

DRAM and Flash memory devices constitute the biggest share of the semiconductor memory market (Figure 2.1(b)). SRAM is also widely used in microprocessors as fast access memory. An SRAM cell is constructed using six MOSFETs, as shown in Figure 2.2(a). The four MOSFETs in the middle (M1 to M4)

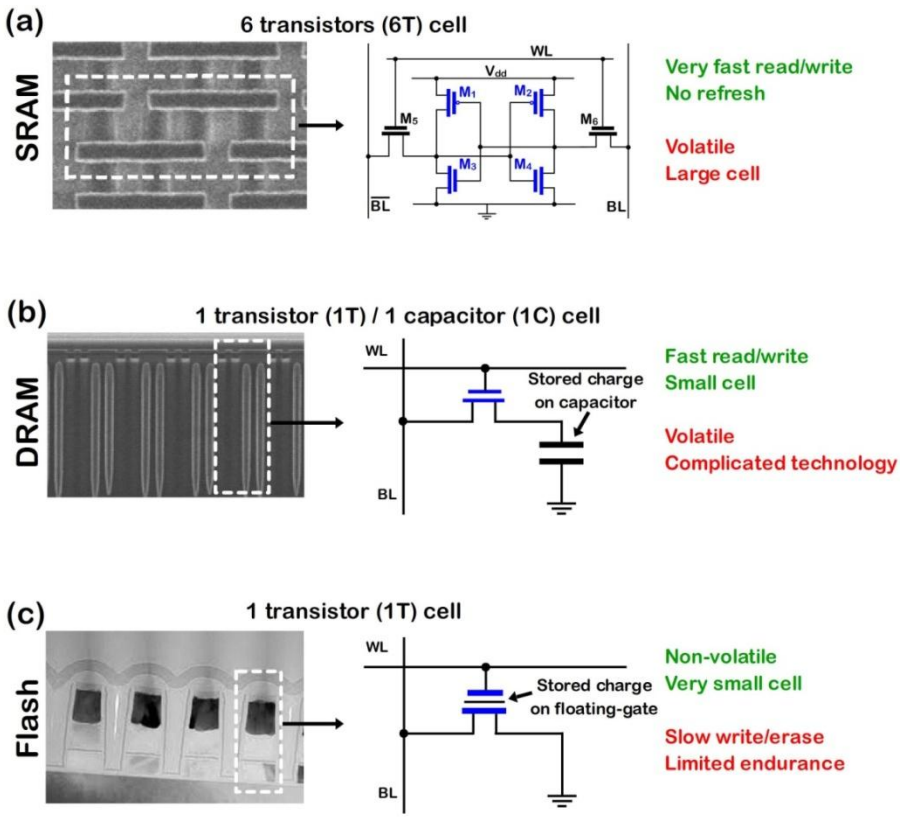

Figure 2.2: Characteristics of semiconductor memory [15].

form two cross-coupled inverters with two stable states, representing the digits '0' and '1'. The state of one cell is immediately available on the bit line (BL) when the word line (WL) is raised (reading). The state of the cell can be changed by setting the BL and $\overline{BL}$ lines to the desired value and then raising WL (writing). SRAM is a very fast type of memory, where the state of one cell can be detected in less than 0.3 ns (Table 2.1). However, SRAM has lower density compared to DRAM and Flash, using 6 transistors for one cell. It is also volatile, and requires constant power (V_{dd}) to maintain the state of each cell.

In DRAM, a cell comprises one transistor and one capacitor as shown in Figure 2.2(b). The transistor serves as a switch which provides access to the state of the capacitor. A charged or uncharged capacitor represents the digits '1' and '0' respectively. In order to read the state of a cell, the WL is raised to switch the transistor to the 'On' state. Then, if the current flows on the BL, the state of the cell is '1' whereas it is '0' when there is no current. A cell is written by raising the WL for an appropriate time to charge or drain the capacitor through the BL.

Table 2.1: Comparison of SRAM, DRAM, Flash and RRAM [16].

	SRAM	DRAM	Flash	RRAM
Cell	6T	1T1C	1T	1T1R or 1D1T
Time of writing to '1'	~0.3ns	<10ns	~1ms	~5ns
Time of erasing to '0'	~0.3ns	<10ns	10-0.1ms	~5ns
Endurance (cycles)	$>10^{16}$	$>10^{16}$	$>10^{5}$	$>10^{10}$
Non-volatility	No	No	Yes	Yes

DRAM is slower than SRAM (see Table 2.1), but it has simpler structure, leading to greater memory density and lower fabrication costs. Therefore, DRAM is used as the main type of memory in electronic devices where high memory capacity is required, while SRAM is only used as the cache in microprocessors where rapid access time is more important. DRAM is also volatile, and due to the leakage of current through the capacitor each cell must be refreshed frequently.

Flash is a non-volatile type of memory which can be used for persistent storage. A typical Flash cell is a floating-gate MOSFET that can be erased electrically (Figure 2.2(c)). The cell represents the states '1' and '0' when the floating-gate is charged and uncharged respectively. Due to the low speed and endurance of Flash relative to DRAM, it cannot be used as the main memory in electronic devices. In addition, Flash has less endurance where the number of write and erase cycles in Flash is about 10^5, whereas in DRAM it is 10^{16} [16].

Although, in electronic devices DRAM and Flash have gained the biggest shares of the semiconductor memory market, their scaling is likely to cause serious limitations in the future. In DRAM the charge on the capacitor must stay constant during scaling, so for high density memory the third dimension is used. This makes the fabrication process complicated which leads to higher fabrication cost. Also, by scaling the capacitor below 30 nm there is a high leakage of current [15]. In the case of Flash, a significant barrier is the requirement to have non-volatile retention, which makes scaling beyond 20 nm challenging [15]. As scaling limitations in mature

memory technologies become serious, new types of memory device have been investigated in the search for a universal memory with the speed of SRAMs and DRAM and the non-volatile properties of Flash as well as smaller size.

Several non-volatile memory technologies have been introduced, such as magnetic RAM [17], spin transfer torque RAM [18], phase change RAM [19], carbon nanotube RAM [20], probe memory [21], single electron memory [22] and RRAM [12].

Among these types of non-volatile memory, RRAM has been considered as one of the most promising due to its excellent scalability. The simple cell structure of RRAM makes the fabrication process uncomplicated, which could lead to lower manufacturing costs. In addition, its write/erase time is much faster than that of conventional non-volatile memory such as in Flash. Table 2.1 compares the specifications of RRAM to other memory devices. This chapter presents an overview of the characteristics of RRAM with a focus on the underpinning resistive switching mechanisms.

2.2 Resistive switching RAMs

A simple RRAM cell is constructed using a MIM structure, where the insulator can switch between two stable resistivity states. The high resistance state represents the digit '0' and the low resistance state represents the digit '1'. Figure 2.3 shows typical RRAM cells which can be arranged in a matrix. The rows and columns of the matrix form WLs and BLs. The state of one cell can switch between high and low resistance by the application of appropriate programming voltage on the WL. The voltage that switches the device to low resistance is called V_{set}, and that which switches the device to high resistance is termed V_{reset}. In order to read the cell, a small voltage is applied to WL and the current through the BL is detected. Depending on the high or low magnitude of the current, the state of the cell can be detected as '1' or '0'

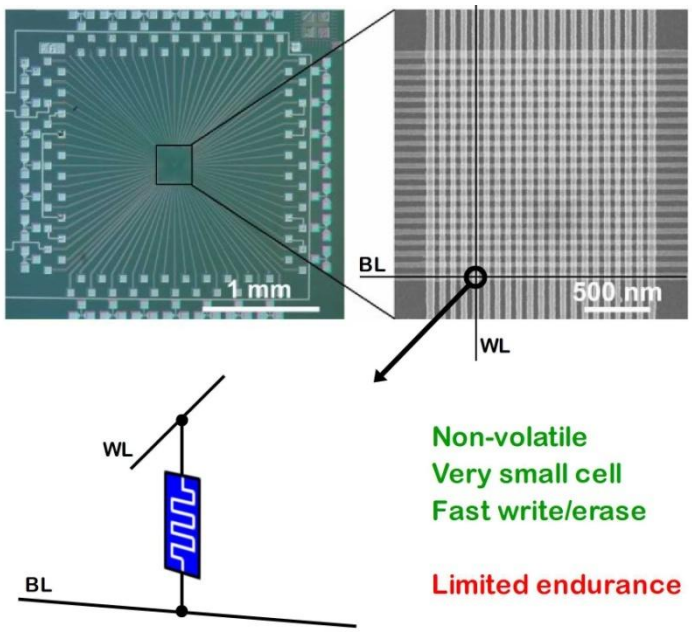

Figure 2.3: The crossbar architecture of RRAM [23] and typical RRAM cell.

respectively. The amplitude of V_{set} and V_{reset} depend upon the properties of the material used. However, the resistive switching behaviour of materials can be categorized into two main groups which are determined based upon the polarity and amplitude of V_{set} and V_{reset}.

The first type of resistive switching behaviour is bipolar, where switching depends upon the polarity of the voltage applied. In this case, the amplitude of V_{set} is almost equal to V_{reset} but with the opposite polarity. Figure 2.4(a) shows an example of bipolar behaviour where a cell can be set to low resistance if $V > V_{set}$ or reset to high resistance if $V < -V_{reset}$.

The second type of resistive switching is termed unipolar, where switching depends only on the amplitude of the voltage, and not the polarity applied. Figure 2.4(b) shows a schematic diagram of unipolar resistive switching, where the resistance of the material can be reset to the high by applying $V_{set} > |V| > V_{reset}$. The low resistance state is then achieved via the application of $|V| > V_{set}$.

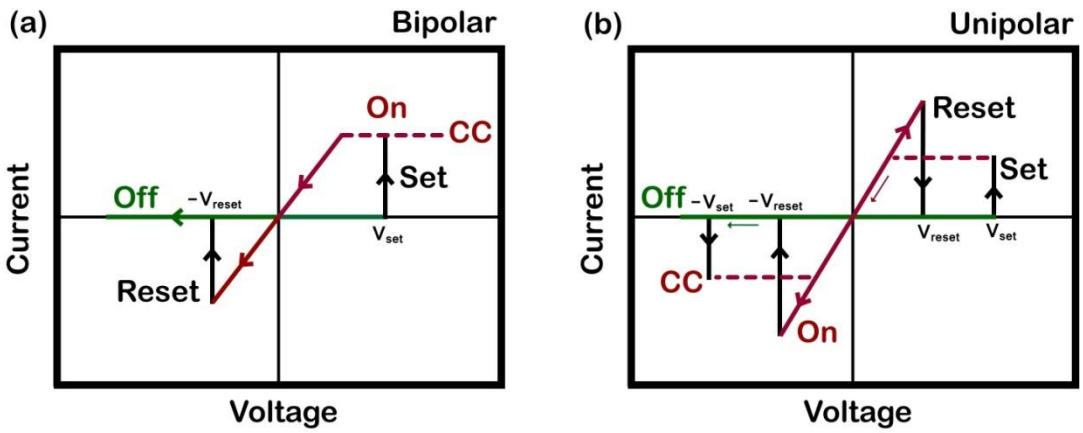

Figure 2.4: (a) Bipolar and (b) unipolar behaviour of resistive switching.

Bipolar and unipolar resistive switching have been observed in a wide range of materials when they have been sandwiched between two electrodes (Appendix A). Table 2.2 shows the elements whose oxides have demonstrated resistive switching. Binary oxides, including NiO, ZnO, Cu_xO, MoO_x, HfO_2, TiO_2, ZrO_2, SnO_2, VO_2, Al_2O_3 and Ta_2O_5, have been reported to show both bipolar and unipolar resistive switching, while perovskite metal oxides such as $BiFeO_3$, $SrZrO_3$, $SrTiO_3$, $BaSrTiO_3$, and $PrCaMnO_3$ have demonstrated more bipolar behaviour. Recently, bipolar behaviour has been also identified in SiO_x, GeO_2 and graphene oxides [24-28].

Table 2.2: Elements that have been used as electrodes (blue), and those whose oxides have demonstrated bipolar (red) and unipolar (yellow) resistive switching behaviour.

Bipolar
Unipolar
Electrode

1 He														
3 Li	4 Be											5 B	6 C	7 N
11 Na	12 Mg											13 Al	14 Si	15 P
19 K	20 Ca	21 Sc	22 Ti	23 V	24 Cr	25 Mn	26 Fe	27 Co	28 Ni	29 Cu	30 Zn	31 Ga	32 Ge	33 As
37 Rb	38 Sr	39 Y	40 Zr	41 Nb	42 Mo	43 Tc	44 Ru	45 Rh	46 Pd	47 Ag	48 Cd	49 In	50 Sn	51 Sb
55 Cs	56 Ba	57-71	72 Hf	73 Ta	74 W	75 Re	76 Os	77 Ir	78 Pt	79 Au	80 Hg	81 Tl	82 Pb	83 Bi

57 La	58 Ce	59 Pr	60 Nd	61 Pm	62 Sm	63 Eu	64 Gd	65 Tb	66 Dy	67 Ho	68 Er	69 Tm	70 Yb	71 Lu

2.3 History

Resistive switching was first reported in aluminium oxide by Hickmott in 1962, who termed it negative resistance [29]. Figure 2.5(a) illustrates the *I–V* characteristics of the MIM structure of $Al/Al_2O_3/Al$ [29] where by increasing the voltage, the current decreases resulting in negative resistance. Nowadays, this behaviour is known as the phenomenon of resistance switching where the $I-V$ characteristics can be interpreted as the resistive switching of aluminium oxide from low to high values by increasing the voltage. Later, similar resistive switching behaviour was observed in NiO [30]. Contemporary research on resistive switching was initiated in 2000, when it was suggested that the reproducible switching effect in $SrTiO_3$:Cr could be practicably developed in the next generation of memory devices [31].

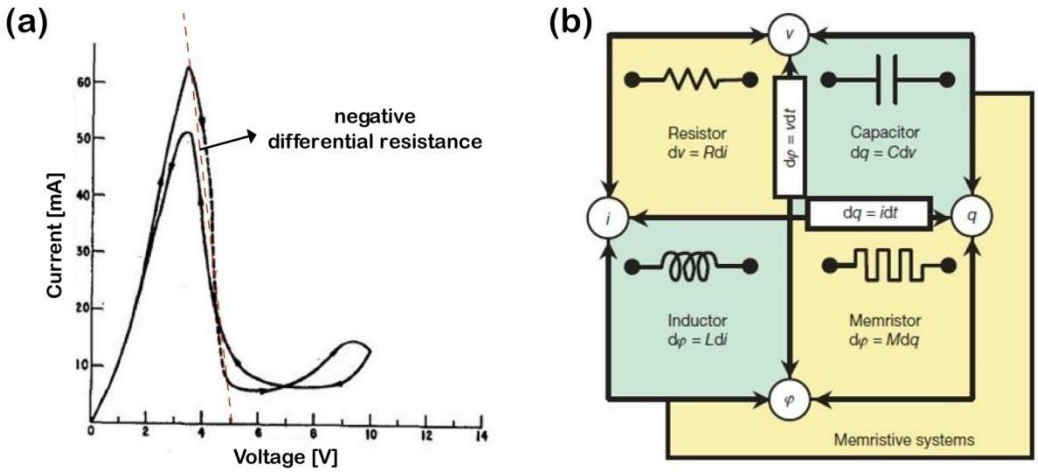

Figure 2.5: (a) Negative resistance in $Al/Al_2O_3/Al$ [29]; (b) the memristor as the fourth missing circuit element [32].

In an completely separate topic, in 1971, Chua predicted the existence of a new circuit element called the memristor (a term constructed from 'memory' and 'resistor') [33]. The four fundamental circuit variables are current (i), voltage (v), charge (q) and flux (φ). Figure 2.5(b) shows the six possible relationships in which these four variables can be paired. Current is a time derivative of charge and voltage is a time derivative of flux. The remaining four relations result in the resistor (R), capacitor (C), inductance (L) and memristor (M). The first three of these are the basic two-terminal circuit elements and Chua predicted the memristor as a fourth circuit element that mathematically connects flux to charge:

$$d\varphi = Mdq. \tag{2.1}$$

Although a relevant physical device had yet to be specified, Chua described the future potential applications of the memristor [33]. In 2008, a physical memristor device was proposed by a group at Hewlett-Packard [32] based on the bipolar resistive switching phenomenon, which led to further renewed interest in resistive switching. During the past five years, the resistive switching phenomenon has not only been extensively investigated for RRAM applications, but it is also considered as having potential in the development of logic devices [34] and for neuromorphic to mimic biological connections in the brain [35].

2.4 Resistive switching mechanisms

The resistive switching properties of materials originate from a large variety of physical and chemical phenomena. However, the mechanisms underpinning resistive switching are still not fully understood. Hence, macroscopic descriptions of resistive switching have been used more often than microscopic modelling, since the latter requires more physical detail and large computational resources.

This section presents details of the electro-chemical, valence-change and thermo-chemical mechanisms which are frequently used in the literature to macroscopically explain the resistive switching phenomenon (Figure 2.6). The electro-chemical and valence-change mechanisms are involved in the bipolar behaviour seen in resistive switching while the thermo-chemical process concerns unipolar behaviour.

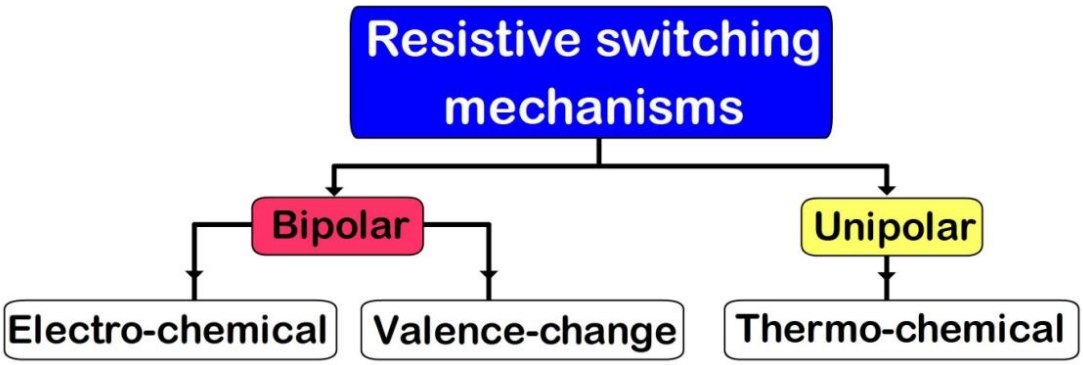

Figure 2.6: Proposed resistive switching mechanisms [36].

2.4.1 Electro-chemical mechanism

In this mechanism, resistive switching is caused by the electrochemical deposition and dissolution of metal cations through the insulator [37]. In this case, the insulator is sandwiched between two electrodes, one of which is an electrochemically active metal such as Cu, Ag or Ni while the other electrode might be Pt, Au, Ir or W [36]. The initial state of the cell is high resistance where no metal is present in the insulator (Figure 2.7(a)). When, a sufficiently positive voltage is applied to the active electrode, the dissolution of the active metal occurs (Figure 2.7(b))

$$M \rightarrow M^{z+} + ze^{-} \tag{2.2}$$

where M is the active metal and M^{z+} refers to the metal cations in the insulator. The

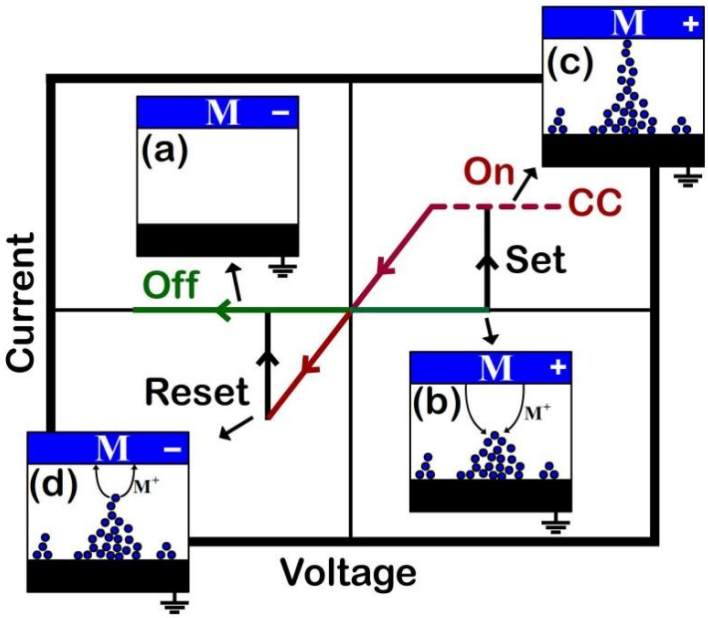

Figure 2.7: (a) Initial state of insulator; (b) growth of conductive filament; (c) formation of conductive filament; (d) rupture of conductive filament.

migration of the M^{z+} through the insulator leads to the formation of a metallic filament which sets the cell to the low resistance state (Figure 2.7(c)). The cell maintains the low resistance state until a sufficient negative voltage is applied, and then the electrochemical dissolution of the metal filaments occurs:

$$M^{z+} + ze^{-} \rightarrow M \tag{2.3}$$

This leads to the rupture of the filament, which resets the cell to the high resistance state (Figure 2.7(d)). This formation and rupture of the metallic filament changes the resistance of the insulator resulting in bipolar resistive switching behaviour.

2.4.2 Valence-change mechanism

In the valence change mechanism, resistive switching occurs by the migration of anions. In most metal oxides, such as Ta_2O_5 [38] and TiO_2 [39], the anions are oxygen ions and their migration might also be described in terms of the motion of the corresponding oxygen vacancies. The migration of oxygen vacancies near one electrode can change the nature of the interface from blocking to Ohmic contact, resulting in resistive switching behaviour.

Figure 2.8(a) shows the cell structure which is constructed from electrodes with high work function such as Pt with two different layers of material in the middle: a layer of stoichiometric oxide such as Ta_2O_5 or TiO_2; and a layer of oxide with missing (represented as ‘x’) oxygen atoms like TiO_{2-x} or Ta_2O_{5-x} [38, 39]. An oxide with a high concentration of oxygen vacancies might be regarded as an n-type

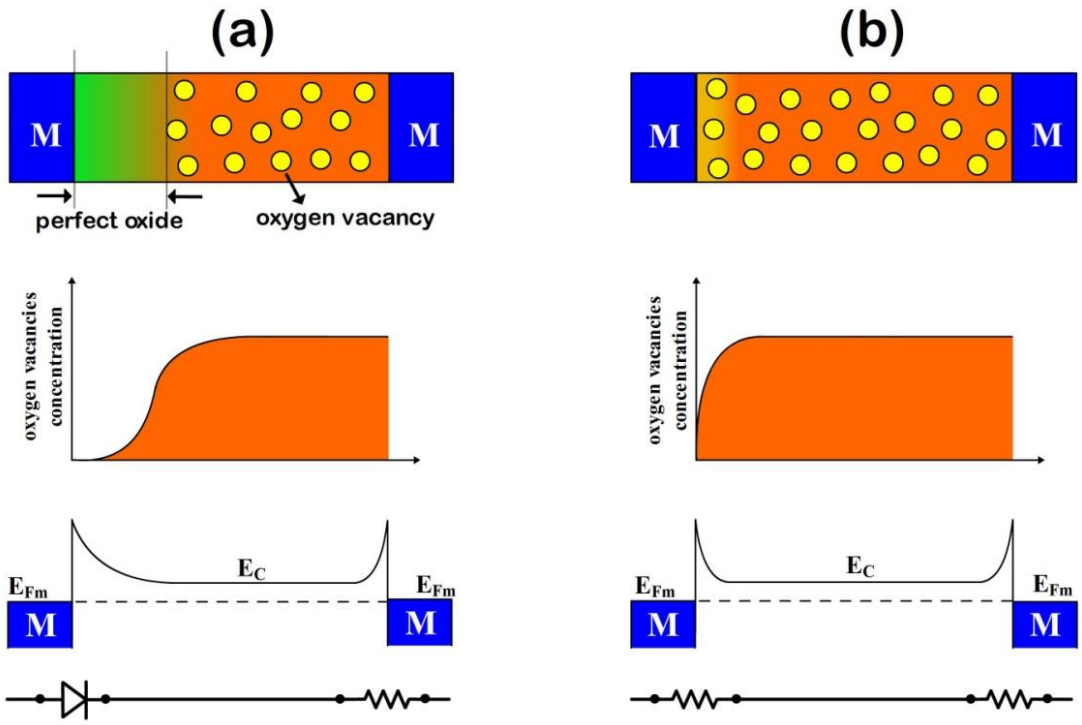

Figure 2.8: Cell structure in the valence-change mechanism when the cell is in (a) the high resistance state and (b) low resistance state.

semiconductor [40], where an Ohmic contact is formed at the interface between the oxide and the metal. The other interface between the metal and the perfect oxide is a Schottky-contact which is also known as the active interface. Therefore, the cell can be modelled as a diode in series with a resistor. This suggests that the *I–V* characteristics can be described by the behaviour of the contacts rather than the bulk of the oxide.

By the application of an appropriate voltage, the active electrode can be switched from Schottky to Ohmic contact by driving the oxygen vacancies into the perfect oxides (Figure 2.8(b)). This increases the concentration of n-carriers near the active interface, which results in narrowing the width of the Schottky barrier. Hence, the

state of the cell can be modelled as two resistors in series. As a result, depending on the concentration of oxygen vacancies near the active electrode, the cell can be in the low or high resistance state respectively.

Figure 2.9 represents an example of the bipolar resistive switching of a cell. When the cell is in the high resistance state, the active interface is in Schottky mode. The application of low voltage at a different polarity would be equivalent to the forward and reverse bias of a diode, which results in low current through the structure. Upon the application of V_{set}, the oxygen vacancies move into the perfect oxide, and this switches the active interface to Ohmic contact. The cell remains at low resistance until a $-V_{reset}$ transforms the interface to Schottky-contact by removing the oxygen vacancies from the perfect oxide.

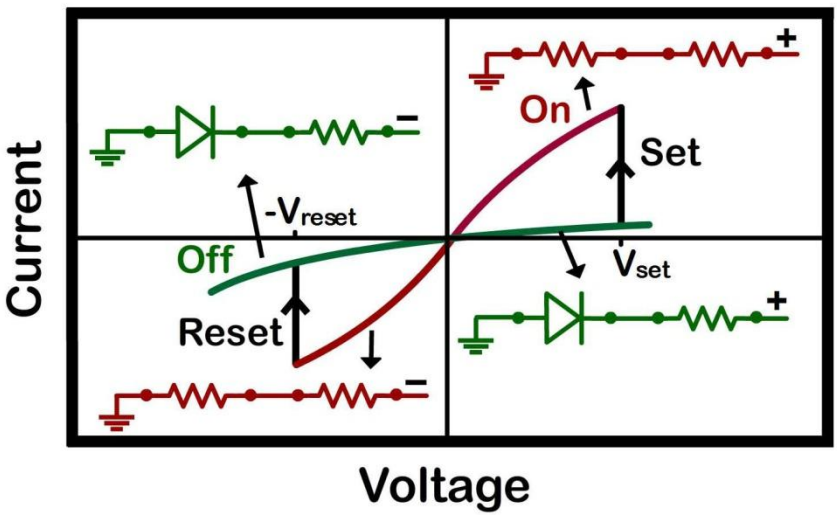

Figure 2.9: Resistive switching behaviour in the valence-change mechanism.

2.4.3 Thermo-chemical mechanism

The thermo-chemical mechanism is primarily based on thermal effects that result in the unipolar behaviour [41]. Resistive switching can then be divided into three steps: electroforming, setting and resetting. Electroforming refers to the initial formation of a conductive filament in the pristine oxide (Figure 2.10(a)). This occurs by increasing the voltage to higher values until the current suddenly increases. During electroforming, large numbers of filaments grow through the oxide due to the electro-migration of oxygen ions (Figure 2.10(b)). Once a conductive bridge connects the top electrode to the bottom electrode (Figure 2.10(c)), a high current flows through the oxide, which must be limited by current compliance to avoid the permanent breakdown of the device.

The formation process is a prerequisite for the generation of conductive filaments, and then the resistive switching occurs due to the rupture and rejuvenation of

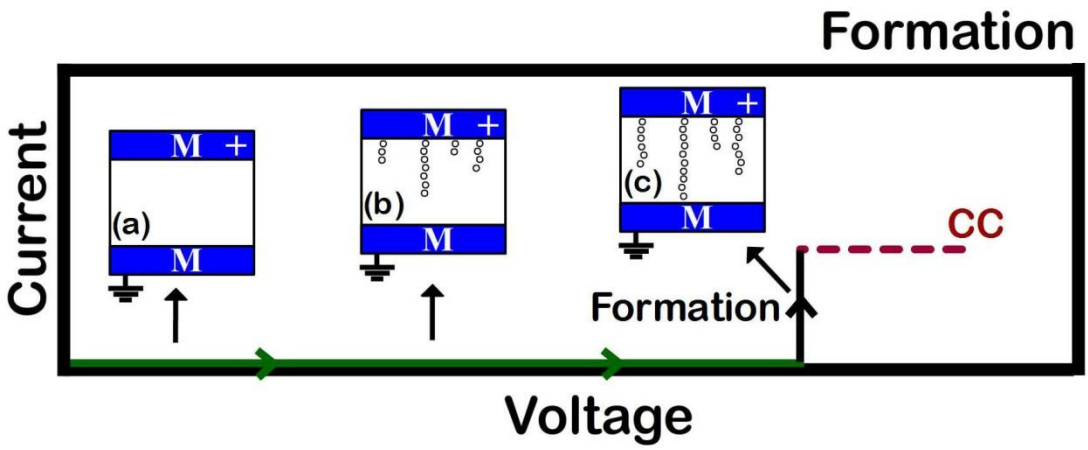

Figure 2.10: Formation process by increasing the voltage to higher values until the current suddenly increases which is limited by current compliance (CC).

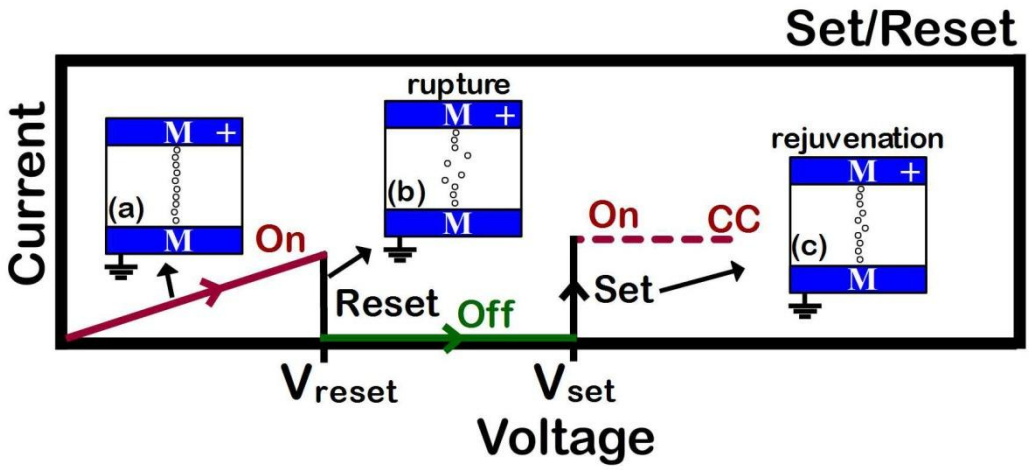

Figure 2.11: Resistive switching behaviour in the thermo-chemical mechanism.

filaments with application of voltage. Figure 2.11(a) shows the initial state of the cell after the formation process. By sweeping the voltage from zero, the high leakage of current through the conductive filaments leads to the local generation of heat. This heat energy results in the thermal dissolution of the conductive filament, which would reset the device to a high resistance state at V_{reset} (Figure 2.11(b)). Now, due to the high resistance of the insulator, the bias voltage would be across the structure which generates a high electric field inside the insulator. By increasing the voltage, the conductive filaments are rejuvenated by the alignment of oxygen vacancies at V_{set} which are driven by electric field (Figure 2.11(c)).

2.5 Strontium titanate

Strontium titanate ($SrTiO_3$) is considered to be an ultra high-k dielectric [42, 43] suitable for application in DRAM [44]. Figure 2.12 illustrates the atomic structure of $SrTiO_3$ which has the general formula of ABO_3. It consists of Sr^{2+} ions on the corners with a Ti^{2+} ion in the centre surrounded by an oxygen octahedron. A high dielectric constant is caused by the displacement of Ti from the centre of the oxygen octahedron which induces a strong electric dipole when it is exposed to an external electric field. In contrast with other perovskite materials such as $PbTiO_3$ or $BaTiO_3$, the ferroelectric properties of $SrTiO_3$ are suppressed by quantum fluctuations at room temperature and they can only be observed at cryogenic temperatures [45, 46]. For RRAM application, $SrTiO_3$ doped with different transition materials has been reported to show bipolar resistive switching behaviour such as $SrTiO_3$:Fe [47, 48], $SrTiO_3$:Cr [49] and $SrTiO_3$:La [50]. Recently, unipolar resistive switching behaviour has also been reported in $SrTiO_3$ [51].

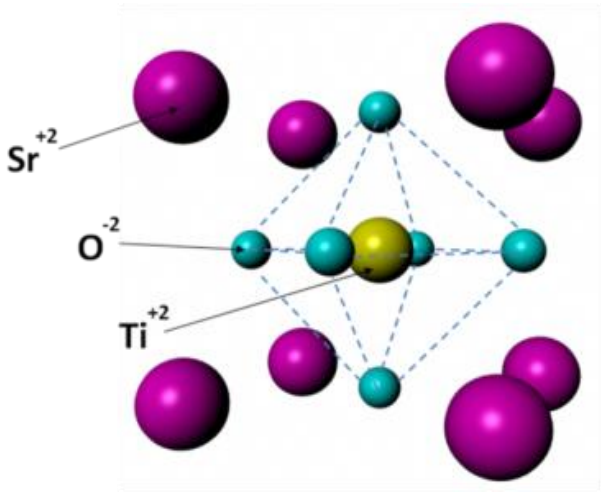

Figure 2.12: Perovskite structure of $SrTiO_3$.

2.6 Fabrication

Various thin film deposition techniques are used to grow a high quality of thin film high-k dielectric, namely thermal evaporation [52], atomic layer deposition [53], metal organic chemical vapour deposition [54], pulsed laser deposition [55], sputtering [56] and molecular beam-epitaxy [57]. In the following section, atomic layer deposition and pulsed laser deposition are explained as the deposition techniques used in this thesis. More detail of fabrication will be presented in the appropriate chapters.

2.6.1 Atomic layer deposition

Atomic layer deposition (ALD) is the preferred growth method used to deposit ultra thin metal-oxide layers, giving excellent control of thickness and reproducibility in film composition [53]. In ALD, the thin film grows due to the surface exchange reaction between the precursor and adsorbed molecules of the reactant. The deposition stops when the surface becomes saturated with the precursors. Hence, the growth rate is independent of precursor dose and can be expressed as the growth per cycle, where each cycle can be defined as having four steps.

The first step involves the introduction of the first precursor to the surface (Figure 2.13(a)). After the formation of a layer, the surface becomes saturated by the precursors. In the next step, residual precursor is evacuated from the chamber, typically by using an inert gas (Figure 2.13(b)). In the next step, the surface is exposed to the second precursor (Figure 2.13(c)). Then, after the formation the next

layer, an inert gas is again used to remove unreacted species from the surface (Figure 2.13(d)). The reaction cycles are repeated until a film of the desired thickness has been obtained (Figure 2.13(e)).

In this study, Sr and Ti precursors are used to grow $SrTiO_3$ [58]. The maximum reactor temperature during the deposition was limited to 250°C due to the thermal decomposition of the precursors at higher temperatures. As a result, post-deposition annealing was carried out to achieve thin crystalline films.

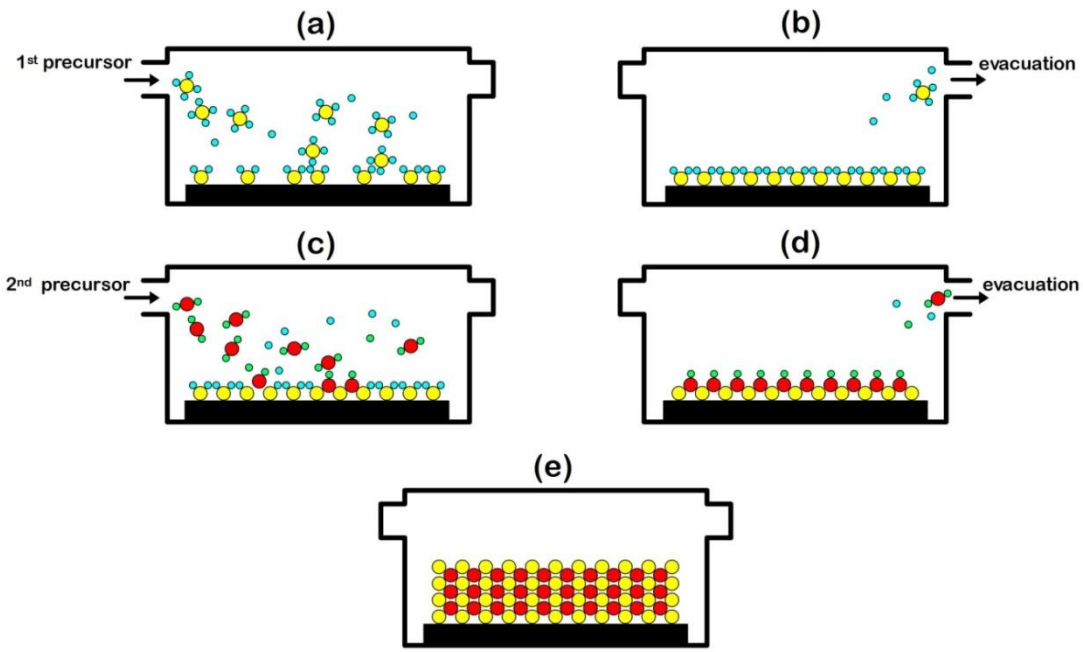

Figure 2.13: Schematic illustration of the deposition cycle in ALD growth: (a) exposure to the first precursor, (b) purge of residual precursors from the reaction chamber, (c) exposure to the second precursor, and (d) evacuation of the reaction chamber; (e) deposited thin films with the desired thickness.

2.6.2 Pulsed laser deposition

Pulsed laser deposition (PLD) is a technique for the deposition of thin films [55], where intense laser pulses of short duration are used to evaporate material from the target. Figure 2.14 shows a simple PLD scheme where the laser beam is generated outside the chamber and directed towards the target by passing it through the focussing lens. The laser beam illuminates the target, which rotates to ensure the uniform coverage of the target surface. The high energy of photons which are generated by laser pulses breaks the chemical bonds of the target and releases particles into the vacuum chamber. Eventually, the ablated particles are deposited on the substrate, forming a thin film. PLD can be used for a wide variety of coating materials. However, problems of a small deposition area and a lack of uniformity of deposited films over the substrate makes the technique unsuitable for industrial applications.

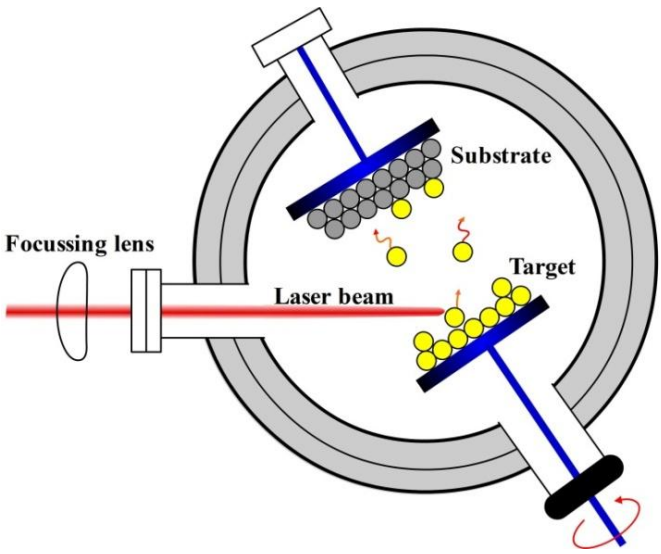

Figure 2.14: Scheme of pulse laser deposition.

2.7 Characterisation

2.7.1 X-ray diffraction

X-ray diffraction (XRD) is a technique used to determine the crystal structure of a sample. Figure 2.15(a) shows the principle of the XRD technique where a beam of x-ray with wavelength λ is radiated onto the sample surface at an angle of θ. When the photons reach the crystal planes, elastic scattering occurs between the photons and atoms. Then, the detector records the scattered intensity of an x-ray beam from the sample. Constructive interference occurs at a particular value of θ, which can be determined by Bragg's law:

$$n\lambda = 2d\ \sin\theta \tag{2.5}$$

where n is an integer and d is the distance between the crystal planes. Therefore, the crystal structure can be determined by interpreting the XRD peaks at different values of θ. In this thesis, XRD technique is used to confirm the crystal structure of $SrTiO_3$. Figure 2.15(b) shows an example of XRD results of $SrTiO_3$ which will be explained in the appropriate chapter.

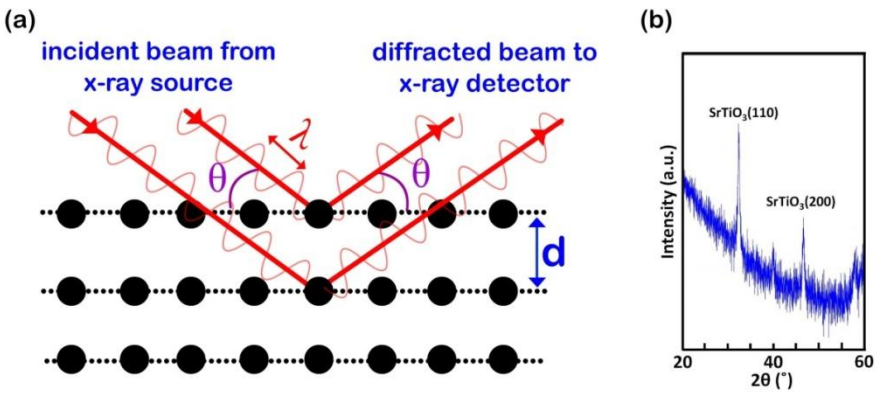

Figure 2.15: The interference of the photons from the crystal planes.

2.7.2 X-ray photoelectron spectroscopy

X-ray photoelectron spectroscopy (XPS) is a quantitative spectroscopic technique used to investigate elemental composition at the surface of a sample. Figure 2.16 shows the basic mechanism of XPS where a beam of x-rays irradiates at a particular wavelength. The photons excite the electronic states of atoms from 1 to 10 nm below the surface of the sample. The electrons ejected pass through the electrostatic fields within a hemispherical analyser which only allows electrons of a given energy to arrive at the detector. Finally, the intensity of a specified energy is recorded by a detector, and the electron binding energy of the emitted electrons can be calculated by:

$$E_{\text{binding}} = E_{\text{photon}} - (E_{\text{kinetic}} + \varphi) \tag{2.4}$$

where $E_{binding}$ is the binding energy of electron, E_{photon} is the energy of x-ray photons, $E_{kinetic}$ is the energy of emitted electrons as measured by the detector and φ is the work function of the spectrometer.

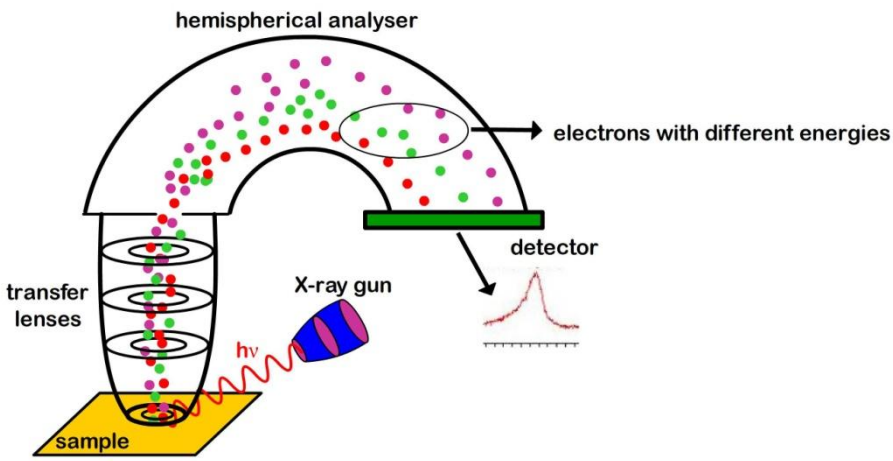

Figure 2.16: Illustration of an XPS instrument.

2.7.3 *J-V* characterisation

The electrical measurements were performed using an Agilent 4155C semiconductor parameter analyzer in combination with a cascade probe station. The most significant measurements in this thesis are *J–V* characterisations, which were performed by sweeping the voltage on the top electrodes while the bottom electrode was grounded (Figure 2.17). The samples were designed in such a way as to have access to both the top and bottom electrodes. In order to check the endurance of resistive switching devices, it was necessary to apply the voltage sweep several times. Due to the lack of multiple sweeping options in the Agilent 4155C, a Labview program was developed to sweep the voltage for the desired number of times.

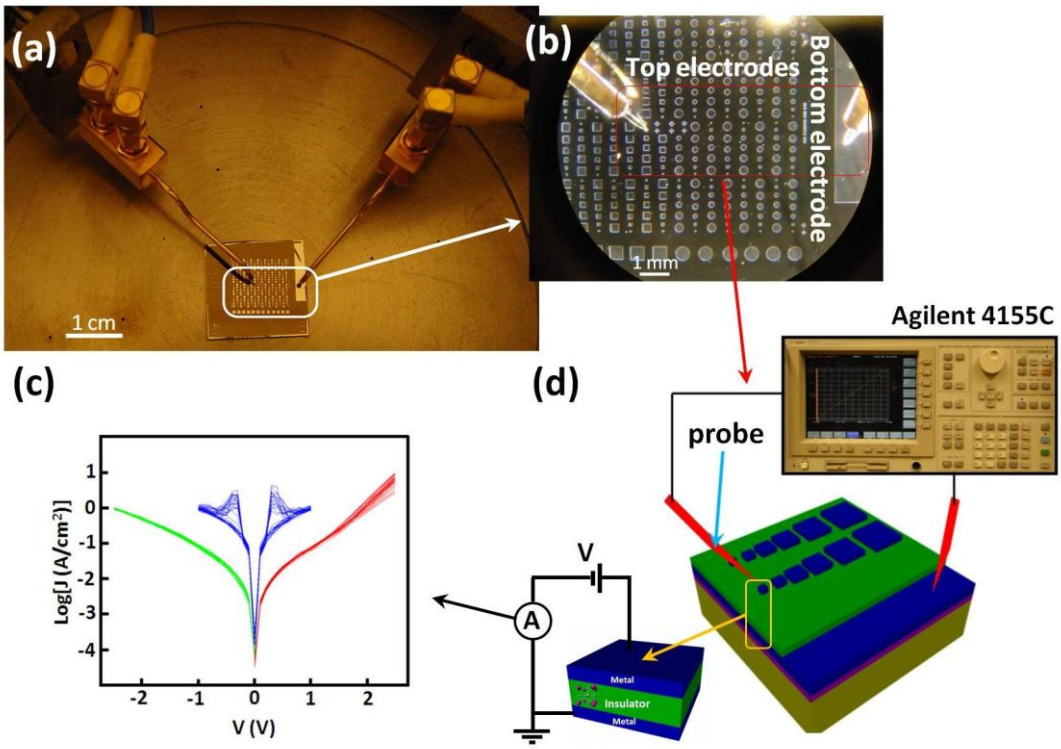

Figure 2.17: (a) Picture of probe station; (b) top and bottom electrodes; (c) *J-V* characteristics of MIM structure; (d) sweeping the voltage on top electrode.

2.7.4 Conductive atomic force microscopy

In this study conductive atomic force microscopy (C-AFM) was performed using the Park Systems XE-150 in order to obtain a microscopic view of the leakage of current through the sample. The C-AFM consists of a cantilever with a conductive tip, and in this study the CDT-NCHR tip was employed. The topographical image is obtained by scanning the surface of the sample where small forces between the tip and the surface lead to deflection of the cantilever. This deflection is detected in terms of the deflection of the laser beam from the top of the cantilever to the photodetector (Figure 2.18). Simultaneously, a constant voltage is applied between the tip and the bottom electrode and the current flowing through the insulator is detected using an external amplifier. Therefore, the current image is obtained as a well as the topography image, which can help in better understanding the microscopic behaviour of the leakage of current through the insulator.

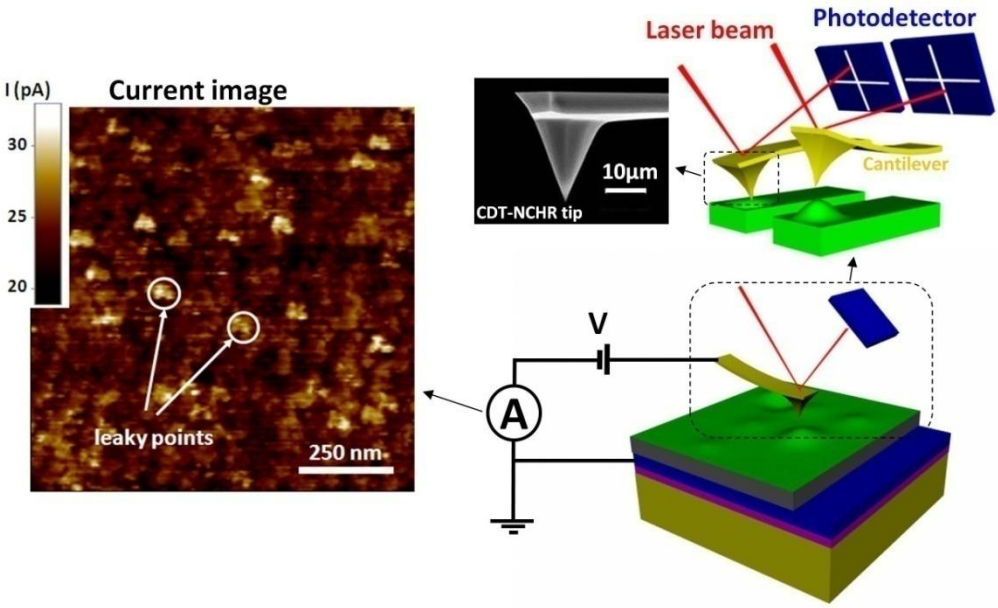

Figure 2.18: Illustration of the C-AFM apparatus.

2.8 Conclusions

RRAM has the advantage of high speed of DRAM, the non-volatile property of Flash memory, and the potential for high density integration, all of which make it one of the most promising candidates for future memory devices. RRAM is based on the resistive switching phenomenon which has been observed in a wide range of transition metal and perovskite oxides. Resistive switching can be divided into bipolar and unipolar behaviour. In the former resistive switching depends on the polarity of the voltage applied, while in the later it depends only on the amplitude of the applied voltage.

A wide variety of models have been proposed to explain resistive switching. This chapter has covered three main types of resistive switching mechanisms, namely electro-chemical, valence-change and thermo-chemical mechanisms. In the electro-chemical mechanism, resistive switching occurs due to the deposition and dissolution of metal cations in the insulator. In the valence-change mechanism, switching the active interface between Ohmic and Schottky contact produces resistive switching characteristic. Finally, the thermo-chemical mechanism is caused by the rupture and rejuvenation of conductive filaments.

Chapter 3

Conduction Mechanisms

'If you can't explain it simply, you don't understand it well enough.'

Albert Einstein

3.1 Introduction

The principle of conduction mechanism was first introduced by Ohm in 1827, who stated that the current through a conductor is proportional to the potential difference across it:

$$I = \frac{1}{R}V \tag{3.1}$$

where R is the resistance of the conductor. Ohm's equation can be applied to a wide range of materials where I–V characteristics show linear behaviour. With the development of quantum mechanics, further conduction mechanisms were introduced to describe the nonlinear I–V characteristics of semiconducting and insulating materials. Most conduction mechanisms originate from two fundamental theories of thermionic emission and quantum tunnelling. Based upon these two

theories, the conduction mechanisms in MIM structures might be categorised into two main groups: interface-controlled mechanisms like the Schottky and Fowler-Nordheim processes, and bulk-controlled mechanisms such as Poole-Frenkel and trap-assisted-tunnelling (Table 3.1).

In the case of interface mechanisms, the bulk is assumed to be highly conductive relative to the interface and the leakage current is only limited by the interface. For bulk mechanisms, the interface does not limit the injection of carriers into the bulk and in this case only the bulk controls leakage current. The Schottky and Poole-Frenkel mechanisms are based on the theory of thermionic emission while Fowler-Nordheim and trap-assisted-tunnelling equations are based on quantum mechanical tunnelling.

This chapter describes the conduction mechanisms summarised in Table 3.1. It begins by presenting the two fundamental theories of thermionic emission and quantum tunnelling, which are necessary to understand the conduction equations. The four main mechanisms (Table 3.1) are then explained in detail. Finally, conventional methods of modelling the *I–V* characteristics are presented.

Table 3.1: The main conduction mechanisms of MIM structures.

	Interface	**Bulk**
Thermionic emission	Schottky	Poole-Frenkel
Tunnelling	Fowler-Nordheim	Trap-assisted-tunnelling

3.2 Thermionic emission theory

Thermionic emission refers to the phenomena in which electrons can escape from the bulk of materials into a vacuum by surmounting the potential energy barrier of V_0 by gaining the energy due to heating. Thermionic emission was first modelled by Richardson, who realised that the current from the hot cathode depends exponentially on temperature [59]. The current density is given by:

$$J = AT^2 \exp\left(-\frac{V_0}{kT}\right) \tag{3.2}$$

where A is the Richardson's constant, k is the Boltzmann's constant, and T is the absolute temperature. For metals, the Fermi level and conduction band are laid on each. The minimum energy required for electrons to escape from the Fermi level to the vacuum is:

$$V_0 = e\varphi_{\mathrm{m}} \tag{3.3}$$

where e is the electron charge and φ_{m} is the work function of metal. The exponential term in Equation 3.2 is also known as the Boltzmann factor, which states the relative probability of an event to occur which requires energy ΔE in a system at temperature T. As a result, the principle of thermionic emission can be extended to any system in which electrical conduction is caused by the thermal emission of electrons over the potential barrier of V_0 by gaining the energy ΔE.

3.3 Quantum tunnelling theory

Quantum tunnelling is described as the ability of an electron to penetrate through a potential barrier. A simple equation for quantum tunnelling can be derived by assuming a rectangular potential barrier. By solving the electron wave functions in three different regions (Figure 3.1) and then using appropriate boundary conditions, the probability that an electron can penetrate through the potential barrier of V_0 is given by:

$$P \approx \exp\left(-2d\sqrt{\frac{8\pi m(V_0)}{h}}\right) \tag{3.4}$$

where d is the potential barrier width, m is the effective mass of the electron and h is Planck's constant. The exponential decay of the electron wave function through the barrier shows that tunnelling probability is reduced exponentially by increasing the barrier width d.

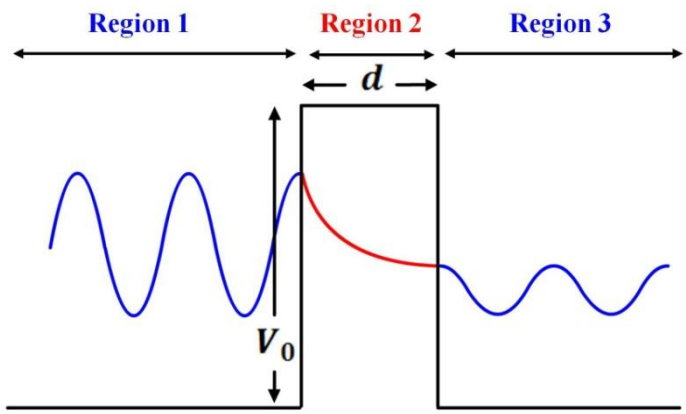

Figure 3.1: Electron penetration through a rectangular potential barrier.

3.4 Interface conduction mechanisms

3.4.1 Schottky emission

When a metal makes contact with a semiconductor, a potential barrier is formed at the metal/semiconductor interface (Figure 3.2). This potential barrier controls the leakage of charge at the interface when it is not limited by the bulk. In this case the bulk is highly conductive due to the high concentration of carriers due to n-type or p-type doping of the semiconductor.

Figure 3.2(a) shows the band structure of a metal and n-type semiconductor. The amount of energy that an electron requires to escape from the bottom of the semiconductor's conduction band into the vacuum is called the electron affinity (χ). When the metal and semiconductor are in contact with each other, the Fermi levels on both sides will line up to establish thermal equilibrium between the metal and the semiconductor. A potential barrier is formed at the interface which is equal to the difference between the work function and the electron affinity:

$$\varphi_{\mathrm{B}} = \varphi_{\mathrm{m}} - \chi \tag{3.5}$$

This potential barrier is termed the Schottky barrier, which controls the leakage of current at the interface (Figure 3.2(b)). The leakage of current occurs due to the emission of electrons from the Fermi level of the metal to the conduction band of the semiconductor at temperature *T*.

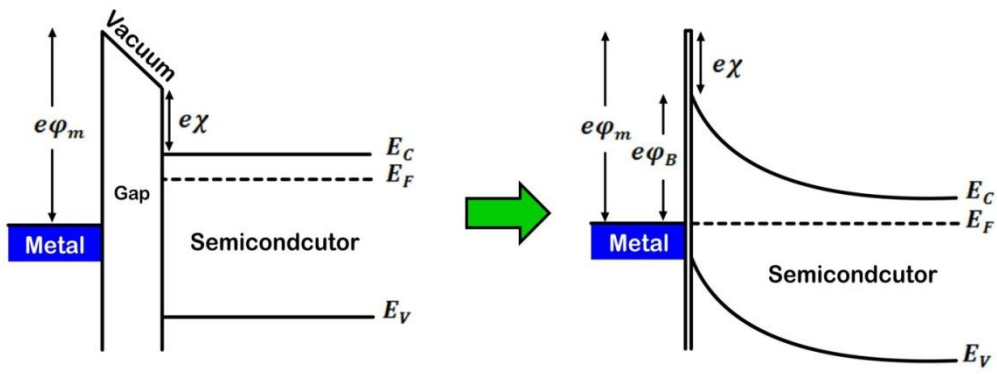

Figure 3.2: Formation of Schottky barrier when a metal is in contact with an insulator.

The conduction mechanism can be modelled using φ_B as the potential barrier in the thermionic emission equation (Equation 3.2). However, the effect of electric field must be also included in Equation 3.1, since this can modify the height of the Schottky barrier, and therefore thermionic emission is dependent on both temperature and the electric field applied.

In order to calculate the effect of the electric field on φ_B, a simple Schottky barrier is illustrated in Figure 3.3. When an electron is at distance x from the metal, an attractive electrostatic image-force will pull the electron back towards the metal due to the positive charges induced on the metal surface which create the normal barrier (Figure 3.3). This image-force can be modelled in terms of the equivalent force that a single positive charge will induce at distance $-x$ from the interface. This positive charge is termed the image-charge, where the attractive force between it and the electron is given by:

$$F = \frac{-e^2}{4\pi\varepsilon_0\varepsilon_r(2x)^2} \tag{3.6}$$

From Equation 3.6, the normal barrier, which is the potential energy of an electron located at distance x from the metal, can be derived by:

$$E(x) = \int_{\infty}^{x} F dx = \frac{-e^2}{16\pi\varepsilon_0\varepsilon_r x} \tag{3.7}$$

When an external electric field is applied, the total potential energy as a function of distance PE(x) will give the effective barrier:

$$PE(x) = -\frac{e^2}{16\pi\varepsilon_0\varepsilon_r x} - e\bar{E}x \tag{3.8}$$

where $\bar{E}$ is the electric field across the junction. Now, the maximum potential barrier is located at x_{m}. By solving the equation $d(PE)/dx = 0$, x_{m} is calculated to be

$$x_{\mathrm{m}} = \sqrt{\frac{e}{16\pi\varepsilon_0\varepsilon_r \bar{E}}} \tag{3.9}$$

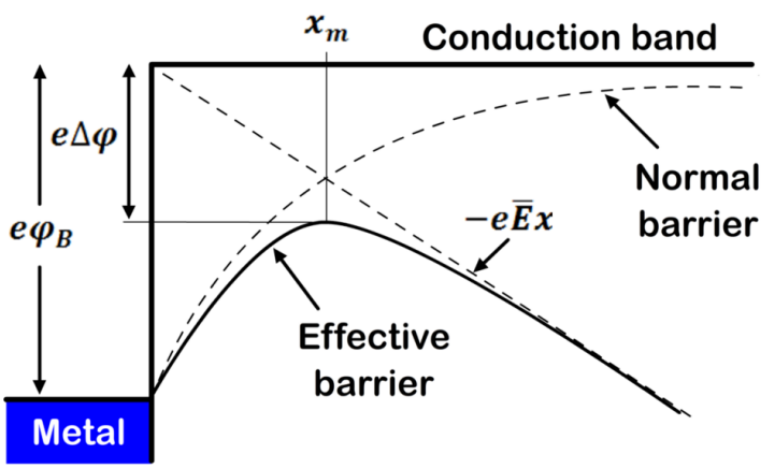

Figure 3.3: Effect of external electric field on the Schottky barrier of a metal and semiconductor interface.

By substituting x_{m} in Equation 3.8 and calculating the potential barrier at x_{m}, the lowering of the Schottky barrier can be derived:

$$\Delta\varphi = \sqrt{\frac{e\bar{E}}{4\pi\varepsilon_0\varepsilon_r}} \tag{3.10}$$

As a result, by including the effect of the electric field on the Schottky barrier ($\Delta\varphi$) in the thermionic emission Equation 3.2, the Schottky equation can be derived:

$$J_{\mathrm{Sch}} = AT^2\exp\left[-e\left(\varphi_{\mathrm{B}} - \sqrt{\frac{e\bar{E}}{4\pi\varepsilon_0\varepsilon_r}}\right)/kT\right] \tag{3.11}$$

where A is a constant.

3.4.2 Fowler-Nordheim tunnelling

A strong electric field can not only reduce the height of the Schottky barrier, but may also change the shape of potential barrier. Figure 3.4(a) illustrates a simple potential step where a uniform external electric field is applied. The potential step barrier will be reshaped to become triangular in a strong electric field (Figure 3.4(b)). Electrons can then tunnel from the metal through the potential barrier directly into the conduction band of the insulator. This mechanism is modelled by the Fowler-Nordheim equation:

$$J_{\mathrm{FN}} = B\bar{E}^2 \exp\left(-\frac{8\pi\sqrt{2me}\varphi^{3/2}}{3h\bar{E}}\right) \tag{3.12}$$

where B is a constant, $\bar{E}$ is the electric field, m is the electron effective mass, φ is the potential barrier equal to the height of the Schottky barrier, and h is Planck's constant.

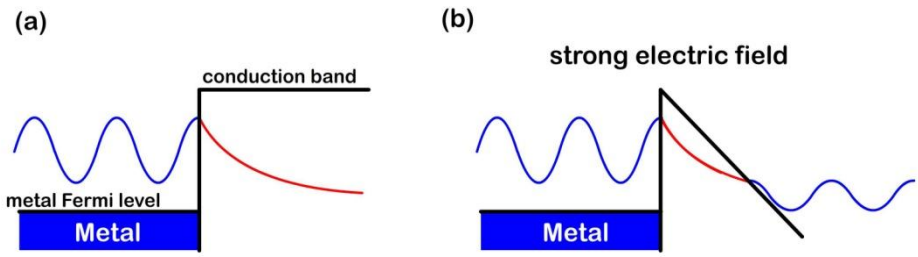

Figure 3.4: (a) Step potential and (b) the effect of strong electric field on the step potential barrier which might result in carriers tunnelling through the barrier.

3.5 Bulk conduction mechanisms

3.5.1 Poole-Frenkel emission

The existence of defects in an insulator can create localised states which serve as traps for electrons. Random thermal fluctuations will then provide enough energy for electrons to escape from trap states to the conduction band. The electrons can subsequently move freely through the conduction band until relaxing into another localised state. The process of the trapping and detrapping of electrons can generate a leakage current through the insulator which is termed the Poole-Frenkel mechanism.

The thermal excitation of electrons from trap states to the conduction band can be explained by the thermionic emission of electrons over the barrier φ_{T} which is the location of the trap level below the conduction band minimum. The application of an external electric field reduces the potential barrier, leading to high rates of trapping and detrapping of electrons through the bulk. As a result, the Poole-Frenkel mechanism can be modelled in terms of the thermionic emission of electrons from trap states into the conduction band by surmounting the potential barrier of φ_{T}, where an external electric field will reduce this potential barrier by $\Delta\varphi$:

$$J = C\bar{E}\exp\left[-e\frac{(\varphi_{\mathrm{T}} - \Delta\varphi)}{kT}\right] \tag{3.13}$$

where C is a constant. The process to find $\Delta\varphi$, the effect of the electric field on φ_{T}, is illustrated in Figure 3.5. When an electron is trapped, the localised state is assumed

to be neutral and, from the movement of an electron over the distance x from the trap state, an attractive electrostatic force will pull the electron back towards the trap state due to the positive charge states of empty traps. This force is equivalent to the force between a positive and negative charge, and is given by:

$$F = \frac{-e^2}{4\pi\varepsilon_0\varepsilon_r x^2} \tag{3.14}$$

Therefore, the potential energy of an electron located at distance x from the trap state can be calculated as:

$$E(x) = \int_{\infty}^{x} F dx = -\frac{e^2}{4\pi\varepsilon_0\varepsilon_r x} \tag{3.15}$$

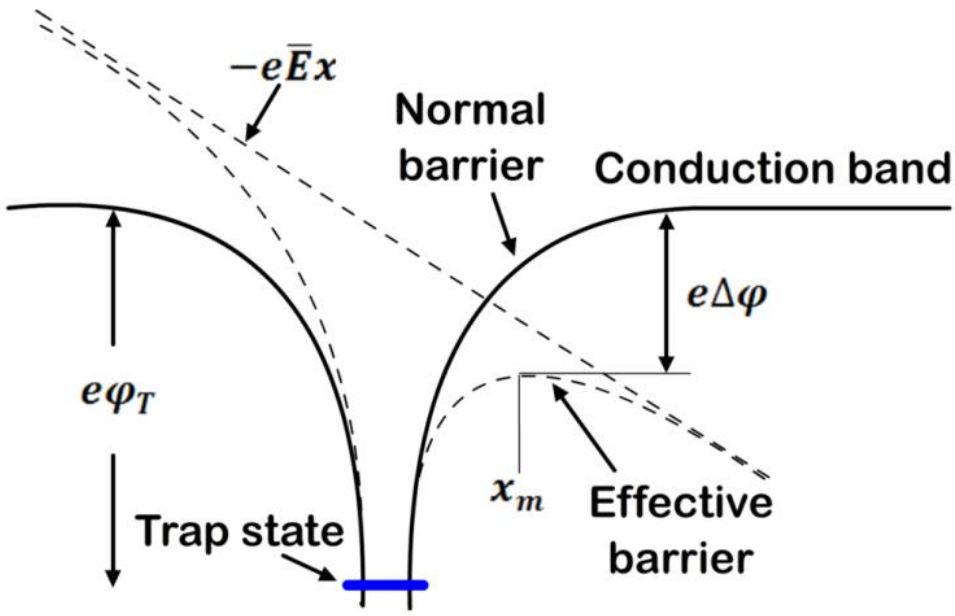

Figure 3.5: The effect of external electric field on the potential barrier between the trap state and the conduction band.

This is illustrated in Figure 3.5 as the normal barrier. The total potential barriers $PE(x)$ in the presence of an electric field $\bar{E}$ is given by:

$$PE(x) = -\frac{e^2}{4\pi\varepsilon_0\varepsilon_r x} - e\bar{E}x \tag{3.16}$$

This is the effective barrier, and in order to calculate the maximum potential barrier it is required to solve the equation $d(PE)/dx = 0$, which gives the value of x_m:

$$x_{\mathrm{m}} = \sqrt{\frac{e}{4\pi\varepsilon_0\varepsilon_r\bar{E}}} \tag{3.17}$$

By substituting the value of x_{m} in Equation. 3.16, the maximum potential barrier is calculated, which shows that the barrier is lowered by:

$$\Delta\varphi = \sqrt{\frac{e\bar{E}}{\pi\varepsilon_0\varepsilon_r}} \tag{3.18}$$

By including the effect of the electric field on the potential barrier of φ_T in Equation 3.13, the Poole-Frenkel equation is derived as:

$$J_{\mathrm{PF}} = \mathrm{C}\bar{E}\exp\left[-e\left(\varphi_{\mathrm{T}} - \sqrt{\frac{e\bar{E}}{\pi\varepsilon_0\varepsilon_r}}\right)/kT\right] \tag{3.19}$$

3.5.2 Trap-assisted-tunnelling

As in the case of tunnelling through the Schottky barrier, a strong electric field can modify the potential barrier of traps in the Poole-Frenkel mechanism. Figure 3.6(a) shows trap states below the conduction band. In a weaker electric field the thermionic emission of electrons over the potential barrier results in the Poole-Frenkel mechanism, as explained in the previous section (Figure 3.6(b)). However, increasing the electric field will cause a narrowing of the potential barrier. Now, the electrons can tunnel through the potential barrier to the conduction band (Figure 3.6(c)). In this case, the potential barrier has a similar shape to that of the Schottky barrier in a strong electric field. Therefore, trap-assisted-tunnelling can be written as follows [60]:

$$J_{\mathrm{TAT}} = D\exp\left(-\frac{8\pi\sqrt{2me}\varphi^{3/2}}{3h\bar{E}}\right) \tag{3.20}$$

where D is a constant and m is the effective mass of the electron.

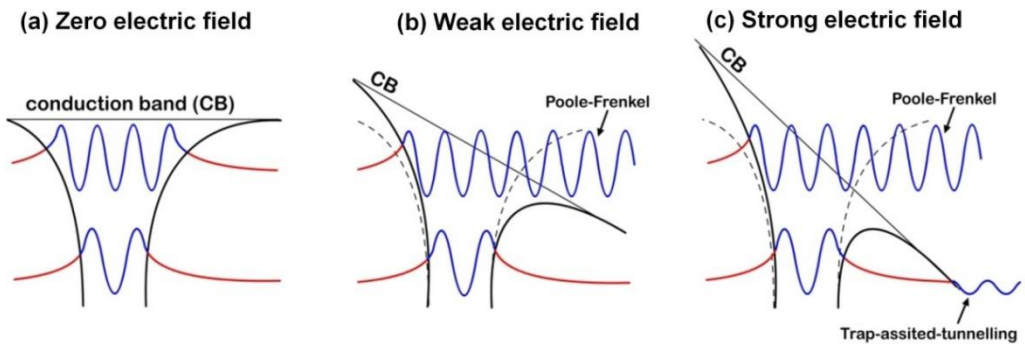

Figure 3.6: (a) Trapped electrons in trap states below the conduction band; (b) electron escaping from the trap state to the conduction band in a weak electric field (Poole-Frenkel); (c) electron tunnelling from trap state to the conduction band in a strong electric field (trap-assisted-tunnelling).

3.6 Leakage current modelling

In conventional techniques used to model the leakage current, the MIM structure is divided into three main regions as depicted in Figure 3.7(a): top interface, bulk and bottom interface. Depending on the *I-V* characteristics involved, either one of the interfaces or the bulk can limit the leakage of current. When one of the interfaces controls the leakage of current, the bulk is assumed to be highly conductive due to the high concentration of defects or doping. The effect of the opposite interface is then assumed to be negligible, possibly due to the lowering of the Schottky barrier height or the existence of an Ohmic contact between the metal and insulator (Figure 3.7(b)). In this case either of the Schottky or Fowler-Nordheim mechanisms is responsible for controlling the leakage current. When the bulk controls the leakage of current, both interfaces are assumed to be highly conductive compared to the bulk (Figure 3.7(c)). Hence, bulk mechanisms are used to model the leakage current.

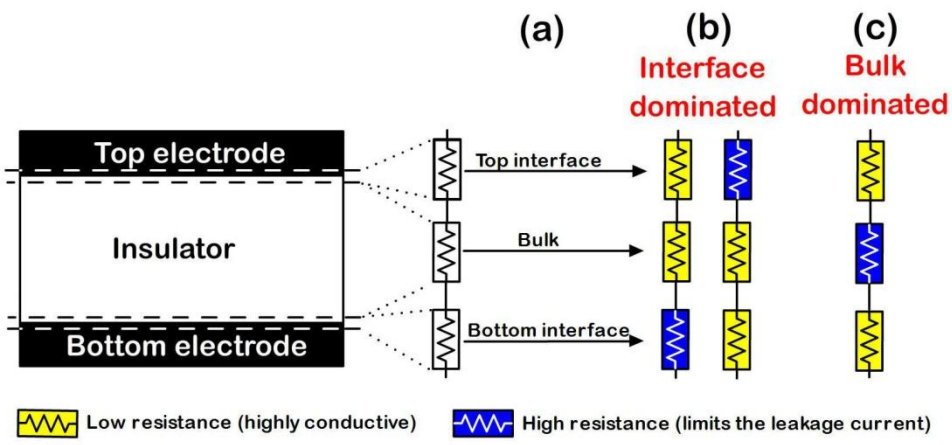

Figure 3.7: (a) Modelling the MIM device by three regions where the leakage current can be attributed to either (b) interface or (c) bulk.

3.6.1 Thermionic emission vs. tunnelling

Before a mechanism can be attributed to the interface or the bulk, the thermionic emission or tunnelling behaviour involved in the leakage current must be specified. The tunnelling current is represented by an abrupt increase in the leakage current at high electric field while in thermionic emission the leakage current increases gradually when the voltage is increased from zero (Figure 3.8(a)).

Thermionic emission and tunnelling can be better distinguished from each other by drawing two plots of $\ln(J)$ vs. $\sqrt{E}$ and $\ln(J)$ vs. $1/E$. In thermionic emission mechanisms, the relationship between current-density and the electric field can be written as:

$$\ln(J) \sim \sqrt{E} \tag{3.21}$$

For tunnelling mechanisms the following equation governs the relationship between the current-density and the electric field:

$$\ln(J) \sim -1/E \tag{3.22}$$

As a result, if the J–E characteristics shows linear behaviour in the $\ln(J) - \sqrt{E}$ plot, then the dominant mechanism is thermionic emission (Figure 3.8(b)). Alternatively, if J–E characteristics shows linearity in the $\ln(J) - 1/E$ plot, the dominant mechanism is tunnelling (Figure 3.8(c)).

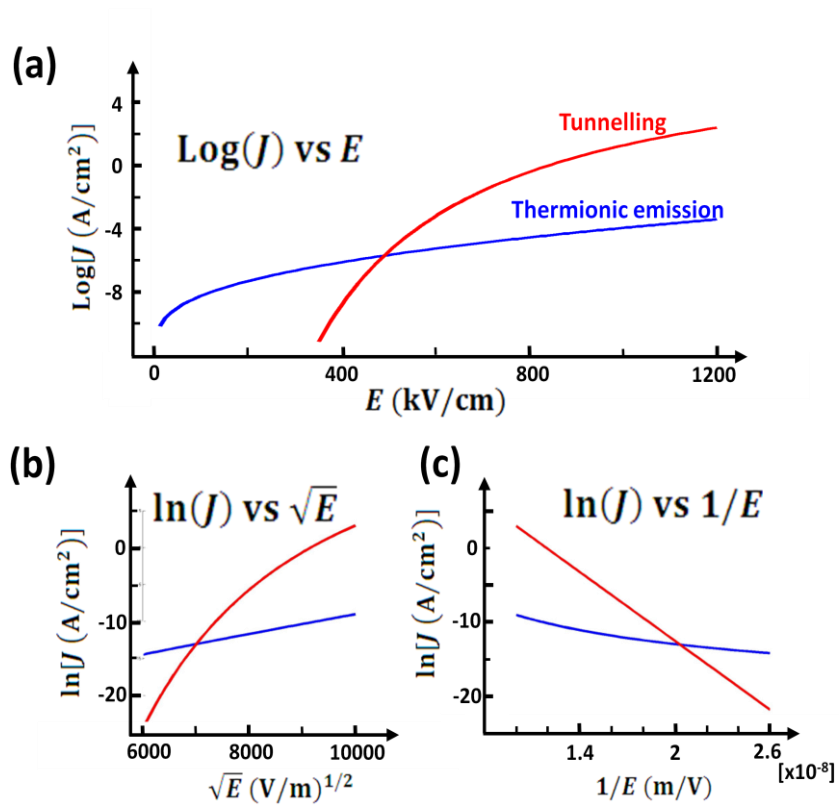

Figure 3.8: (a) *J-E* characteristics of thermionic emission (blue) and tunnelling mechanism (red); (b) ln(*J*) vs √*E* where the thermionic emission curve shows linearity; (c) ln(*J*) vs *1/E* where the tunnelling curve is linear.

When the dominant mechanism is thermionic emission, the height of the potential barrier can be determined by measuring the leakage current at different temperatures (Figure 3.9(a)). By increasing temperature, more electrons gain enough energy to surmount the potential barrier, which results in an increase of the leakage current in constant electric field. This is shown in Figure 3.9(a), where the *J*–*E* characteristics shift to higher values as temperature increases. The height of the potential barrier (φ) can be calculated from the slope of ln(J) vs $1/kT$ (Arrhenius plot) at a fixed electric field as depicted in Figure 3.9(b).

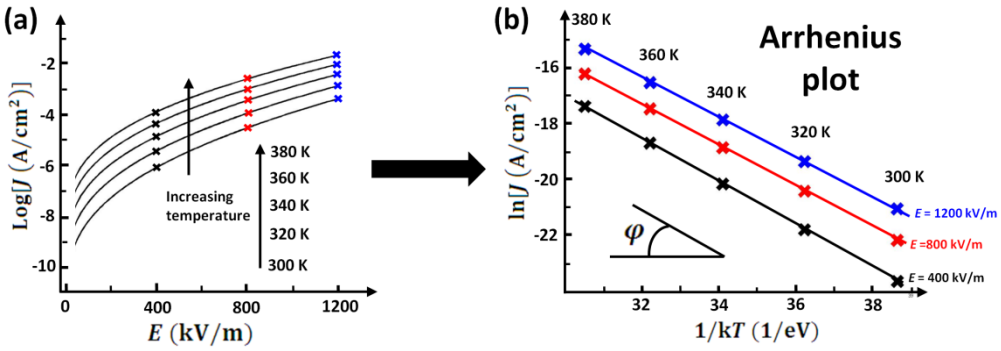

Figure 3.9: (a) Increasing the leakage current by temperature; (b) Arrhenius plot of leakage current in different electric fields.

3.6.2 Schottky vs. Poole-Frenkel

When the leakage exhibits thermionic emission behaviour, it might follow Schottky emission at the metal/insulator interface or Poole-Frenkel due to the presence of bulk traps. In order to determine which mechanism is operating, it is necessary to measure the refractive index of the insulator by e.g. ellipsometry [61, 62]. Then, the optical dielectric constant of the insulator can be calculated as:

$$\varepsilon_{\mathrm{r}} = n^2 \tag{3.23}$$

where n is the refractive index. The optical dielectric constant can also be calculated by fitting the experimental results to either the Schottky (Equation 3.11) or Poole-Frenkel (Equation 3.19). However, the value of ε_{r} obtained from Equation 3.23 only matches one of the values calculated from Equations 3.11 and 3.19. Therefore, thermionic mechanism would be as a result of either Schottky or Poole-Frenkel emission. The difference between the values of ε_{r} calculated from Equations 3.11 and 3.19 arises from the levels of Coulomb potential that the electrons face upon application of electric field [63]. In Poole-Frenkel, the potential barrier reduction is

larger than in Schottky emission by a factor of 2, since the lowering of the barrier is twice as large due to the immobility of the positive charge (Figure 3.10).

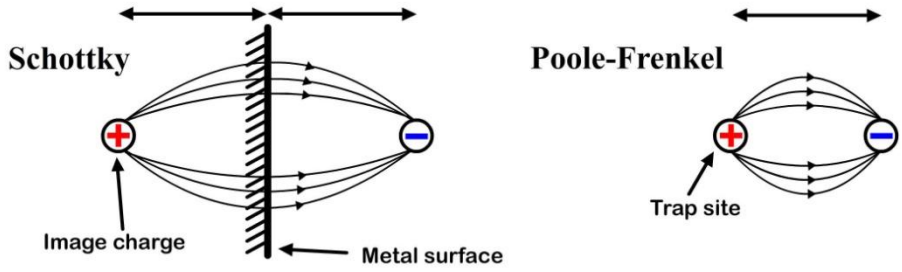

Figure 3.10: The potential that electrons are face in: (a) Schottky; (b) Poole-Frenkel.

3.6.3 Fowler-Nordheim vs. trap-assisted-tunnelling

Tunnelling occurs due to the effect of a strong electric field on the narrowing of the potential barrier which results in electrons tunnelling thorough it. In order to find the appropriate tunnelling mechanism, it is necessary to specify the nature of the potential barrier, which could be either a Schottky potential barrier at the interface (φ_B) or potential well in the bulk (φ_T). The potential barrier can be specified by considering the leakage of current in a weak electric field where the potential barrier shape is less distorted. In this case, the leakage current is dominated by the thermionic emission of energetic electrons over the potential barrier. Hence, as explained in the previous section, thermionic emission can be attributed to either Schottky or Poole-Frenkel mechanisms.

If the height of Schottky barrier controls the leakage current at a weak electric field, the abrupt increase in the leakage current in strong electric field is due to the

narrowing of the width of the Schottky barrier, which can be modelled by Fowler-Nordheim. In contrast, if the Poole-Frenkel mechanisms controls the leakage current through the bulk, trap-assisted-tunnelling would be responsible for high leakage current in strong electric field. By substituting the calculated values of ε_r and potential barrier height in the tunnelling equations, the effective mass of the electron can be calculated by fitting the characteristics of the leakage current.

3.7 Conclusions

Thermionic emission and tunnelling mechanisms have been considered in this chapter. The Schottky and Poole-Frenkel mechanisms are based on the thermionic emission of electrons over the potential barriers while the Fowler-Nordheim and trap-assisted-tunnelling mechanisms are used to model the tunnelling of electrons through the potential barriers at strong electric fields.

In conventional leakage current modelling, the MIM structure is divided into the interface and the bulk, where the leakage current is dominated by either interface or bulk mechanisms. In most metal oxides, thermionic emission mechanisms have been used to describe the temperate dependency of $J-E$ characteristics, while tunnelling mechanisms are used to explain the abrupt increase in the leakage current at high electric fields.

Chapter 4

Leakage Current Behaviour of $SrTiO_3$

'If I have seen further than others, it is by standing upon the shoulders of giants.'

Isaac Newton

4.1 Introduction

Transition metal oxide junctions have attracted considerable attention due to their potential for applications such as DRAM [64], and RRAM [65-68]. For such applications, an important factor to be addressed is the leakage current that affects the reliability of the devices. Leakage current through transition metal oxides has been the subject of extensive discussion, and different models have been proposed to explain it [69-73]. Thermionic field emission equations (i.e. Schottky or Poole-Frenkel) are frequently used to explain temperature dependent characteristics of leakage current, which is mainly attributed to oxygen vacancies [66, 70, 73-75]. The conduction mechanism of the oxygen vacancies was also found to vary according to the difference in the thermionic field emission types (either Schottky or Poole-Frenkel).

In the case of Poole-Frenkel emission (Equation 4.1), the oxygen vacancies are regarded as traps inside the bulk [70, 73]. Leakage current originates from the thermionic field emission of electrons between oxygen vacancies (Figure 4.1(a)) and can be expressed by Poole-Frenkel equation

$$J_{\mathrm{PF}} = C\bar{E}\exp\left[-e\left(\varphi_{\mathrm{BPF}} - \sqrt{\frac{e\bar{E}}{\pi\varepsilon_0\varepsilon_{\mathrm{r}}}}\right)/kT\right] \tag{4.1}$$

where $\bar{E}$ is the electric field strength, C is a constant, e is the electron charge, k is Boltzmann's constant, T is the temperature, φ_{BPF} is the location of the trap level below the conduction band minimum, ε_0 is the vacuum permittivity and ε_r is the dielectric constant.

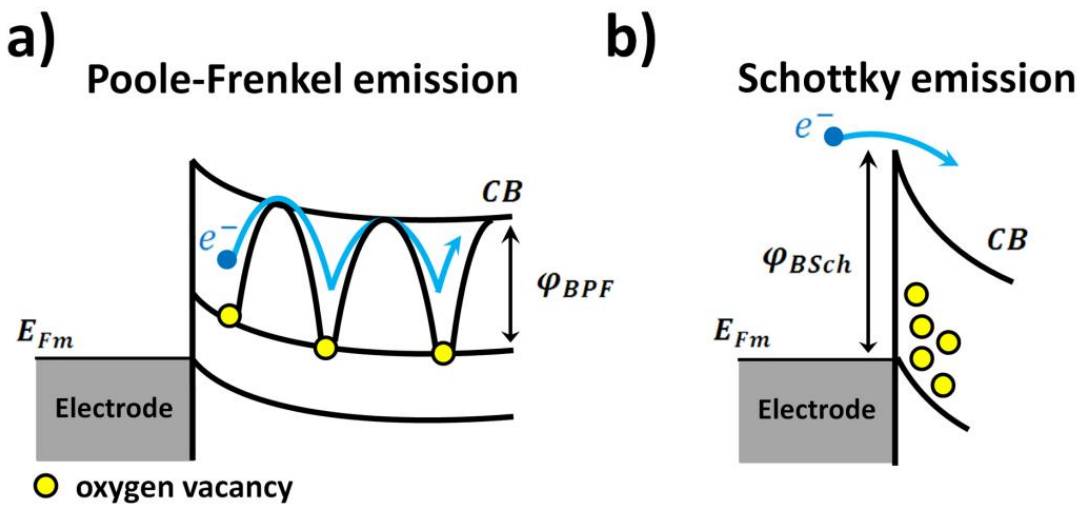

Figure 4.1: Scheme of thermionic field emission of electrons (a) between the oxygen vacancies in bulk that can be modelled by Poole-Frenkel emission equation, and (b) over the effective Schottky barrier that can be modelled by the Schottky emission equation.

For Schottky emission (Figure 4.1(b)), the bulk is regarded as an n-type or p-type semiconductor depending on the defect chemistry [66, 74-76]. The leakage current is then due to thermionic field emission of electrons over the effective Schottky barrier (φ_{BSch}) and the leakage current can be modelled by the Schottky equation (Equation 3.11). An electric field can drive diffusion of charged defects such as oxygen vacancies, changing their concentration profiles at the interface, resulting in a field dependent variation of φ_{BSch}, and, subsequently, an asymmetry in the leakage current.

Both equations can explain the existence of temperature-dependent leakage characteristics, but the underlying conduction processes are related to the dielectric in fundamentally different ways: Poole-Frenkel is limited by conduction mechanisms in the bulk region without any limit on the carrier injection, whereas Schottky emission is limited by injection at the interface, with bulk conduction being relatively high, mediated by defects such as oxygen vacancies. In order to reduce the leakage current, it is important to determine which of these mechanisms dominates. For instance, if it is Schottky emission, the interface controls the leakage current so that using different electrode materials might improve the leakage current [77, 78]. In contrast, if Poole-Frenkel is the dominant mechanism, then dielectric quality controls the leakage current, and bulk treatments such as oxygen annealing might be deployed to reduce the leakage current [79].

However, there are several discrepancies with the existing models in respect of the impact of dielectric film quality or interface on leakage current. The

Poole-Frenkel model proposed previously [70, 71, 73, 80-82] suggests that bulk controls the leakage current while the Schottky emission model [39, 83-87] indicates interface as a dominant factor.

Moreover, restriction to just the interface mechanism or just the bulk mechanism can lead to inaccurate modelling of leakage current, for example in the calculation of the dielectric constant from the thermionic field emission equations obtained from the leakage current in the positive voltage region [73, 79, 85, 88]. From Poole-Frenkel and Schottky equations, the dielectric constant is defined by the slope of the leakage current curves on a logarithmic scale. Under normal circumstances ε_r is greater than unity [89], but dielectric constants obtained from the slope can be smaller than unity [90].

In this chapter, the results of a study into leakage current mechanisms in $SrTiO_3$ MIM structures are presented. A model including both interface and bulk effects upon the leakage current is proposed. The model demonstrates an improved agreement with experimental current density, both as a function of voltage and temperature compared to previous published models [79, 80, 83, 85, 87]. The model also indicates the existence of fixed positive charges at the bottom electrode leading to the characteristic asymmetry observed in the J–V characteristics.

4.2 Experiment

A 100 nm thick Pt film was deposited on a $Ti/SiO_2/Si$ substrate to act as the bottom electrode in the MIM structure. The 10 nm Ti flash-layer provides adhesion between the Pt and the SiO_2 layer. On top of the Pt electrode was deposited a 50 nm layer of $SrTiO_3$ via ALD at a reactor temperature of 250 °C. After deposition, the sample was annealed at 500 and 600 °C for 120 s in N_2. After each annealing, the crystal structure of the film was characterised by x-ray diffraction (Figure 4.2), which showed strong $SrTiO_3$ (110) peaks after annealing at 600 °C, consistent with the expected perovskite structure. Following the anneal, circular Pt electrodes with a thickness of 100 nm and diameter of 150 μm were deposited to form MIM structures used in electrical characterisation. The leakage current characteristics were measured across a temperature range of 300–380 K.

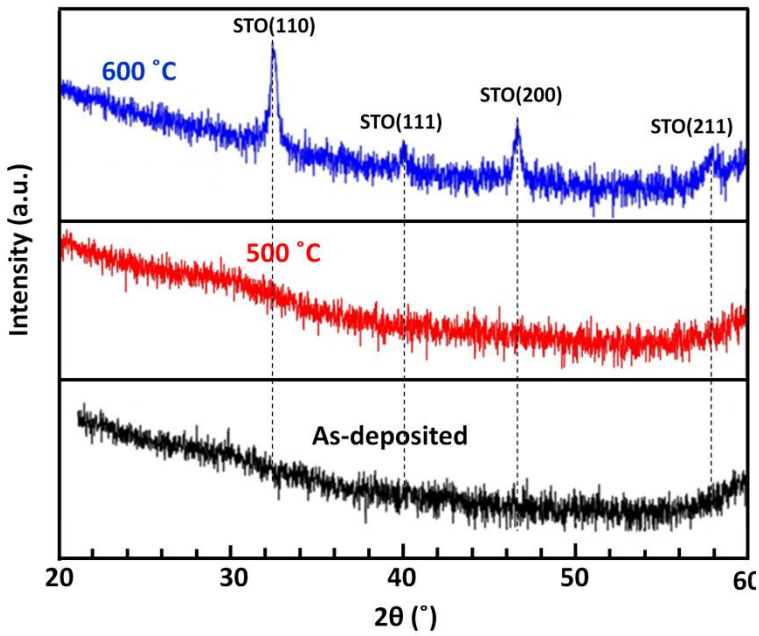

Figure 4.2: The XRD results of $SrTiO_3$ before and after 600 °C annealing.

4.3 Electrical results

Figure 4.3 shows the *J*-*V* characteristics of a $SrTiO_3$ MIM structure. For positive voltages, there are two distinct regions of behaviour: low voltage ($V < +0.5$ V) where the leakage current is less than 10^{-8} A/cm^2 and high voltage ($V > +1.3$ V) where the leakage current increases with increasing temperature. Each *J*–*V* characteristic exhibits an abrupt transition between the two regions at a voltage which decreases with temperature ($+0.5 < V < +1.3$ V). At high negative voltage bias ($V < -1$ V), the measured current shows a temperature dependence similar to that observed for positive biases. However, the leakage current for negative voltages is lower than the corresponding positive voltages, leading to an asymmetry in leakage current curves.

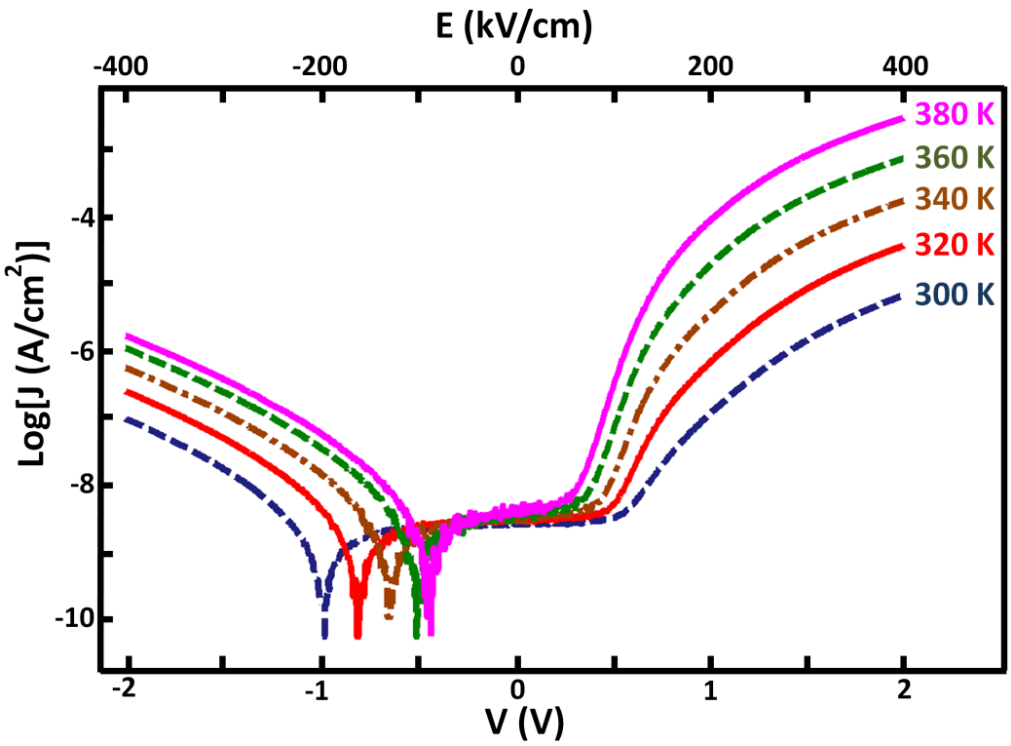

Figure 4.3: *J*–*E* characteristics of Pt/$SrTiO_3$/Pt structure for both negative and positive voltage biases over temperature range 300 K to 380 K.

4.4 Modelling the leakage current

The temperature dependence of the leakage current at $V > +0.5$ V is suggestive of a thermionic field emission, indicating a current dominated by either Poole-Frenkel emission, Equation 4.1, or Schottky emission Equation 3.11. The temperature independence of low leakage current for ($V < +0.5$ V) may imply a current blocked at the metal/insulator interface and there is only small leakage current due to the Ohmic behaviour.

Based upon these observations, a likely model might be that the current is dominated by a bulk conduction mechanism where at low voltage, the interface blocks injection of electrons to the bulk. Indeed, at high voltage the leakage current is modelled very accurately by Equation 4.1, where the electrons move through the bulk by hopping between localised states such as might arise from oxygen vacancies inside the insulator (Figure 4.1(a)).

At low voltage ($V < +0.5$ V) the leakage current is dominated by the interface where the injection of electrons into the bulk is blocked. In the range $+0.5 < V < +1.3$ V, injection most likely occurs by tunnelling of electrons from the electrode to the defect states near the interface, which may be modelled by the trap-assisted-tunnelling current [91]

$$J_{\mathrm{TAT}} = A \exp\left(-\frac{8\pi\sqrt{2em}\varphi_{\mathrm{BTAT}}^{\frac{3}{2}}}{3h\bar{E}}\right) \tag{4.2}$$

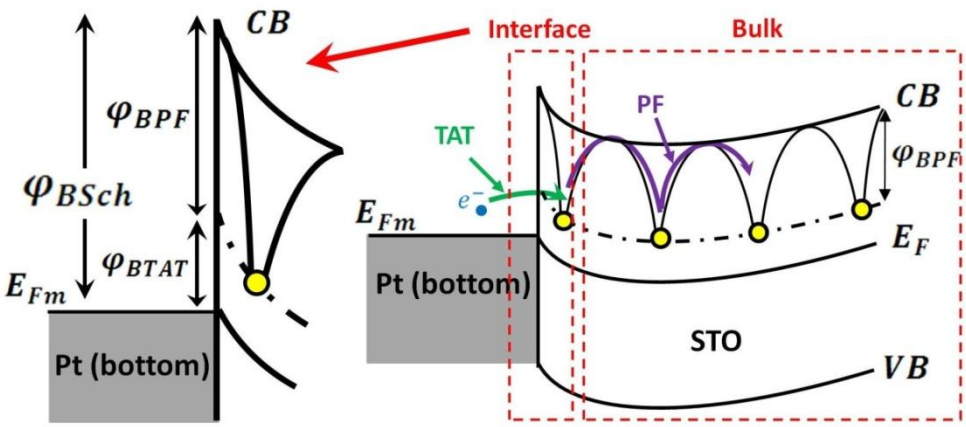

Figure 4.4: Schematic of leakage current mechanisms through $SrTiO_3$.

where A is a prefactor. In this model φ_{BTAT} is the difference of φ_{BSch} and φ_{BPF}, as the electrons tunnel from the electrode to the defect states near the interface (Figure 4.4).

Based on this model, electrons are injected into deep states near the interface by tunnelling and subsequently move through the bulk by thermal emission between traps throughout the dielectric film. At low voltage, the electric field is not high enough for injection and the Poole-Frenkel mechanism is suppressed by the interface where the Ohmic behaviour leads to the small leakage current at $V < +0.5$ V. By increasing the voltage, the potential across the dielectric is sufficient to result in injection of electrons to the states near the interface, causing an abrupt increase in the leakage current, as shown in Figure 4.3. At this point, the thermionic field emission of electrons between the oxygen vacancies limits the leakage current and the dominant mechanism is Poole-Frenkel.

In order to determine values for the physical parameters in the Poole-Frenkel and trap-assisted-tunnelling equations, the experimental data is plotted in two ways. Figure 4.5 illustrates ln(J / E) against $E^{1/2}$ at a positive bias over temperature range 300 K to 380 K. The plots show a linear relation for voltage biases above +1.3 V, indicating Poole-Frenkel as the dominant mechanism for V > +1.3 V. The dielectric constant (ε_r) has been calculated 5.7 from the slope of lines in Figure 4.5 which is consistent with Equation 3.23 using the refractive index of 1.95 measured by an ellipsometer [83]. Also, the trap ionisation energy (φ_{BPF}) can be calculated from the slope of ln(J / E) vs 1/T at a fixed voltage. Below +1.3 V, the leakage current cannot be explained by the Poole-Frenkel mechanism since the plots show a nonlinear behaviour.

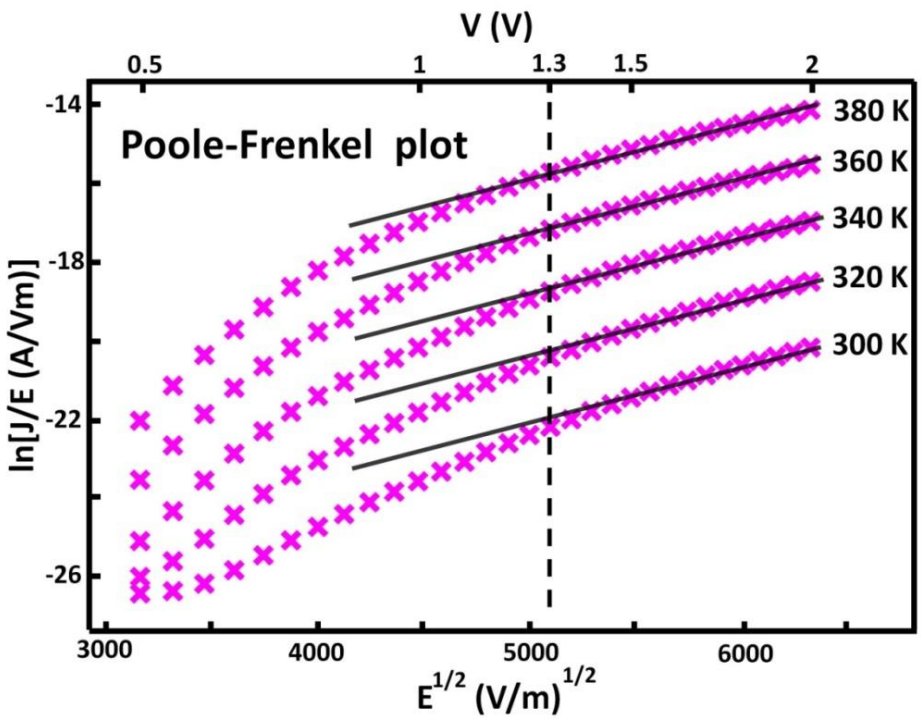

Figure 4.5: Extracting the parameters of Poole-Frenkel equations in the temperature range of 300–380 K from ln(J) vs 1/E (Poole-Frenkel plot).

In the case of trap-assisted-tunnelling, plotting ln(J) against 1/E also yields a straight-line fit, but over the complementary range of V < +1.3 V, as shown in Figure 4.6. This might indicate that over the range $+0.5 < V < +1.3$ V trap-assisted-tunnelling limits the leakage current while by increasing the voltage (V > +1.3 V) Poole-Frenkel is the dominate mechanism. However, the latter plot shows an increase in current density with increasing temperature, inconsistent with Equation 4.2, where trap-assisted-tunnelling is temperature independent. Clearly, this experimentally observed temperature dependence shows that at low field the mechanism cannot be purely due to tunnelling of carriers through an interface barrier and thermionic emission might be involved in the conduction mechanism.

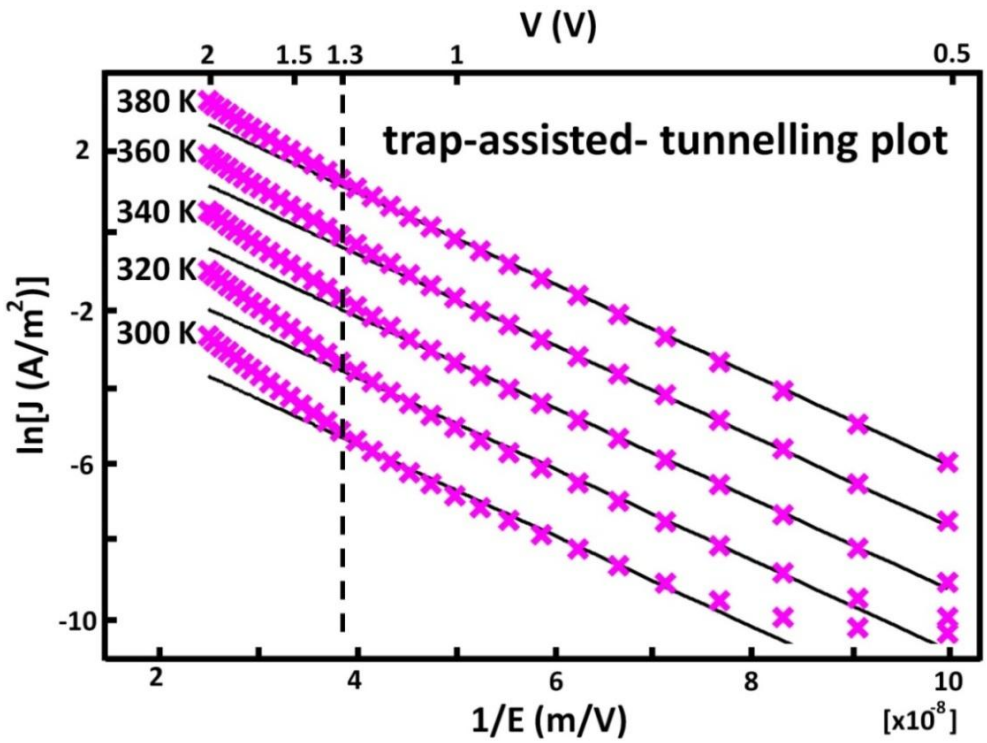

Figure 4.6: Extracting the parameters of trap-assisted-tunnelling equations in the temperature range of 300–380 K from ln(J) vs 1/E (trap-assisted-tunnelling plot).

The temperature dependence can be introduced in Equation 4.2 by modifying the prefactor *A*, which defines the magnitude of tunnelling current at high electric field. As the first step, the experimental characteristics were fitted to Equation 4.2 for the data obtained at 380 K. From the gradient (Figure 4.6), φ_{BTAT} is calculated to be 0.18 eV, using $m = 0.05m_{\mathrm{e}}$ with m_{e} being the free electron rest-mass [83].

The new prefactor, *A*, was then obtained for the remaining temperatures using this value of φ_{BTAT}. The resulting temperature dependence of *A* is plotted in Figure 4.7, which has an Arrhenius form. The pre-factor, *A*(*T*), can therefore be expressed as

$$A = A_0 \exp\left(-\frac{e}{kT}\varphi_{\mathrm{B}}\right) \tag{4.3}$$

where A_0 is a constant and from the gradient of the line, the activation energy, φ_{B}, is calculated to be 0.82 eV. Combining Equations 4.2 and 4.3 provides the current-density for $V < +1.3$ V

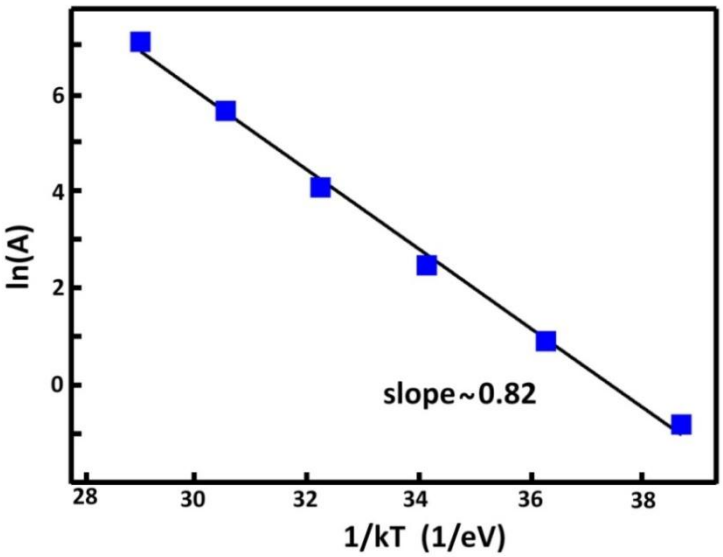

Figure 4.7: The calculated values of *A* as a function of 1/*kT*.

$$J = A_0 \exp\left(-\frac{e}{kT}\varphi_{\mathrm{B}}\right) \exp\left(-\frac{8\pi\sqrt{2em_{\mathrm{s}}}\varphi_{\mathrm{BTAT}}^{3/2}}{3hE}\right) \tag{4.4}$$

Equation 4.4 fits the observations very well. Noting the similarity between the form of the pre-factor and the Poole-Frenkel emission formula, suggests the leakage current can be represented by the product of the two mechanisms, Poole-Frenkel and trap-assisted-tunnelling:

$$J \sim P_{\mathrm{PF}} \times P_{\mathrm{TAT}} \tag{4.5}$$

where P_{PF} is the probability that an electron will pass through the bulk by thermal excitation via trap bound-states and the conduction band of the insulator and P_{TAT} is electron injection probability at the interface. To understand the physical meaning of Equation 4.5 further, the parameters of the Poole-Frenkel equation need to be explored in more detail, taking into account the proximity of the electron traps to the interface. Equation 4.1 includes of a constant, C, and an exponential term. When deep electron traps lie near the interface, the injection of electrons tunnelling through the interface barrier into the nearest trap is highly probable and nearly independent of V. Therefore, the leakage current will be limited by the hopping conduction between the deep states. These deep traps might arise from oxygen vacancies [48, 76, 88, 92-95]. In this case, C in Equation 4.1 represents the current density at low voltage, arising from the hopping of electrons that have enough energy to overcome the potential barriers between the defects. By increasing the bias, and hence lowering the effective barrier height for hopping, more electrons can contribute to the leakage

current, which thus increases. This bias effect corresponds with the exponential term in Equation 4.1. However, the picture becomes modified when the defects in the $SrTiO_3$ are located further from the interface. Where this is the case, a significantly higher voltage is required to inject the electrons into the vacancies by tunnelling, as the barrier width is effectively much bigger. The injection rate will then begin to become significant at a higher V compared to where the traps are in close proximity to the interface, ($+0.5 < V < +1.3$ V). This can be observed in the experimental characteristics (Figure 4.3) where there is an abrupt transition between low and high leakage current. This would correspond to a voltage dependence of C in Equation 4.1. The effect is illustrated in Figure 4.8. This shows the calculated injection current from tunnelling as a function of applied voltage V using Equation 4.2, with φ_{BTAT} taken to be the value of 0.18 eV extracted from the fit to data in Figure 4.6.

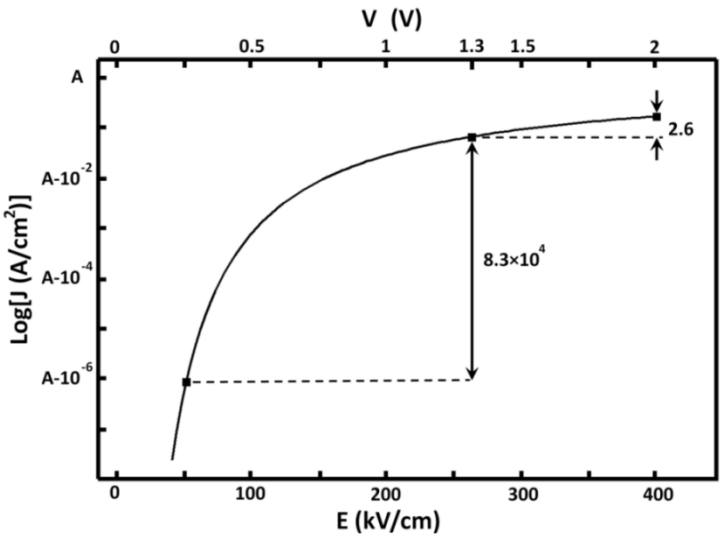

Figure 4.8: The relationship between the electric field and tunnelling current which shows how the injection of electrons to the vacancies is changed by electric field.

By increasing the voltage from +0.25 to +1.3 V, the tunnelling current increases by more than four orders of magnitude. Above +1.3 V, the current increases much less dramatically, and by less than an order of magnitude up to +2 V. As a result, in Equation 4.4, the trap-assisted-tunnelling term defines the variation of C with voltage and the Poole-Frenkel term explains the temperature dependence of the thermionic field emission of electrons. Equation 4.4 remains valid for $V > +1.3$ V where the trap-assisted-tunnelling is saturated. Combining the Poole-Frenkel and trap-assisted-tunnelling equations, a more general expression for the leakage current-density is obtained as follows

$$J = BE\exp\left(-\frac{8\pi\sqrt{2em_s}\varphi_{\mathrm{BTAT}}^{3/2}}{3hE}\right)\exp\left[-e\left(\varphi_{\mathrm{BPF}} - \sqrt{\frac{eE}{\pi\varepsilon_0\varepsilon_r}}\right)/kT\right] \quad (4.6)$$

where B is a constant. In terms of the global agreement with the J–V characteristics, Equation 4.6 is a substantial improvement over models proposed previously [79, 80, 83, 85, 87]. Figure 4.9 shows the results of modelling based on Equation 4.6 including both the positive and negative voltage ranges. The values of the physical parameters calculated are listed in Table 4.1. Both these parameters and the J–V traces show a marked polarity asymmetry. It should be noted that the calculated φ_{BPF} in Table 4.1 is different for positive and negative voltage. This originates from variation of injection current at different voltage polarities which will be explained in more detail in chapter 5. The expected value of the high frequency dielectric constant of $SrTiO_3$ is 5.8 [89] which is consistent with our calculated value of $\boldsymbol{\varepsilon}_r$.

Table 4.1: Calculated parameters used in Equation 4.6.

	φ_{BPF} (eV)	φ_{TAT} (eV)	ε_r
V > 0	0.90	0.13	7.0
V < 0	0.55	0.11	6.9

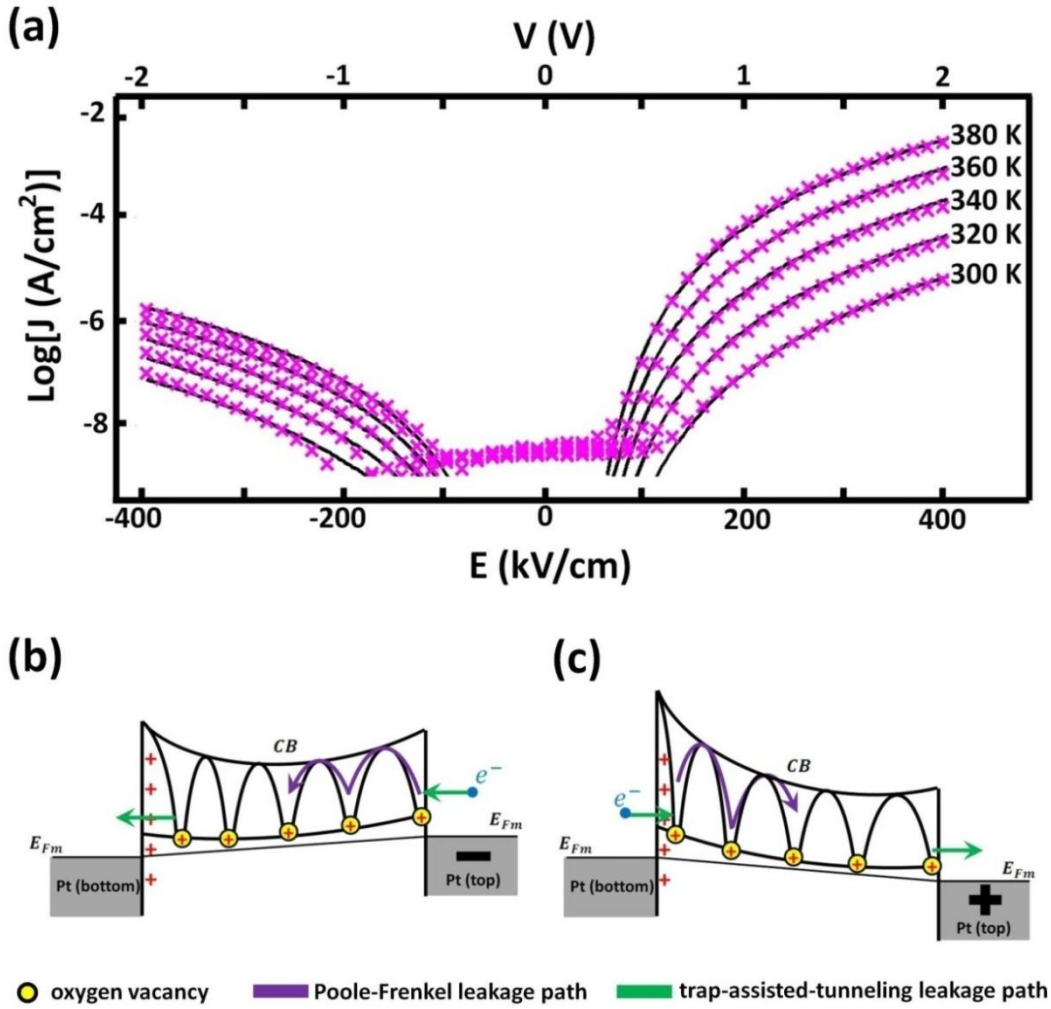

Figure 4.9: (a) Results of experimental matching based on Equation 4.6 at negative and positive voltage. (b) Negative voltage bias at top electrode and low injection of electrons to the bottom electrode due to high distance of oxygen vacancies from bottom electrode. (c) Positive voltage bias at top electrode and high injection of electrons to vacancies due to small distance between oxygen vacancies and bottom electrode.

4.5 C-AFM

Finally, the conduction through the oxide films has been examined, using C-AFM to resolve the uniformity of the leakage across the film. A typical C-AFM image is shown in Figure 4.10. There are clearly discrete points through which the leakage current passes most efficiently, which might arise from conductive filaments [68, 96, 97] through the dielectric. The filamentary conduction mechanism of $SrTiO_3$ is consistent with our assumption that the leakage current originates from the aligned oxygen vacancies from top to bottom electrode (Figure 4.11(a)). In order to also confirm the filamentary origin of *J–V* characteristics in Figure 4.3, we have investigated the *I–V* characteristic of each point.

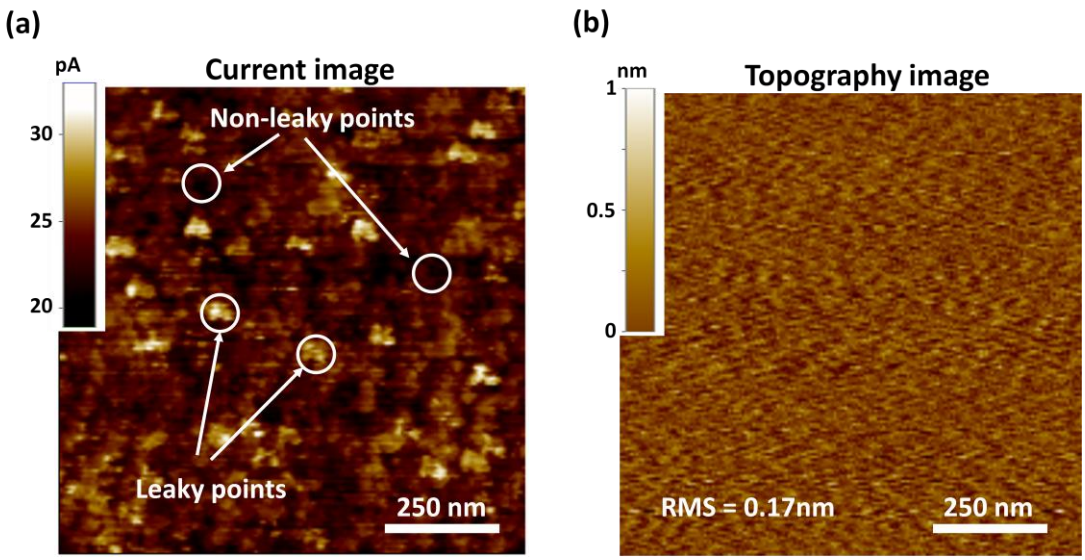

Figure 4.10: (a) The current image of $SrTiO_3$ surface, showing filamentary conduction through the film. (b) The topography image.

Single-point *I–V* measurement have been carried out by setting the location of AFM tip over a leaky and non-leaky points. Figure 4.11(b) shows the rectifying behaviour of a leaky point, with a comparatively small negative bias leakage current compared to the positive bias case. This is entirely consistent with *J–V* results that show a lower value of leakage current at negative bias. Non-leaky points show very low leakage current which cannot be detected by C-AFM. Therefore, it can be concluded that the main path of leakage current is through more conductive channels distributed across the dielectric film. At low voltage, there is a low injection of electrons to the oxygen vacancies near the bottom electrode (green paths in Figure 4.11(a)). By increasing the voltage, the high electron injection occurs at the bottom electrode where the thermionic emission of electrons between the oxygen vacancies limits the leakage current (purple paths in Figure 4.11(a)).

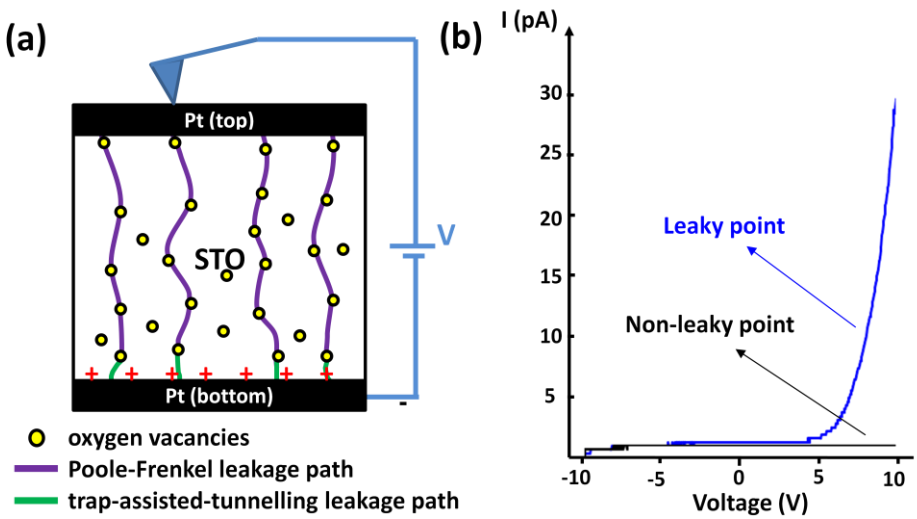

Figure 4.11: (a) Schematic path of leakage current through the aligned oxygen vacancies. (b) *I–V* characteristic of a single-point by sweeping the voltage on top of leaky and non-leaky points.

4.6 Positive charge trapped at the interface

It is important that the source of the asymmetry in *J–V* characteristics is identified. In the devices used in this study, it has been proposed that the difference between the characteristics with forward and reverse bias is produced by the existence of fixed positive charges at the bottom $SrTiO_3$/Pt interface. They give rise to an internal electric field at the interface which combines with the applied field. Figure 4.12 shows the *J–V* data for 300 K, which exhibits a minimum in the leakage current at a negative bias. At low negative bias, where the internal electric field is greater than the applied electric field, the current is in the direction opposite to that which would be generated by the applied field alone, as observed.

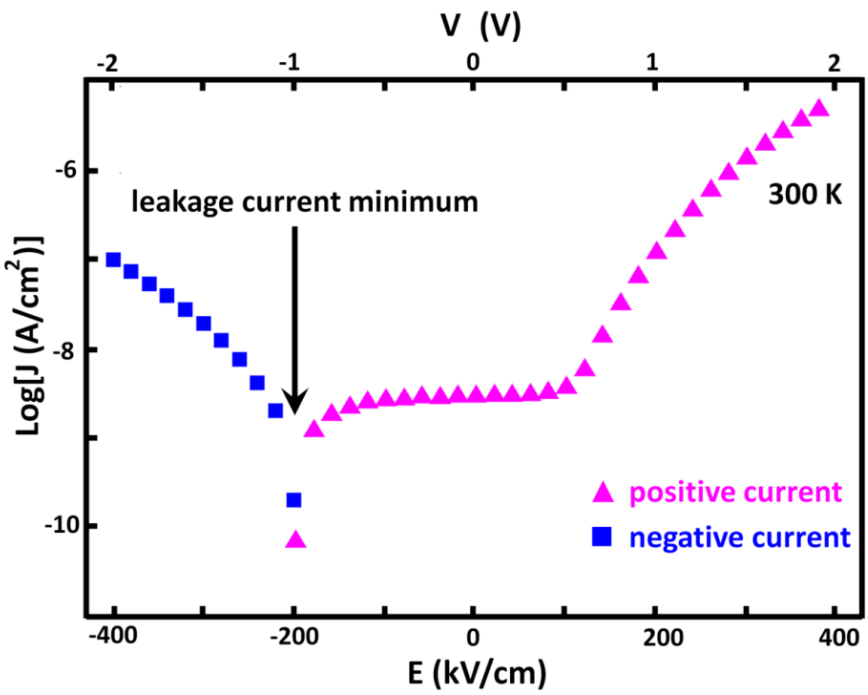

Figure 4.12: Different direction of current where the minimum of leakage current lie at negative voltage.

In the proposed model to explain the asymmetry (Figure 4.9), the fixed positive charges at the bottom electrode repel mobile electron donors, such as positively charged oxygen vacancies, increasing the distance between them and the electrode. Consequently, as outlined above, there will be a wider barrier to injection, and a concomitantly larger bias required to saturate the tunnelling injection of carriers into the oxide film. This is reflected in the *J*–*V* characteristics where at low voltage the injection current due to tunnelling is very low. This can also be viewed in terms of the combination of fixed and mobile positively charged defect centres. By increasing the positive voltage bias at the top electrode, positively charged mobile defects are pushed towards the bottom electrode. The positive bias tends to offset the repulsion from the fixed positive charges at the lower electrode, so the positively charged mobile defects are effective in producing a tunnelling current. In contrast, when a negative bias is applied, the mobile defects are directed away from the bottom electrode as the internal and external electric fields add to enhance the field driven diffusion. This results in an increase in the distance between the oxygen vacancies and the bottom electrode. Hence the electron tunnelling occurs at higher voltage. However due to the greater distances, the injection of electrons at negative voltage is always lower than for positive voltage. For the case of the top electrode, it differs from bottom electrode due to the different modes in which the two interfaces are synthesised. As a result, there is no fixed positive charge at the interface and as it is exposed to the atmosphere, oxygen vacancies can be created near this interface. Hence, the top electrode does not limit the injection of electrons to the deep traps.

4.7 Conclusions

The temperature dependence of the *J–V* characteristics of Pt/$SrTiO_3$/Pt structures were investigated from 300 to 380 K. It was found that the leakage current originates from the injection of electrons to deep traps, possibly oxygen vacancies near the interface, followed by thermionic field emission of electrons between the oxygen vacancies. In order to have an accurate model to explain the leakage current, it is necessary to consider the impact of both the interface and bulk. Therefore, a model has been proposed that combines both Poole-Frenkel and trap-assisted-tunnelling mechanisms in one equation that is able to model the experimental data quantitatively over the whole range of both positive and negative applied bias.

It is proposed that the asymmetry in the leakage current with respect to the bias direction is due to the varying distance of mobile electron traps, such as oxygen vacancies, from bottom electrode caused by the presence of a layer of fixed positive charge. This results in a variation in the injection rates of electrons at the two interfaces for a given bias.

In addition, C-AFM measurements strongly indicate a highly non-uniform conduction across the dielectric, demonstrating that the leakage current is predominantly through discrete channels, each of which exhibit asymmetric *I–V* characteristics consistent with the device *J–V* results.

Chapter 5

Bipolar Behaviour of $SrTiO_3$

'No amount of experimentation can ever prove me right; a single experiment can prove me wrong.'

Albert Einstein

5.1 Introduction

Resistive switching phenomena in metal oxide MIM structures have attracted significant attention for nonvolatile memory devices [36, 38], with the underpinning mechanisms thought to depend upon the material [11]. However, there are two main mechanisms in the literature, namely valance-change and thermo-chemical. The first concerns variation of the Schottky barrier height due to a change in the oxygen vacancy concentration at the metal/oxide interface that can be controlled electrically [98, 99], while the second involves electrically conducting filaments formed by diffusion of cations in or out of the metal oxide [37]. Although these models can explain many features of bipolar resistive switching in metal oxides, the relationship between the observed leakage current asymmetry and resistive switching of oxides

has not been clearly elucidated. This is partly caused by the asymmetry in leakage current being confused with the resistive switching behaviour of oxides [84, 85].

In chapter 4, a model has been proposed based on Poole-Frenkel as the main conduction mechanism through the bulk where the electron injection at the bottom electrode were affected by the formation of oxygen vacancies away from the interface. In this chapter, the resistive switching behaviour of $SrTiO_3$ is investigated in ALD and PLD deposited $SrTiO_3$ samples.

In section 5.2, the *J*–*V* characteristics of $SrTiO_3$ are presented using the same ALD deposited sample as for chapter 4. The voltage was swept in positive and negative directions, which demonstrates asymmetric *J*–*V* characteristics and bipolar resistive switching behaviour. In order to explain the underpinning mechanism of resistive switching, the previous model presented in chapter 4 is extended by considering the role of oxygen vacancies at the bottom electrode in more detail.

In section 5.3, the *J*–*V* characteristics of PLD deposited $SrTiO_3$ sample are presented. The resistive switching behaviour was observed at room temperature with a hysteresis curve that occurs only for positive voltages. The resistive switching is explained by the same mechanism used for section 5.2. The existence of positive charge trapped at the interface is a key assumption to explain occurrence of the hysteresis curve at the positive voltage. It is also suggested carbon contamination at the interface might be the origin of fixed positive charge trapped at the bottom electrode.

5.2 ALD $SrTiO_3$

5.2.1 Electrical results

The sample structure has been explained in section 4.2. Figure 5.1 shows *J–V* characteristics of the leakage current at temperatures between 280 K and 400 K. The voltage is swept at a constant rate from zero bias to +4 V, then to −4 V before returning to zero bias. An asymmetry in the leakage current was observed at all temperatures examined. The leakage current asymmetry increases with temperature. This can be seen by comparing the *J–V* curves at 280 K and 400 K. In addition, the leakage current curves exhibit a pronounced hysteresis between the forward and reverse sweep under both positive and negative directions of the bias variation, which increases with temperature.

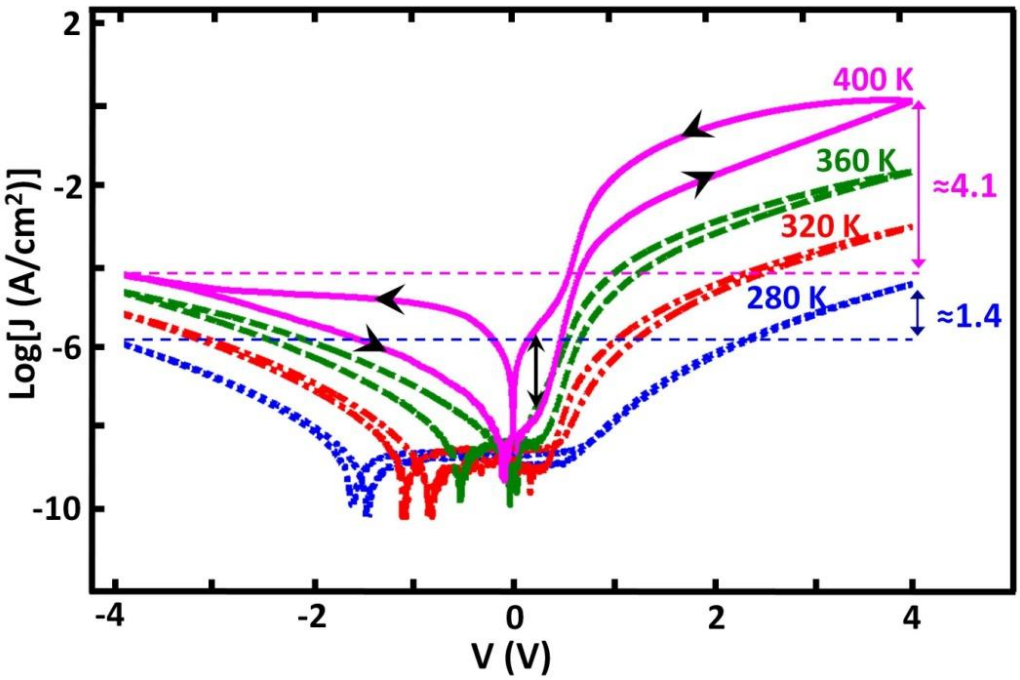

Figure 5.1: *J–V* characteristics for the $SrTiO_3$ MIM structures from 280 to 400 K.

5.2.2 Modelling the bipolar behaviour

In chapter 4, it has been proposed that the leakage current is through a pathway of oxygen vacancies from top to bottom electrode. The leakage current occurs by electron injection from one electrode to oxygen vacancies near the metal/oxide interface by tunnelling. This is followed by hopping conduction between oxygen vacancies by thermionic emission before tunnelling from oxygen vacancies into the other electrode (Figure 5.2). Due to the existence of positive charge trapped at the bottom electrode interface, the positively charged oxygen vacancies are electrostatically repelled, and in equilibrium they are located far from the bottom electrode. In this case, the tunnelling current limits the injection of electrons into the bulk, being highly sensitive to the proximity of oxygen vacancies to the bottom electrode.

In the proposed model, there is no fixed positive charge at the top electrode. This leads to the possibility of asymmetric electrical characteristics with respect to bias direction. The absence of the positive fixed charge at the top electrode allows oxygen vacancies to lie close to that interface, so that injection does not limit the leakage current there.

Figure 5.2: Illustrations of conduction mechanism under different voltage polarities.

In order to describe the processes underpinning resistive switching, the displacement and migration of oxygen vacancies at the bottom electrode are investigated. Displacement is defined as the reversible movement of oxygen vacancies under electrical bias, where upon removal of the applied voltage the oxygen vacancies return to their initial locations. Migration occurs when the field-driven movement of the vacancies is not reversible upon removal of the bias. At low temperature (Figure 5.3) (< 320 K), the oxygen vacancies cannot easily surmount the diffusion barriers. Application of a positive voltage bias displaces oxygen vacancies towards the bottom electrode, which enhances electron injection and increases the leakage current. A negative voltage displaces oxygen vacancies away from the bottom electrode, which suppresses electron injection. The displacement of oxygen vacancies at low temperatures leads to a small leakage current asymmetry; at 280 K the leakage current at −4 and +4 V differ by 1.4 orders of magnitude (Figure 5.1).

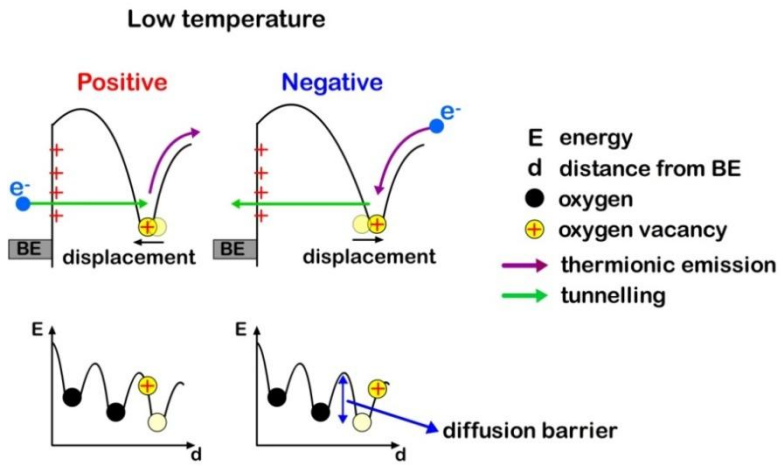

Figure 5.3: A model for the displacement of oxygen vacancies near the bottom electrode interface under an applied voltage at low temperature.

By increasing the temperature (Figure 5.4), there is more thermal energy, which increases the rate of migration. When the voltage increases from zero to positive values, the oxygen vacancies migrate towards the bottom electrode leading to a higher electron injection relative to low temperatures. At 400 K, by decreasing the voltage from +4 V to +0.5 V, the external electric force on oxygen vacancies reduces. Thus, the positive charge trapped at the bottom electrode interface repels the oxygen vacancies, leading to a reduction in leakage current by four orders of magnitude (Figure 5.1). However, while approaching zero bias there remains a remnant of the oxygen vacancy population close to the bottom electrode. When the voltage is swept to negative bias, this remnant is removed, so that upon return to low positive voltage from the negative bias the leakage current is significantly lower than when the remnant is present.

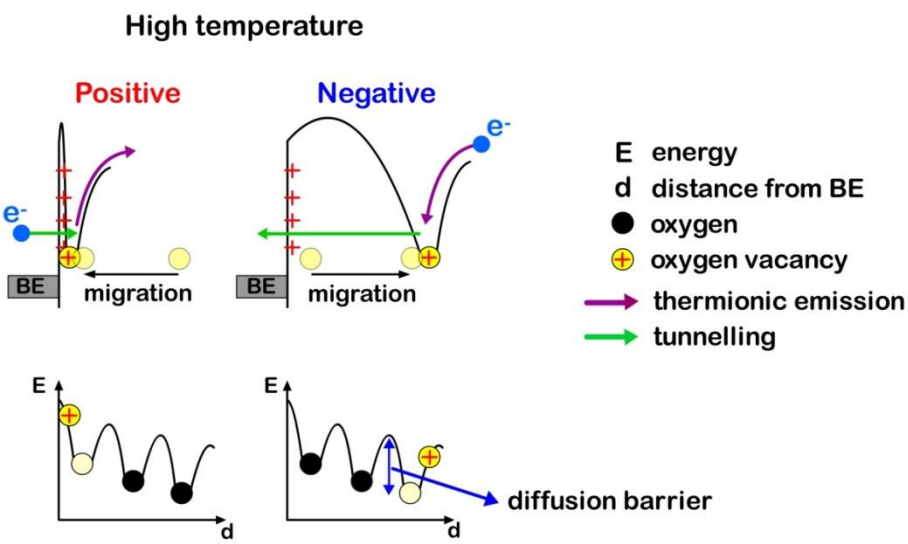

Figure 5.4: A model for the migration of oxygen vacancies near the bottom electrode interface under an applied voltage at high temperature relative to the onset of migration of oxygen vacancies.

This effect is indicated by the vertical arrow at +0.2 V in Figure 5.1 where there is a hysteresis of around two decades of current. As a result, when the applied voltage is swept from negative to positive, the leakage current does not follow the same path as it does when the voltage is swept from positive to negative, thus demonstrating hysteresis.

In order to examine this model, an experiment was carried out increasing the temperature from 300 K to 400 K and then back to 300 K with the DC voltage fixed at +4 V. The leakage current-density as a function of the changing temperature is shown in Figure 5.5. Initially it increases sharply in the range from 300 K to 400 K (from point a to b). Upon the subsequent reduction of the temperature under bias, the leakage current-density decreases (from point b to c), but does return to its initial value: there is nearly two orders of magnitude difference in the initial and final current densities at 300 K.

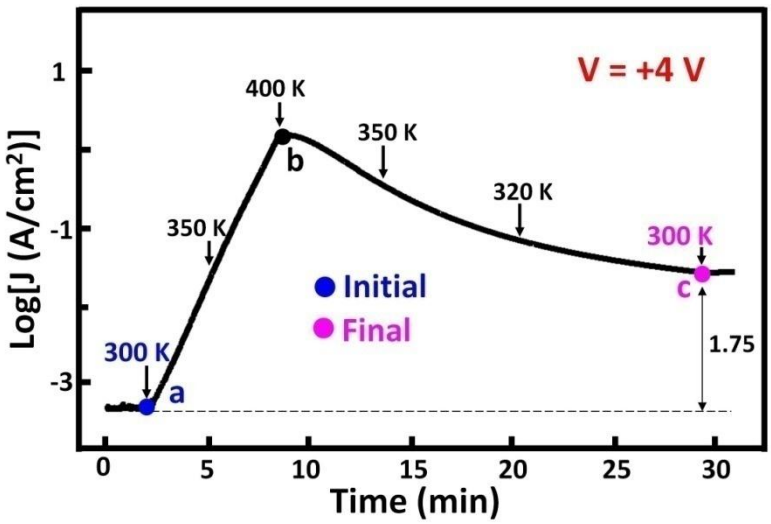

Figure 5.5: The leakage-current density at +4 V during the temperature variation from 300 K→400 K→300 K.

Figure 5.6 shows the initial and final leakage-current curves at 300 K, as well as the *J*–*V* curve at 400 K. The variation is interpreted as follows. Increasing the temperature under the fixed DC voltage of +4 V causes oxygen vacancies to migrate nearer to the bottom electrode interface. In the phase where the temperature is reduced to 300 K, the oxygen vacancies maintain their location closer to the bottom electrode interface due to the applied bias (Figure 5.7). As a result, the final injection current is greater than at the beginning. By comparing the final 300 K and 400 K *J*–*V* characteristics, it can be seen that at higher voltages the thermionic emission starts to dominate, causing divergence of the two *J*–*V* curves (Figure 5.6).

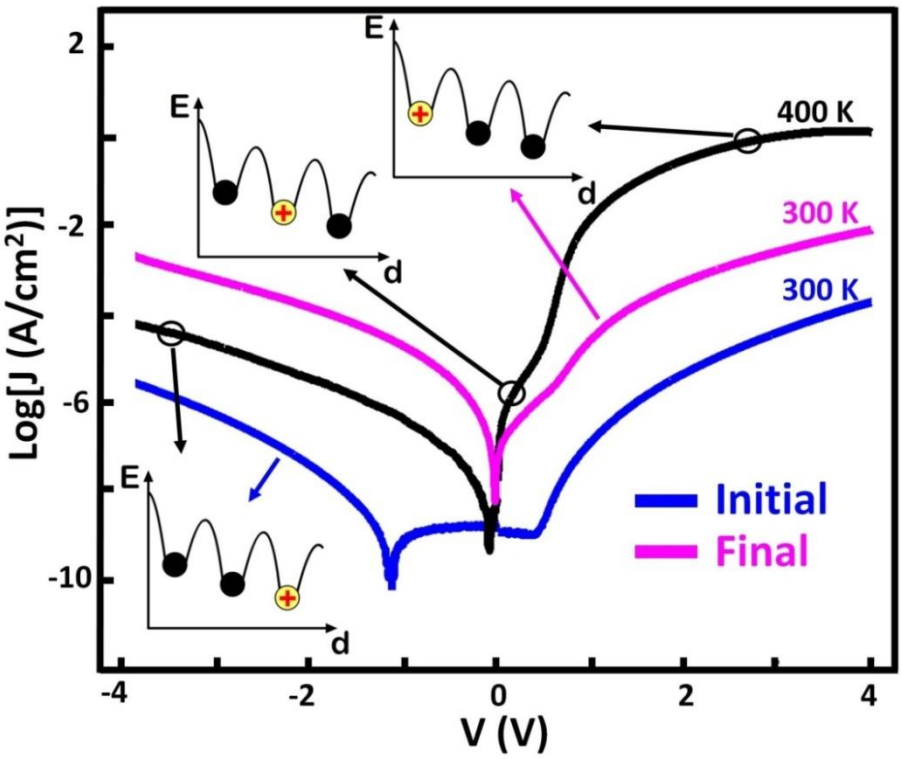

Figure 5.6: The leakage current at 300 K before and after the annealing cycle, and at the peak temperature of 400 K. Inset are illustrations of the model involving oxygen vacancies in relation to the bottom electrode.

Sweeping the voltage to negative values displaces the oxygen vacancies away from the bottom electrode interface. However at 300 K, subsequent to the thermal excursion to 400 K, the oxygen vacancies do not have sufficient energy to surmount the diffusion barriers. Therefore, migration does not take place and the electron injection is similar to that seen in the positive voltage sweep. Figure 5.6 shows that the leakage current at 300 K after the thermal cycle is almost symmetric, with only small differences between the positive and negative bias sides, probably due to oxygen vacancies displacement. It should be noted that under the negative voltage subsequent to the thermal cycle, the leakage current at 300 K is greater than at 400 K. This is interpreted as arising from the migration of vacancies at 400 K away from the bottom electrode, which reduces injection, but at 300 K after a thermal cycle under positive bias the vacancies are fixed at the bottom electrode interface, enhancing the injection (Figure 5.7).

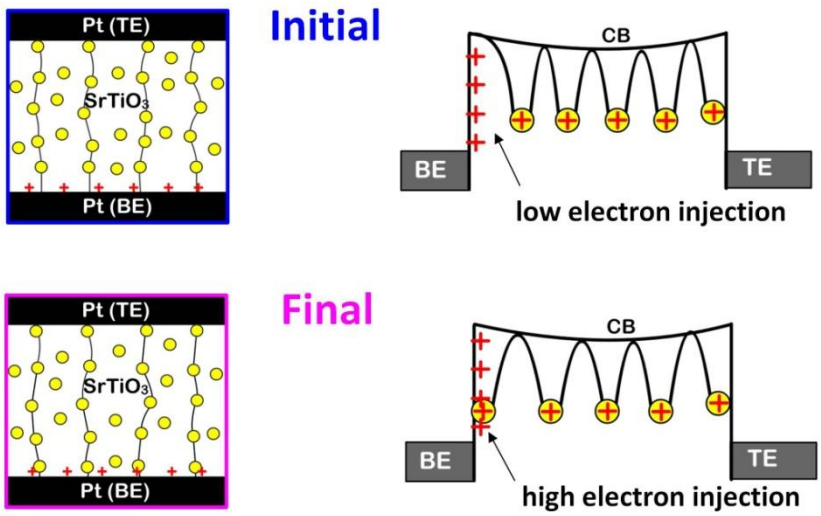

Figure 5.7: Oxygen vacancies locations in relation to the bottom electrode before and after annealing cycle.

5.2.3 Trap states of oxygen vacancies

In the conventional Poole-Frenkel equation (Equation 3.13) the injection at the interface is assumed to be high, with only thermionic emission of electrons between oxygen vacancies limiting the leakage current. In chapter 4, it has been demonstrated that the leakage current is affected by injection of electrons at the bottom electrode. The value of C in Equation 4.1 changes with voltage which was modeled by a trap-assisted-tunnelling equation (Equation 3.20). In trap-assisted-tunnelling, the locations of traps are assumed to be fixed and the applied voltage increases the leakage current by modifying the shape of the potential barrier.

In the previous section, it has been suggested that the leakage current is influenced by migration of oxygen vacancies relative to the bottom electrode. The applied voltage alters the tunnelling barrier height at the interfaces, by affecting the distance between the oxygen vacancies and the bottom electrode. As a consequence, the equation 4.6 is not accurate for high temperatures where there is migration of oxygen vacancies and the conduction mechanism must be presented as

$$J \approx C(T,V)\exp\left(-\frac{e\varphi_{\mathrm{T}}}{kT}\right) \tag{4.1}$$

where φ_{T} is the trap state of an oxygen vacancy below the conduction band and the parameter C depends upon both temperature and voltage. By increasing the temperature, the exponential term increases. However, at high temperature, the parameter C also changes by application of a voltage. In this case, the value of φ_{T} cannot be described by using an Arrhenius plot as the value of C is also dependent

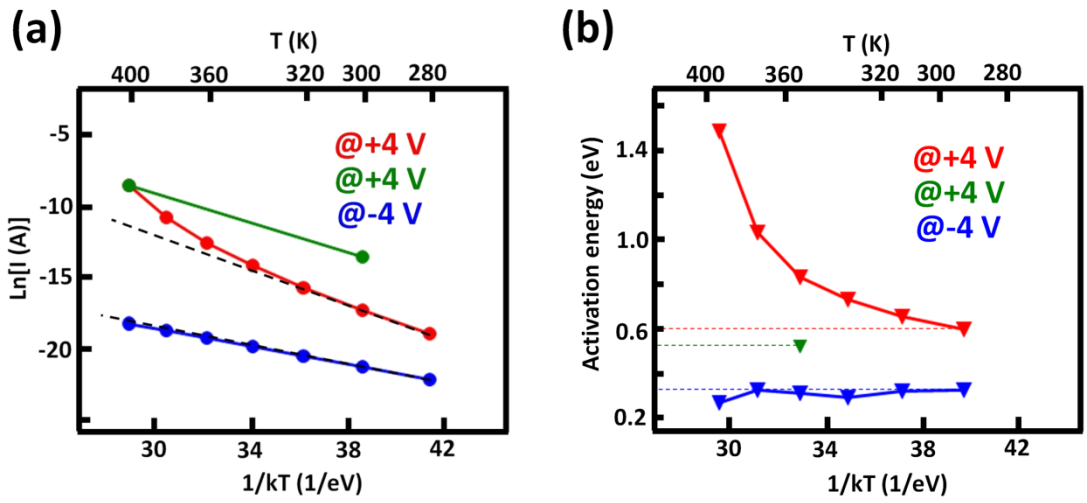

Figure 5.8: (a) The Arrhenius plot for figure 5.1 at voltage −4 and +4 V. (b) The activation energy plot.

upon temperature. This can be better understood by plotting the Arrhenius plot of *J–V* characteristics (Figure 5.8(a)). Although, the Arrhenius plot shows an almost linear behaviour for the leakage current at −4 V, the behaviour is nonlinear at +4 V. Figure 5.8(b) shows the variation of activation energy with temperature which is calculated from the Arrhenius plot. At low temperature, there is only a small displacement of oxygen vacancies towards the bottom electrode leading to the constant injection of electrons into the bulk. Therefore, *C* is a constant and Arrhenius plot shows a linear behaviour. However, by increasing the temperature, migration of oxygen vacancies towards the bottom electrode at positive voltage will increase electron injection at the interface. Therefore, not only the exponential term increases with temperature, but also the value of *C* increases. This can give rise to non-linear behaviour in an Arrhenius plot due to the variation of the prefactor *C* with temperature.

When the temperature decreases from 400 K to 300 K by keeping a DC voltage of +4 V on the top electrode, the oxygen vacancies maintain their location closer to the bottom electrode interface. At room temperature, the repulsive force of fixed positive charge trapped at the bottom electrode repels the oxygen vacancies away from the interface. However, the oxygen vacancies do not have enough thermal energy to surmount the diffusion barriers. As a result, by removing the DC voltage, the oxygen vacancies maintain their locations close to the bottom electrode similar to the case when a voltage of +4 V is applied at 400 K. In both cases, the oxygen vacancies are close to the bottom electrode and due to high electron injection at the interface, thermionic emission of electrons through the bulk controls the leakage current. The prefactor $C(T,V)$ is maximum and almost equal for both $C(300,+4)$ and $C(400,+4)$. Hence, the value of φ_T can be extracted from values of the leakage current at 400 K and 300 K (after thermal excursion). At these two points only the exponential term varies with the temperature. Therefore, from the slope of the green line created from leakage current values at 300 K and 400 K (Figure 5.8(a)) the activation energy is calculated to be −0.52 eV.

This also explains the difference between the calculated values of φ_{BPF} at negative and positive voltage biases in Table 4.1. At positive voltage, the migration of oxygen vacancies close to the interface leads to higher electron injection. Therefore, the value of φ_{BPF} at positive voltages is calculated to be greater than φ_{BPF} at negative voltages.

5.2.4 Activation energy of oxygen vacancies

The *J*–*V* characteristics of the sample that had received a thermal cycle under a fixed +4 V bias were investigated at temperatures between 300 K and 380 K. Figure 5.9 shows the impact upon the leakage current-density characteristics. The leakage current under positive bias increases with temperature in a fashion similar to the normal operation shown in Figure 5.1. However, the leakage current decreases over the $-4 < V < 0.5$ V range, an effect also observed by Shang *et al* [84]. This effect is explained by the same mechanism as proposed for the temperature dependence shown in Figure 5.6. By increasing the temperature, the oxygen vacancies can migrate away from the bottom electrode under negative bias, allowing them to move to their equilibrium locations. This reduces the injection of carriers, and therefore the leakage current.

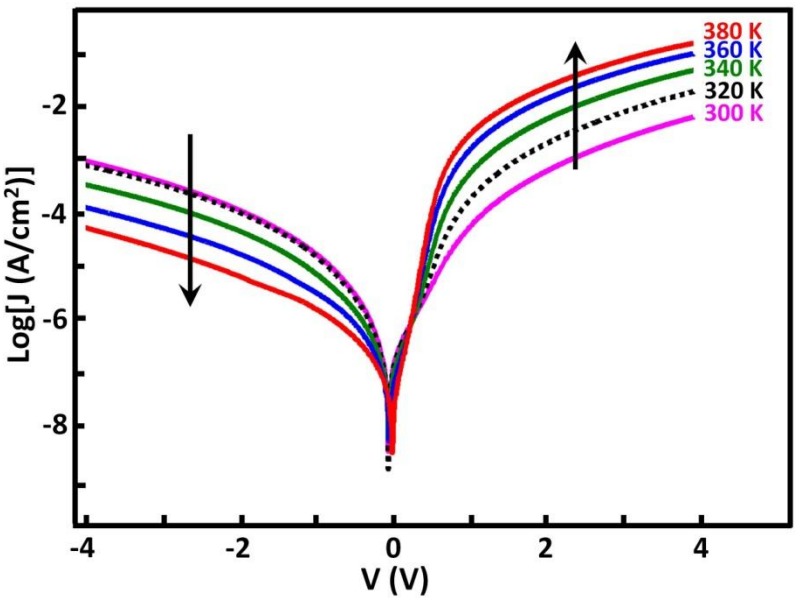

Figure 5.9: Effect of temperature on the leakage current density after annealing the MIM device at 400 K under a positive dc bias of +4 V.

In order to estimate the activation energy for the migration of oxygen vacancies, the experiment was repeated by increasing temperature from 300 K to 400 K and then back to 300 K with the DC voltage fixed at +4 V. After driving the oxygen vacancies near to the bottom electrode, the temperature was increased under a fixed −4 V bias. Figure 5.10 shows the variation in leakage current with temperature in this case. By increasing the temperature, the leakage current increases by enhancing the thermionic emission of electrons between the oxygen vacancies. However, above 340 K, oxygen vacancies begin to migrate away from the bottom electrode, leading to a reduction in the injection-current, which in turn reduces the leakage current. The onset of migration at around 340 K is followed by an abrupt decrease in the leakage current after 385 K, which is proposed to be due to a rapid migration of the majority of the population of oxygen vacancies.

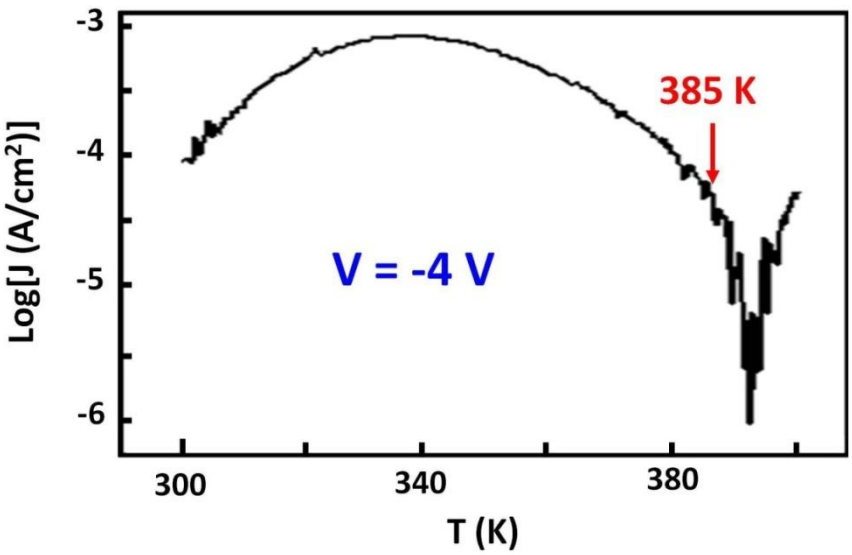

Figure 5.10: The leakage current variation by increasing temperature when the voltage of −4 V is applied on top electrode.

After the migration of oxygen vacancies, the injection current reduces to a constant value. Therefore, by increasing the temperature, the thermionic emission dominates current, due to a fixed value of injection current at the bottom electrode, which increases the leakage current. A rough estimate of the activation energy can be made by Urbach's approximation [100]

$$E_{\mathrm{T}} = 23kT \tag{5.2}$$

where E_{T} is the activation energy of oxygen vacancies. Using this equation, the activation energy lies between 0.67 eV (T= 340 K) and 0.76 eV (T=385 K). It should be noted that the calculated oxygen vacancies migration energy is 0.757 eV [101], consistent with our observation of rapid migration at 385 K.

5.3 PLD $SrTiO_3$

In section 5.2, the bipolar behaviour of an ALD grown $SrTiO_3$ sample was presented. The *J*–*V* characteristics showed asymmetry at all temperature examined, with resistive switching behaviour observed at elevated temperature. The asymmetry is explained by the relative lack of traps at one electrode, which is determined from symmetric *J*–*V* curve obtained at room temperature (Figure 5.6) due to the redistribution of the dominant electrical oxygen vacancies in the film.

In this section, the *J*–*V* characteristics of thin film $SrTiO_3$ grown by PLD are presented which show resistive switching behaviour at room temperature with a hysteresis curve under positive voltages. This behaviour cannot be categorised as bipolar behaviour as the resistive switching between high and low resistance only exists under positive voltage. The hysteresis of *J*–*V* characteristics cannot be explained by the previous models [36] where the formation and rupture of filaments occurs by changing the voltage polarity. We show that our model can not only explain the asymmetry and bipolar behaviour of the ALD $SrTiO_3$ sample, but it can also elucidate the hysteresis behaviour under positive voltages of $SrTiO_3$ grown by PLD. Furthermore, this behaviour supports the model of fixed positive charges trapped at the bottom electrode interface.

5.3.1 Experiment

A 100 nm thick Pt film was deposited on a Ti/SiO_2/Si substrate to act as the bottom electrode of the MIM structure. The 13 nm thick $SrTiO_3$ thin film was deposited on the Pt by PLD at a substrate temperature of 700 °C (Figure 5.11). The substrate was secured by silver paste onto the stainless-steel resistive heater. The target to substrate distance was set to 50 mm. The $SrTiO_3$ film was grown by laser ablation using a laser wave length of 248 nm and a stoichiometric $SrTiO_3$ target with a diameter of 20 mm. The substrate temperature during deposition was controlled using a thermocouple embedded in the heater. The sample thickness was measured using a Dektak 150 contact profiler. The circular Pt top electrodes of thickness 100 nm were deposited by electron beam evaporation, and patterned by a lift-off process. For electrical characterisation, the voltage was varied on the top electrode while the bottom electrode was grounded.

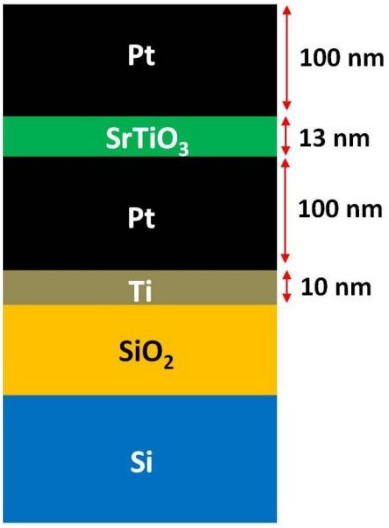

Figure 5.11: The sample sturture of 13 nm PLD $SrTiO_3$.

5.3.2 Electrical results

Figure 5.12 shows the *J–V* characteristic of the sample at room temperature. The voltage is swept from −1 to +1 V, followed by a reverse sweep from +1 to −1 V. There is a low leakage current when the voltage is swept from negative to positive values (Figure 5.12 (a, b)). However, as the voltage approaches +1 V, an abrupt increase in leakage current occurs (Figure 5.12 (c)). When decreasing the voltage, the leakage current stays at the high values (Figure 5.12 (d)) until a dramatic decrease occurs at a voltage around +0.2 V (Figure 5.12 (e)). By sweeping the voltage from 0 to −1 V, the leakage current is almost similar to the leakage current when the voltage was swept from −1 to 0 V (Figure 5.12 (f)). Therefore, the leakage current curve exhibits a pronounced hysteresis between the forward and backward sweeping under the positive voltage where the switching between low and high leakage current is on the order of 10^6.

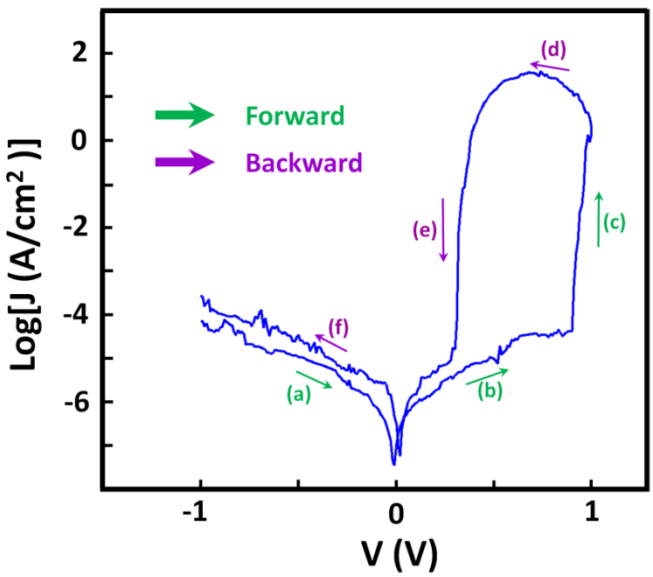

Figure 5.12: *J–V* characteristics for the 13 nm $SrTiO_3$ MIM structure at 300 K.

Figure 5.13 represents 50 switching loops, illustrating the repeatability of the *J–V* characteristic presented in Figure 5.12. The current compliance of 1 µA has been set to prevent the device from suffering permanent breakdown.

The resistance state of the device switches from a high resistance state to a low resistance state at ~0.7 V. By sweeping the voltage to zero, the resistance of the device will switch back to 'high' at ~0.2 V. The device maintains the high resistance state when the voltage is swept at negative values. The *J–V* characteristics demonstrate a good repeatability which can be realised by comparing the first loop (red curve) and fiftieth loop (black curve).

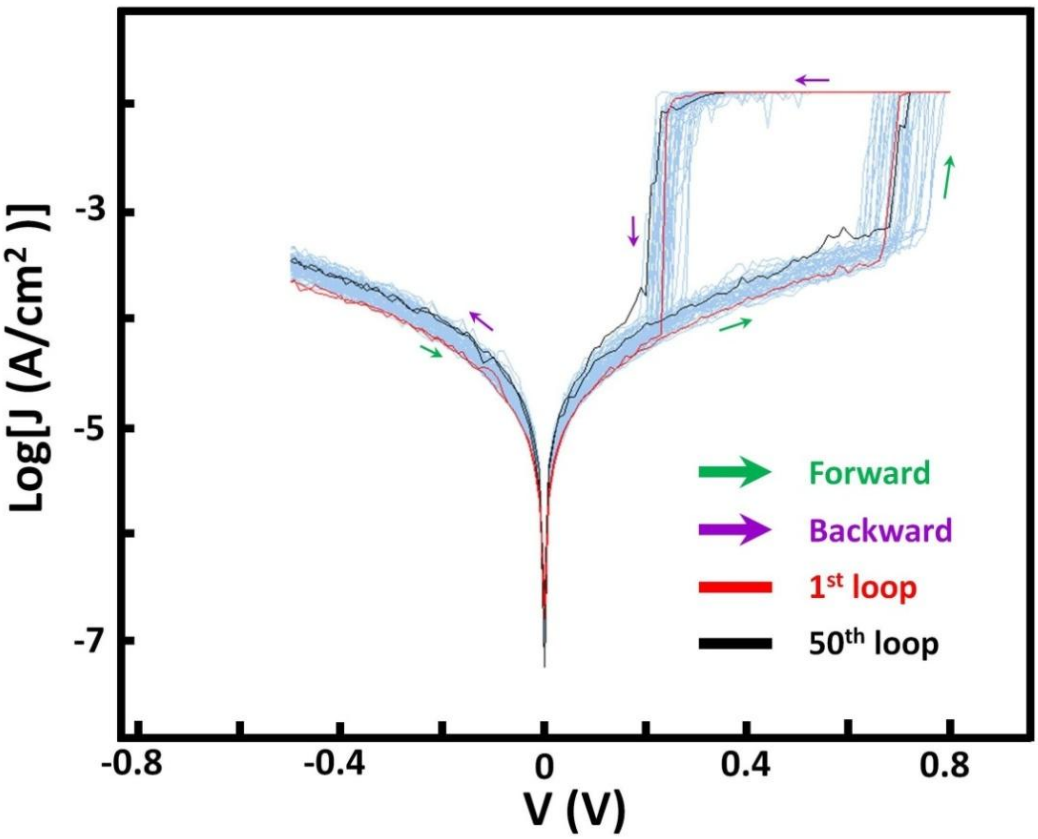

Figure 5.13: *J–V* charactersitics of $SrTiO_3$ for 50 consecutive sweeping loops.

5.3.3 Modelling

The leakage current of the ALD $SrTiO_3$ sample in section 5.2 was modelled based on electron injection from one electrode to the bulk, followed by thermionic emission between the oxygen vacancies before injection from the bulk to the opposite electrode. The presence of interfacial defects where the dielectric layer is nucleated, leads to the lack of oxygen vacancies at the bottom electrode, which limits the electron injection. The relative lack of oxygen vacancies at the bottom electrode originates from the positive charge trapped at the Pt/$SrTiO_3$ interface, repelling mobile oxygen vacancies. In this case, the tunnelling current at the bottom electrode controls the injection of electrons to the bulk, it being highly sensitive to the distance of oxygen vacancies from the bottom electrode.

The leakage current of the PLD sample in this section 5.3 demonstrates a similar behaviour, where the leakage current increases at positive voltage. However, the hysteresis loops only appear for positive voltages. In addition, the hysteresis loop in the ALD sample was only observed at 400 K while the PLD sample shows the hysteresis loop even at room temperature. This might indicate a lower diffusion barrier for oxygen vacancies in PLD $SrTiO_3$ which results in migration of oxygen vacancies upon application of a voltage bias at room temperature.

Figure 5.14 illustrates a model where an oxygen vacancy is located near the bottom electrode. The fixed positive charge trapped at the interface repels the oxygen vacancies away from the bottom electrode. A positive voltage on the top electrode

drives the oxygen vacancies close to the bottom electrode by cancelling the electric field due to the positive trapped charges. However, the diffusion barrier, E_{d1}, prevents migration of oxygen vacancies upon application of a voltage bias (Figure 5.14(a)). In this case, application of a positive voltage may only result in a displacement of oxygen vacancies towards the bottom electrode. When the applied voltage is enough to overcome both the repulsive force of positive trapped charge and the diffusion barrier E_{d1}, the migration of oxygen vacancies can occur. The threshold voltage of 0.7 V must surmount two things: the repulsive force of fixed positive charge trapped at the interface and the diffusion barrier of E_{d1}. Therefore, the threshold voltage compromises V_+ and V_{d1} which result in displacement and migration of oxygen vacancies close to the bottom electrode respectively.

$$V_+ + V_{d1} = 0.7 \qquad 5.3$$

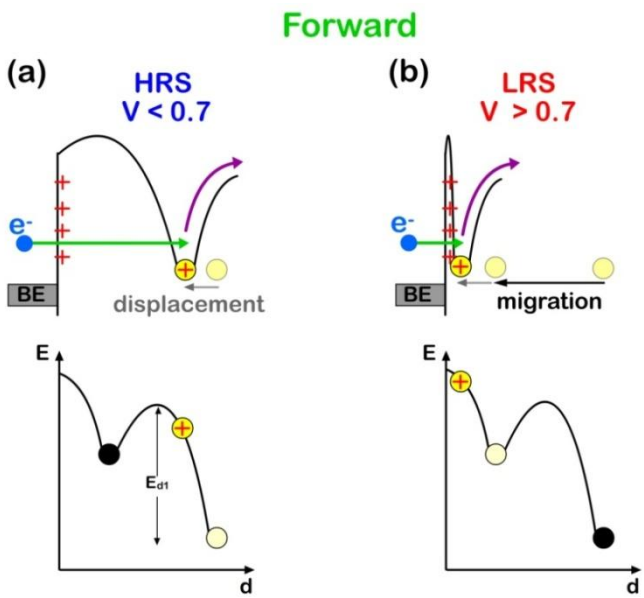

Figure 5.14: A model for the migration of oxygen vacancy near the bottom electrode interface when the voltage is swept from zero to positive values.

When migration occurs (Figure 5.14(b)), the applied voltage drives the oxygen vacancies close to the interface, leading to high electron injection into the bulk, which results in an abrupt transition from low to high leakage current values at ~0.7 V. When the voltage is swept back to zero, the repulsive force of the positive trapped charges repels the oxygen vacancies away from the bottom electrode (Figure 5.15(a)). However, the diffusion barrier of E_{d2} prevents the migration of oxygen vacancies back to their initial locations. When the voltage is reduced to 0.2 V, the repulsive force due to the fixed positive charges is enough to overcome both the applied voltage bias and the diffusion barrier of E_{d2}

$$0.2 + V_{d2} = V_{+} \qquad 5.4$$

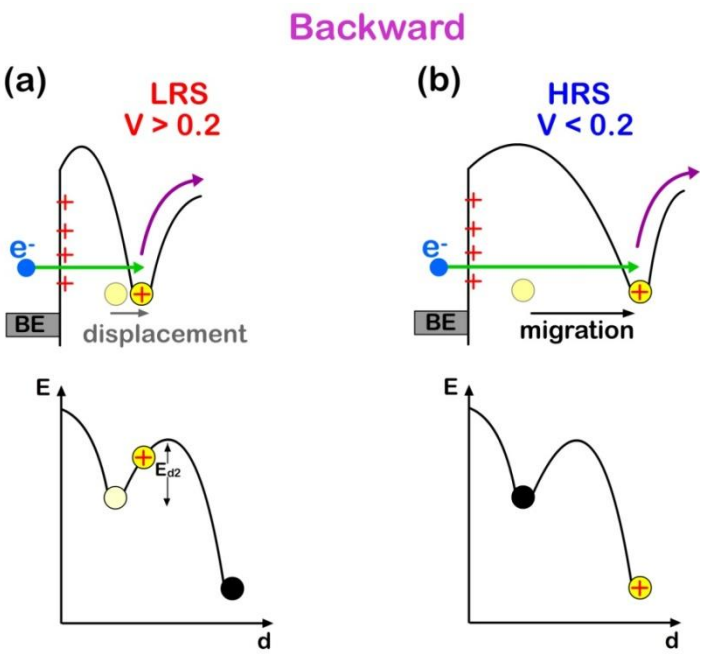

Figure 5.15: Migration of oxygen vacancy away from the bottom electrode interface when the voltage is swept from positive values to zero.

Therefore, the oxygen vacancies migrate to the equilibrium locations and the distance between the oxygen vacancies and the bottom electrode increases which results in a low electron injection (Figure 5.15(b)).

In Figure 5.14 and Figure 5.15 it has been assumed that $E_{\mathrm{d1}} > E_{\mathrm{d2}}$. In the next section, carbon contamination is suggested as the origin of positive charge trapped at the interface where it might modify the diffusion barriers of oxygen vacancies in a way that $E_{\mathrm{d1}} > E_{\mathrm{d2}}$. As a result, in equilibrium the oxygen vacancies are located away from the bottom electrode which is a critical assumption in our model.

5.3.4 Carbon as a positive charge trapped

The existence of positive trapped charges at the bottom electrode is a key assumption in the proposed model (Chapter 4) which explains the minimum leakage current shift to the negative voltage, asymmetry in leakage current and the hysteresis behaviour of leakage current under positive voltage sweeping. In order to reveal the structure or composition of the positive charge trapped at $SrTiO_3$/Pt interface, the XPS has been performed. Figure 5.16 shows the XPS depth profile obtained from 5 s etch cycle through the $SrTiO_3$ until approaching the Pt bottom electrode. The dashed line approximately indicates the $SrTiO_3$/Pt interface where the Pt concentration starts to increase.

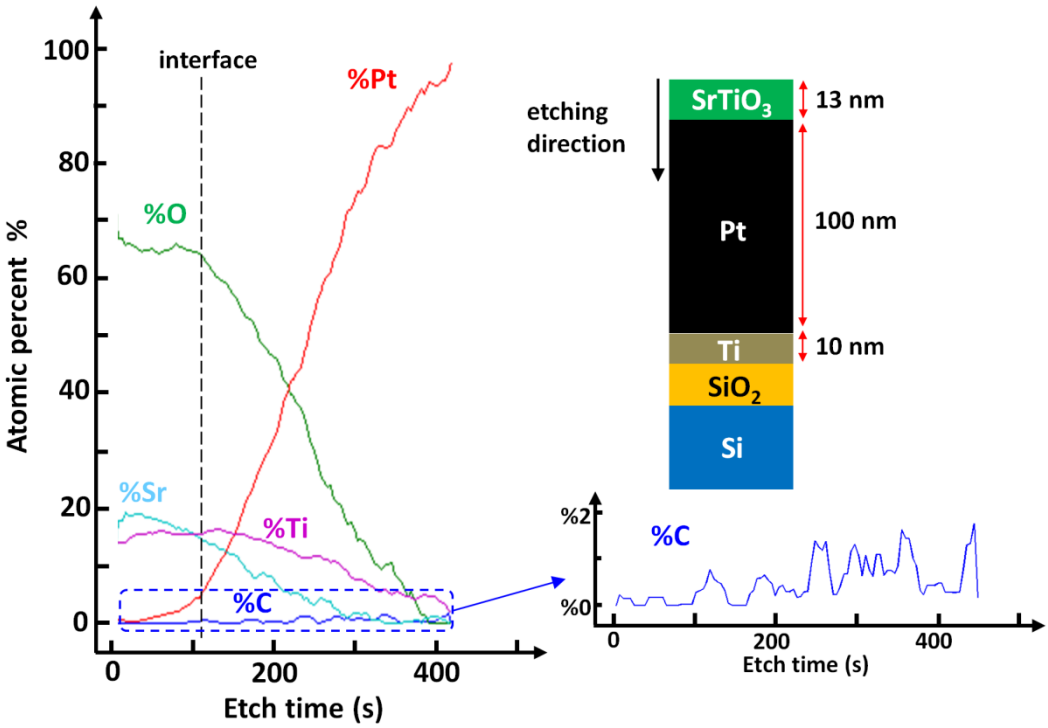

Figure 5.16: XPS depth profile result through the $SrTiO_3$ and Pt bottom electrode.

The XPS results show the existence of carbon contamination at the $SrTiO_3$/Pt interface which might be introduced from the crucible during the electron-beam deposition of Pt [62]. The XPS results might suggest a role for carbon as a fixed positive charge trapped at the interface.

In the absence of carbon at the interface, the oxygen vacancies lie close to the interface which results in a high electron injection at both the top and bottom electrodes (Figure 5.17(a)). Presence of carbon at the interface modifies the diffusion barrier of oxygen vacancies and repels them away from the bottom electrode which results in a gap with no oxygen vacancies at the interface (Figure 5.17(b)). As a result, the leakage current is dominated by electron injection at this interface.

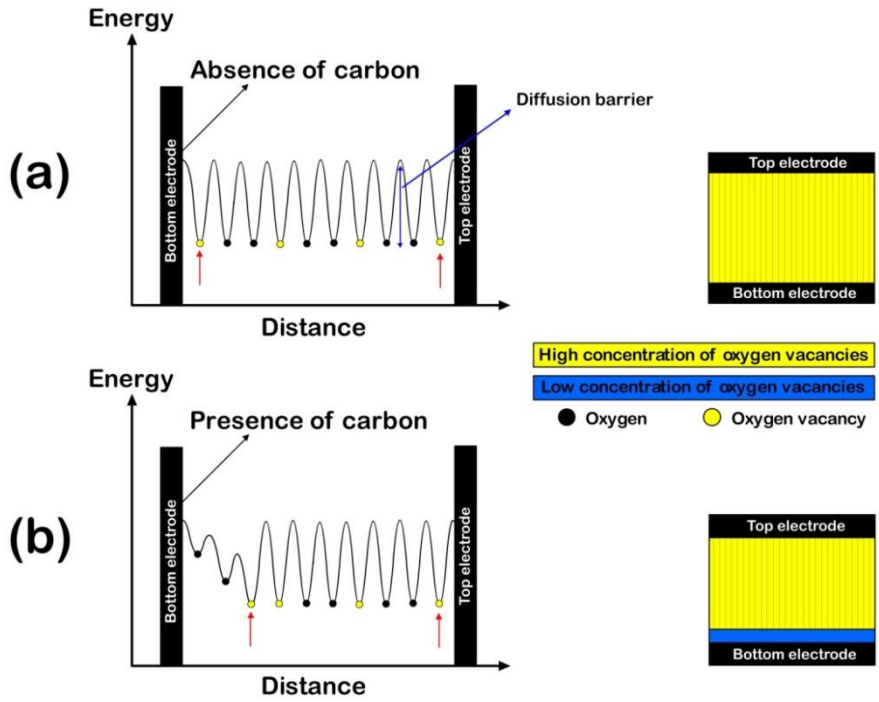

Figure 5.17: (a) Absence and (b) presence of carbon contamination at the bottom electrode interface.

It is worth noting that in both ALD and PLD samples, the injection current does not change during the negative voltage sweep and it only increases when a positive voltage is applied. For the ALD sample, this can be seen in Figure 5.8(b) where the activation energy at −4 V is almost constant while it increases at +4 V nonlinearly. For the PLD sample, when the sweeping voltage is negative, the values of leakage current are similar in magnitude to the low leakage current values at positive voltage (Figure 5.12). This might imply that the migration of oxygen vacancies away from the bottom electrode is negligible under negative bias voltage and the low concentration of oxygen vacancies does not increase (blue area in Figure 5.17(b)). When a positive voltage is applied, the low concentration of oxygen vacancies area decreases which results in a high electron injection current to the bulk.

Alternatively, upon application of voltage, there must be a smaller migration of oxygen vacancies through the bulk (yellow area in Figure 5.17(b)). The bulk is highly conductive relative to the interface and conductivity of the bulk does not change significantly by application of voltage. This suggests that in the absence of carbon at the interface (Figure 5.17(a)) there would be a high leakage current through the MIM structure. The distribution of oxygen vacancies does not change through the bulk by application of a voltage bias due to the high diffusion barrier of oxygen vacancies. The carbon contamination at the interface modifies the diffusion barrier of oxygen vacancies in the vicinity of carbon as illustrated in Figure 5.18.

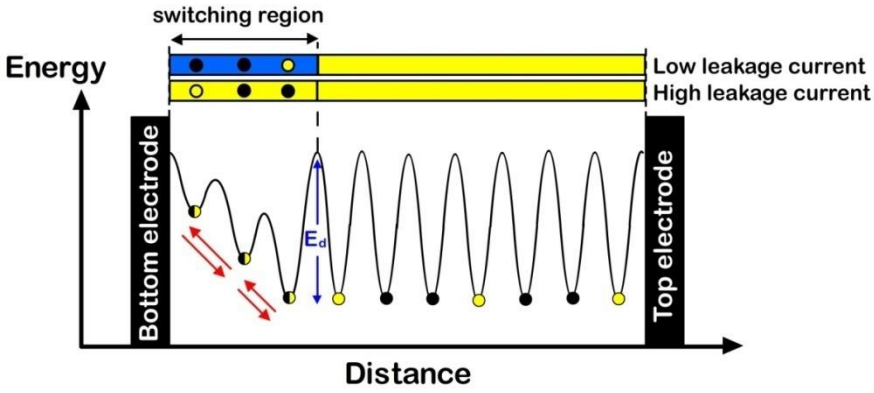

Figure 5.18: Illustration of oxygen vacancies migration only at the bottom electrode.

Therefore, the oxygen vacancies are formed far from the bottom electrode, generating an area with a low concentration of oxygen vacancies which is depicted by blue colour in Figure 5.17(b). Now, the oxygen vacancies can migrate close to the interface due to the low diffusion barriers. In this case, the switching from high to low resistance states occurs by driving the oxygen vacancies close to the interface by the application of positive voltage. When a negative voltage is applied the oxygen vacancies migrate away from the bottom electrode to their equilibrium position, causing a reduction in electron injection. The migrations can happen even at low positive bias where the repulsive force of positive charge, trapped at the interface, is sufficient to repel the oxygen vacancies. As a result, the switching occurs by migration of oxygen vacancies only in a few layers of $SrTiO_3$ in the vicinity of carbon contamination at the bottom electrode (Figure 5.18). By increasing the voltage in the negative direction, no further migration of oxygen vacancy occurs away from the bottom electrode due to the high diffusion barrier, E_d, depicted in Figure 5.18.

5.3.5 C-AFM

In section 4.5 the filamentary conduction paths of the ALD sample have been found to originate from the aligned oxygen vacancies from top to bottom electrode. In order to examine the filamentary conduction mechanism of the PLD sample, C-AFM has been carried out on the sample. Figure 5.19(a) shows a typical current image which has been obtained by scanning the $SrTiO_3$ surface when a positive voltage of 10 V was applied between cantilever's tip and the Pt bottom electrode. There are clearly discrete leaky points which indicate the similar filamentary mechanism of leakage current as has been observed for the ALD sample.

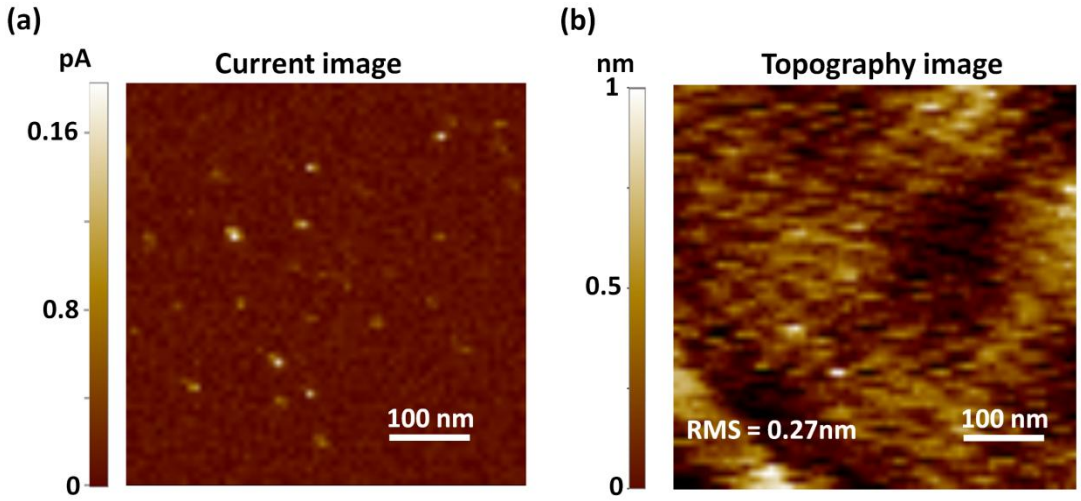

Figure 5.19: (a) The current image of PLD $SrTiO_3$ surface, showing the leakage current through the discrete points. (b) The topography image.

In order to confirm that the resistive switching (Figure 5.12) originates from these conductive spots, single-point *I–V* measurements have been carried out. The AFM tip was located over a leaky and non-leaky points. The sweeping voltage was between −10 V and +10 V in both directions across the AFM tip and the Pt bottom electrode. Figure 5.20 shows the resistive switching behaviour of a conductive spot, where the switching occurs only under the positive voltage. This is entirely consistent with macroscopic *J–V* characteristics (Figure 5.12) that show a hysteresis curves at the positive bias. The non-leaky point shows low leakage of current where there is no resistive switching. Therefore, the switching electrical resistance of individual filaments in $SrTiO_3$ are the main origin of resistive switching. The filaments are constructed from aligned oxygen vacancies where the migration of oxygen vacancies at the end of the filaments switch the resistance of the MIM structure between high and low resistance states.

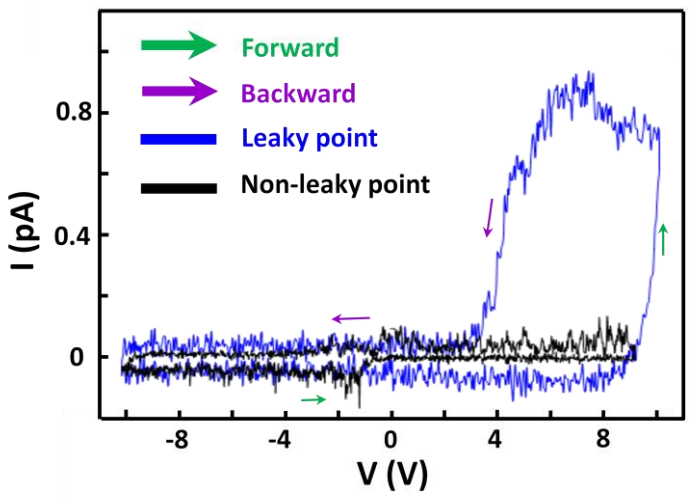

Figure 5.20: The electrical resistance of individual leaky and non-leaky points by sweeping the voltage from −10 V and +10 V.

5.4 Conclusions

The resistive switching in $SrTiO_3$ MIM devices was investigated. By constructing a simple model based upon the movement of electrically active point defects, it is possible to account for all the key features observed. A critical condition is that the leakage current is sensitive to the distance of oxygen vacancies from the bottom electrode due to the positive charge trapped at the interface. The asymmetry of leakage current originates from the displacement of oxygen vacancies relative to the bottom electrode, depending upon the temperature and applied bias. At high temperatures, oxygen vacancies' migration towards the bottom electrode leads to the resistive switching behaviour observed in leakage current, with oxygen vacancies driven to the bottom electrode resulting in a symmetric *J*–*V* curve at room temperature.

The resistive switching has also been observed in a PLD $SrTiO_3$ sample. At high voltage bias, the oxygen vacancies are driven close to the interface. However, by reducing the voltage, the repulsive force between the oxygen vacancies and the fixed positive charge trapped at the interface causes the migration of oxygen vacancies to equilibrium locations away from the bottom electrode. The fixed positive charge trapped might originate from the existence of carbon at the bottom electrode interface which modifies the diffusion barrier of oxygen vacancies in the vicinity of the electrode interface. The resistive switching occurs by the migration of oxygen vacancies only in just a few layers of $SrTiO_3$ at the bottom electrode interface.

Chapter 6

Antipolar Behaviour of $SrTiO_3$

'In science the credit goes to the man who convinces the world, not to the man to whom the idea first occurred.'

Sir Francis Darwin

6.1 Introduction

In the pursuit of emerging non-volatile memory devices, metal oxides have shown significant promise [36, 102, 103]. Ideal memory characteristics should display low power-consumption, fast programming, non-destructive readout, high-density integration, and low fabrication-cost. RRAM devices have attracted considerable attention due to exhibiting most of these features [11, 24, 104]. A RRAM cell is constructed using MIM structure, where the insulator is typically constituted from metal oxide dielectrics. The resistivity of metal oxides can be electrically switched between a low resistance state and high resistance state, where the current-voltage (*I*–*V*) characteristics exhibit a pronounced hysteresis.

Several models have been proposed to explain the underpinning mechanisms of hysteresis in *I–V* characteristics in metal oxides. The models cover a wide range of chemical and physical mechanisms, but it has proven difficult to find a simple unified model. However, the hysteresis in *I–V* characteristics can be broadly grouped into two main categories: bipolar and unipolar resistive switching.

As explained in chapter 2, in bipolar resistive switching, the switching depends upon the polarity of the applied voltage (*V*). A cell can be set to the low resistance state by $V > +V_{set}$ or reset to the high resistance state by $V < -V_{reset}$ (Figure 6.1(a)). In contrast, during unipolar resistive switching, the switching depends only on the amplitude of the applied voltage, and not the polarity. Figure 6.1(b) shows a schematic for unipolar resistive switching, where the oxide resistance can be reset to the high resistance state by applying $V_{reste} < |V| < V_{set}$. The low resistance state is then achieved via application of $|V| > V_{set}$. Several binary oxides (Appendix 1) have been reported to show unipolar and/or bipolar resistive switching. Bipolar resistive switching behaviour has been also observed in perovskite structure metal oxides [105].

In this chapter, resistive switching in Pt/$SrTiO_3$/Pt MIM structures is reported with switching characteristics that cannot readily be categorised as either bipolar or unipolar resistive switching. The *I–V* characteristics show that the resistive switching depends on both the polarity and amplitude of the applied voltage (Figure 6.1(c)). The $SrTiO_3$ resistance can be reset to the high resistance state by application of a high voltage with either polarity. A voltage of the opposite polarity to that used to

generate the high resistance state sets the low resistance state. Thus, if a high positive voltage has reset the device, the polarity of the set voltage must be negative.

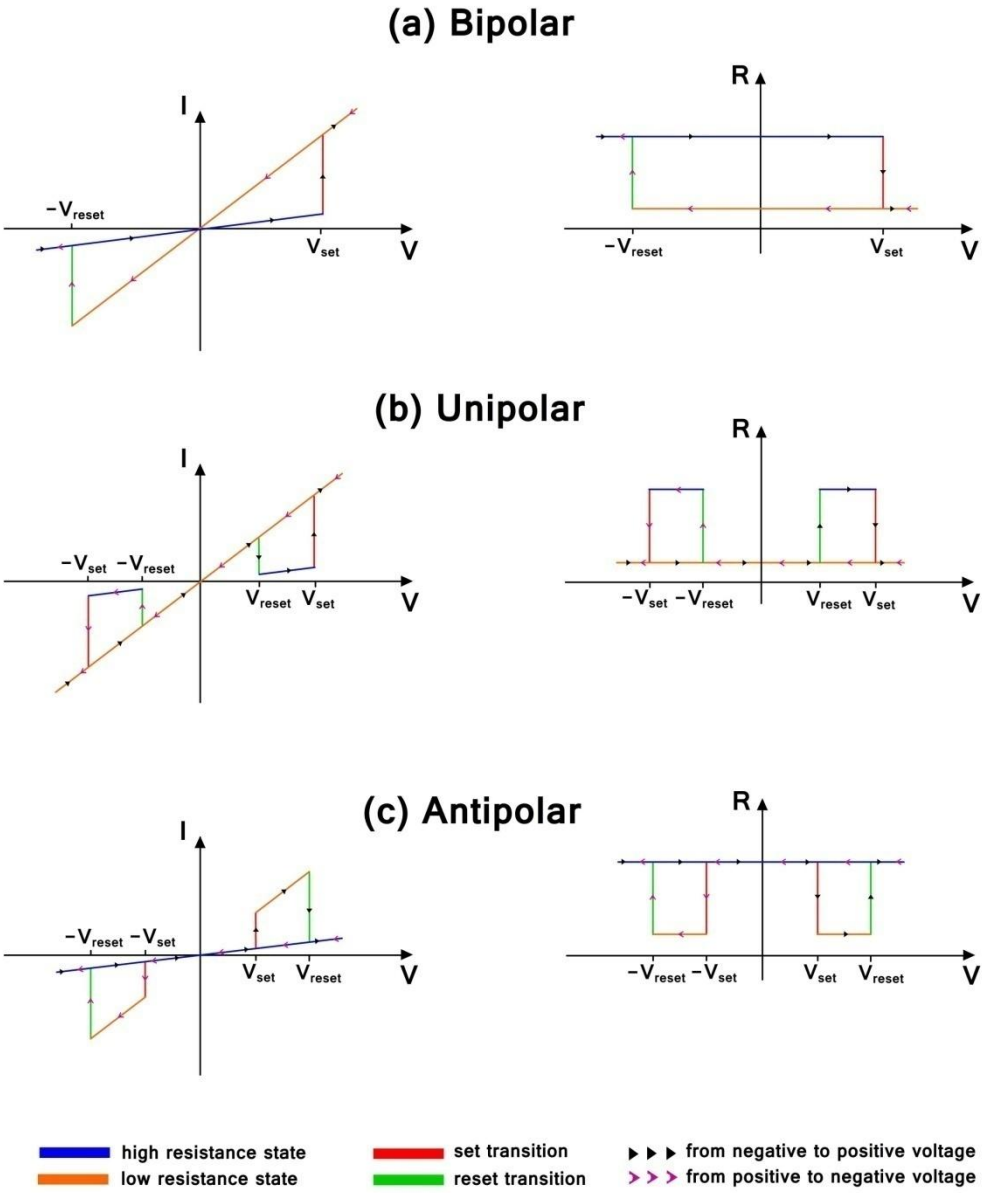

Figure 6.1: Schematic representations of the ideal *I–V* and *R–V* hysteresis behaviour of (a) bipolar resistive switching (b) unipolar resistive switching, and (c) antipolar resistive switching.

Similarly, if the reset voltage was negative, the polarity of set voltage must be positive. This behaviour is called antipolar resistive switching due to the opposite polarity of the set voltage with respect to previous reset voltage.

The differences between the operation of bipolar, unipolar, and antipolar resistive switching devices are summarised in Table 6.1. The contrast between the set and reset voltage magnitudes and polarities shows that the antipolar behaviour of the $SrTiO_3$ devices characterised in this study do not follow either the bipolar or unipolar behaviour of oxides. In this chapter, the conduction mechanism proposed in chapter 4 is used to explain the antipolar resistive switching behaviour of $SrTiO_3$. This conduction mechanism is based on electron injection from the electrode to trap states near the interface by tunnelling, followed by hopping conduction between traps via thermionic emission, supported by a simple mathematical frame work that quantitatively supports the conduction model.

Table 6.1: Characteristics of bipolar, unipolar and antipolar resistive switching in terms of the conditions required to set the devices to the low resistance state, and reset to the high resistance state.

	Reset voltage	**Set voltage**	$\mathbf{V_{set} \Leftrightarrow V_{reset}}$
Bipolar	$V < -V_{reset}$	$V > +V_{set}$	$V_{set} \sim V_{reset}$
Unipolar	$V_{set} < \lvert V \rvert < V_{reset}$	$\lvert V \rvert > V_{set}$	$V_{set} > V_{reset}$
Antipolar	$\lvert V \rvert > V_{reset}$	If $V > +V_{reset}$: $-V_{reset} < V < -V_{set}$ If $V < -V_{reset}$: $V_{set} < V < V_{reset}$	$V_{set} < V_{reset}$

6.2 Experiment

A 100 nm thick Pt film was deposited on a $Ti/SiO_2/Si$ substrate to act as the bottom electrode in the MIM structure (Figure 6.2). A 25 nm thick $SrTiO_3$ thin film was deposited on the Pt by PLD at a substrate temperature of 700 °C. The $Pt/Ti/SiO_2/Si$ substrate was secured by silver paste onto the stainless-steel resistive heater with a target to substrate distance of 50 mm. The $SrTiO_3$ film was grown by laser ablation (Neocera PLD system with a Lambda Physik KrF laser, λ = 248 nm) using a 20 mm diameter stoichiometric $SrTiO_3$ target in an oxygen pressure of 300 mTorr. The substrate temperature during deposition was controlled using a thermocouple embedded in the heater. The energy density of the laser spot (1.5×8 mm^2) was 1.2 J/cm^2, while the laser pulse repetition rate was 8 Hz. Once the ablation was over, the sample was cooled down at a rate of 10 °C/min in an oxygen rich environment (700 Torr). The sample thickness was measured using a Dektak 150 contact profiler. The Pt top electrodes (100 nm) were deposited by electron beam evaporation, and patterned by a lift-off process for electrical characterisation.

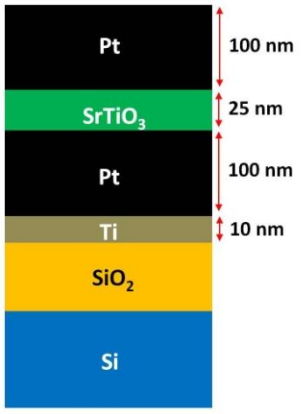

Figure 6.2: The sample sturture of 25 nm PLD $SrTiO_3$.

6.3 Electrical results

Figure 6.3 represents 100 switching loops, illustrating the repeatability of the resistive switching behaviour. The voltage was swept from −3 to +3 V (green arrows) followed by reverse sweeping from +3 to −3 V (purple arrows). There is a clear resistive switching around two decades of current that is indicated by the vertical arrow at ±0.5 V. The *J*–*V* characteristics demonstrate a good endurance which can be realised by comparing the 1st loop (red curve) with the 100th loop (black curve). The cycling between the low and high resistance state can be characterised by switching in the following fashion.

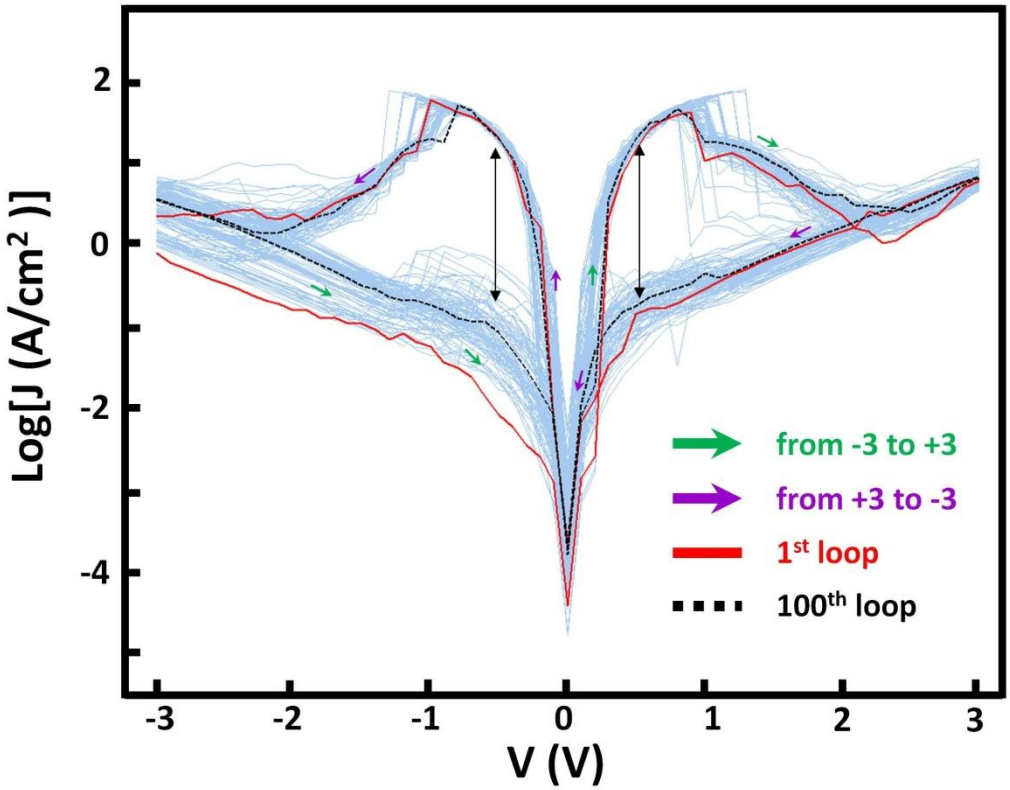

Figure 6.3: *J-V* characteristics of SrTiO3 for 100 consecutive sweeping loops between –3 and +3 V.

By increasing the positive bias from zero, the $SrTiO_3$ resistive state changes from high resistance state to low resistance state with $V > +0.2$ V, as shown in Figure 6.4. As the bias is further increased, the $SrTiO_3$ switches to the high resistance state at ~1 V. Subsequently, during reduction of the bias to zero the device remains in the high resistance state.

From zero bias, the sweeping of the voltage in the opposite direction results in switching to the low resistance state at $V < -0.2$ V. In accord with the magnitude of the reset voltage in positive bias, the device is switched to the high resistance state around −1 V, and the device remains in the high resistance state until a 'set' voltage of > +0.2 V is applied.

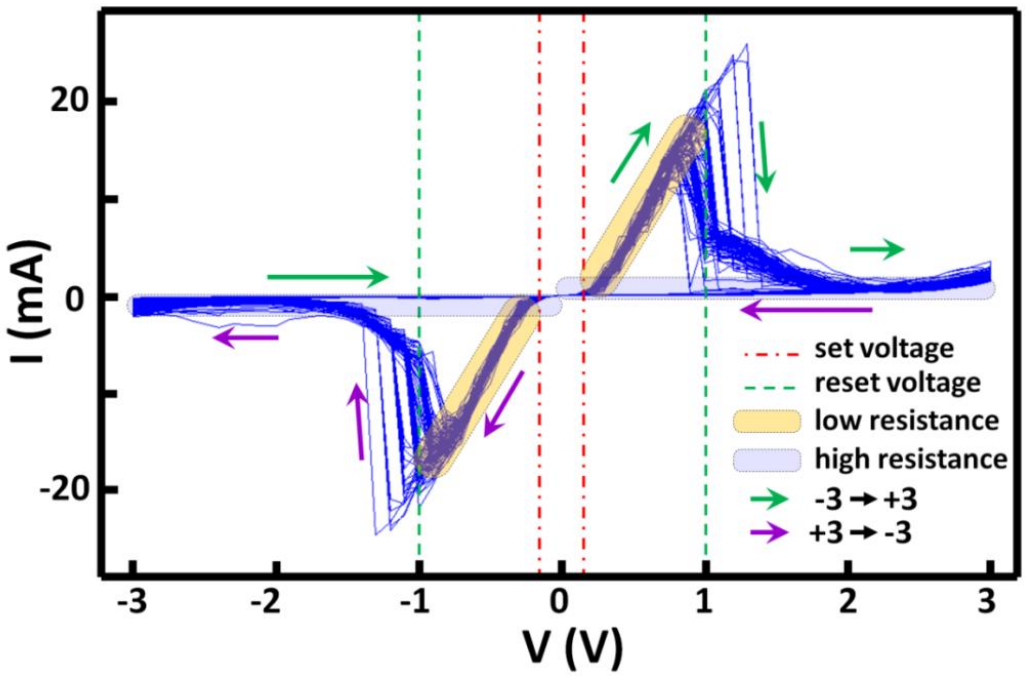

Figure 6.4: The *I–V* characteristcs in the antipolar resistive switching behaviour of the Pt/$SrTiO_3$/Pt MIM structure.

In order to further rule out bipolar and unipolar resistive switching, the device has been cycled 25 times in three different bias ranges (Figure 6.5). The voltage cycling in the high resistance state only with a positive polarity between $0 < V < 2.5$ V (red curves) shows no hysteresis. Since the resistive state of the structure does not change with the magnitude of the bias, the resistive switching behaviour is not unipolar. Similar behaviour is observed sweeping the voltage with negative polarity (green curves). The $SrTiO_3$ shows the same resistance for either polarity of voltage which is in contrast with bipolar resistive switching where the resistive state of the structure is switched by changing the polarity of the voltage, and as a result bipolar resistive switching is also ruled out.

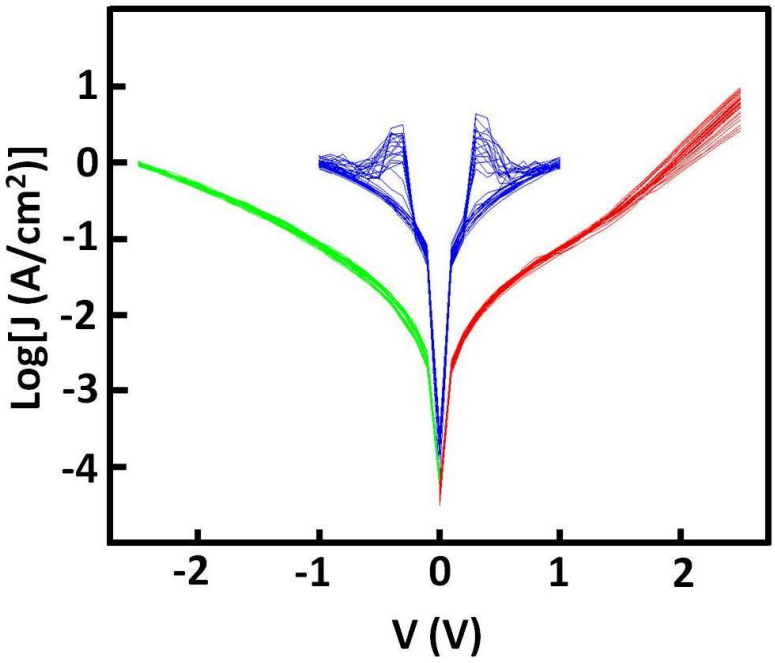

Figure 6.5: Current-density–voltage characteristics for 25 cycles under different conditions: positive bias (red curves), negative bias (green curves) and $-1 < V < +1$ V (blue curves).

By cycling the voltage over the range $-1 < V < +1$ V (blue curves) the $SrTiO_3$ is in the low resistance state because the device is never exposed to the reset threshold voltage, and although there is some hysteresis, it is much less significant than that seen in the large voltage range (Figure 6.3).

After each set of experiments depicted in Figure 6.5, the resistive state of $SrTiO_3$ has been checked by cycling the voltage in the range of $-0.2 < V < +0.2$ V 25 times, with the resulting characteristics shown in Figure 6.6. Sweeping the voltage between zero and high positive or negative voltage ($|V| > 1$ V) resets the $SrTiO_3$ into the high resistance state. By sweeping the voltage between −1 and +1 V, the $SrTiO_3$ is maintained in the low resistance state.

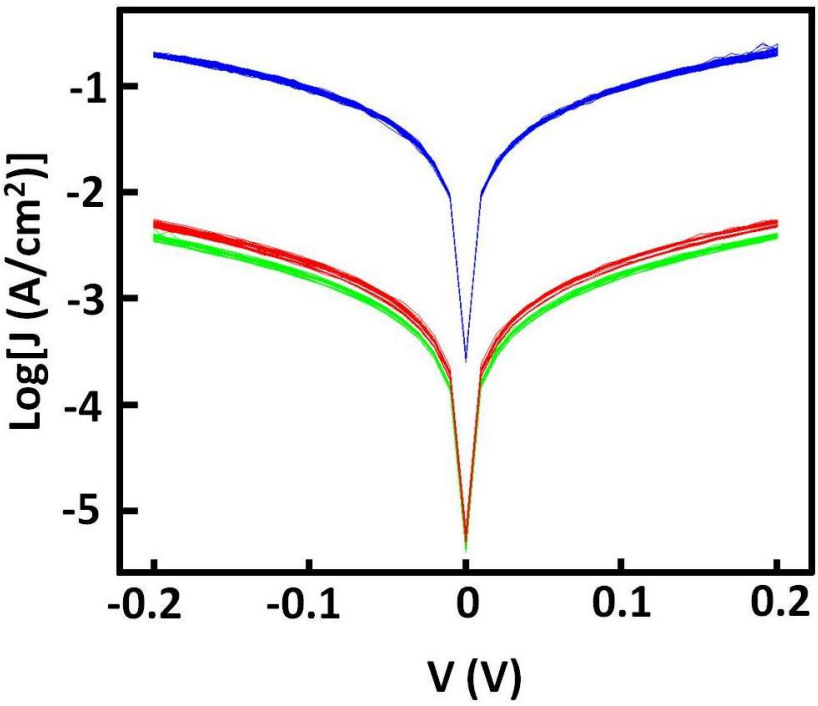

Figure 6.6: Confirmation of the resistive state in each case from Figure 6.5 via variation of the bias in the $-0.2 < V < +0.2$ V range, as described in the text.

6.4 Modelling the antipolar resistive switching

As presented in chapter 3, the conduction through metal oxides can be modelled using the Poole-Frenkel equation. The electrical current originates from electron transport via the conduction band by trapping and detrapping of carriers at localized states, expressed by

$$J_{\mathrm{PF}} = C\bar{E}\exp\left[-e\left(\varphi_{\mathrm{T}} - \sqrt{\frac{e\bar{E}}{\pi\varepsilon}}\right)/kT\right] \tag{6.1}$$

where C is a constant, $\bar{E}$ is the electric field strength, φ_{T} is the location of the trap below the conduction band minimum and ε is the permittivity of the material. Application of Equation 6.1 assumes that the interface is ideal, so that there is efficient injection of electrons from the electrode into the dielectric film.

In several metal oxides, it has been observed that at low electric field there is a small current that increases abruptly to high values by increasing the voltage. The abrupt transition between low and high leakage-current may indicate that the injection of electrons into the bulk is suppressed at low voltages. Hence, the impact of the interface on injection of electrons must be combined with the Poole-Frenkel equation to account for this phenomenon. This has been modelled in chapter 4 where it has been proposed that the conduction mechanisms in $SrTiO_3$ originate from the injection of electrons into the bulk by tunnelling to trap states near the interface,

followed by thermal activation of electrons between the traps inside the dielectric film. The equation for conduction may be summarised by

$$P = P_{\text{injection}} \times P_{\text{excitation}} \tag{6.2}$$

where P is the probability of an electron will pass through the oxide, which is equal to the product of electron injection probability at the interface ($P_{\text{injection}}$) and the probability that an electron will pass through the bulk by thermal excitation via trap bound-states and the conduction band of the insulator ($P_{\text{excitation}}$). At low voltage, P is limited by $P_{\text{injection}}$ due to low electron injection at the interface. At high voltages, $P_{\text{excitation}}$ limits the total current where there is sufficient tunnelling injection of electrons into the dielectric. $P_{\text{excitation}}$ is given by the Poole-Frenkel equation (Equation 6.1), where the exponential term shows the probability of electron thermal activation from the trap states into the conduction band. The thermal excitation of electrons can be increased by lowering the potential barriers between traps, where the term $\sqrt{e\bar{E}/\pi\varepsilon}$ in Equation 6.1 describes the effect of an electric field upon the barriers. $P_{\text{injection}}$ has been modelled in chapter 4 by trap-assisted-tunnelling, where the location of traps relative to the interface have been assumed to be fixed. The electric field increases electron injection by lowering and/or narrowing the barrier between the traps and the interface.

By using Equation 6.2, the current characteristics in $SrTiO_3$ can be accurately modelled (Figure 4.9). However, in order to model the antipolar resistive switching behaviour of $SrTiO_3$, an additional mechanism must be added into Equation 6.2.

First, in a MIM structure, upon application of negative voltage on the top electrode a leakage current occurs by electron injection from the top electrode to the bulk and from the bulk to the bottom electrode (Figure 6.7(a)). When a positive voltage is applied, the injection of electrons would be in the reverse direction from the bottom electrode to the bulk and then to the top electrode (Figure 6.7(b)). As a result, both interfaces must be included independently, and Equation 6.2 is modified to

$$P = P_{\mathrm{BE}} \times P_{\mathrm{excitation}} \times P_{\mathrm{TE}} \tag{6.3}$$

where P_{BE} and $P_{\mathrm{T}E}$ are the probabilities of electron injection at the bottom and top electrodes, respectively.

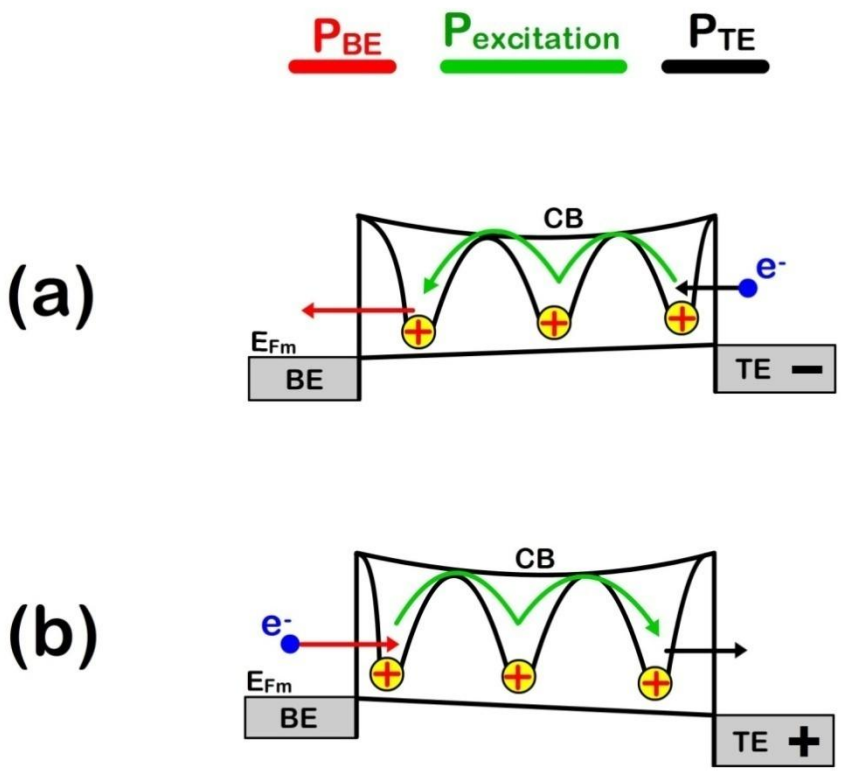

Figure 6.7: The electron injection (a) from an electrode to the bulk and (b) from the bulk to the opposite electrode at different voltage polarities.

Secondly, in resistive switching metal oxides, it is currently understood that there is migration of traps during the application of a bias, changing the spatial distribution of the electron traps. In $SrTiO_3$ the traps probably arise from oxygen vacancies, which act as deep double donors [62, 93]. By changing the polarity of the voltage, the oxygen vacancies migrate nearer to the top or bottom electrode (Figure 6.7). Consequently, the distance between oxygen vacancies and the electrodes can be changed electrically. If this is the case, the electric field alters the tunnelling barrier width at the interfaces, by affecting the distance between traps and the electrodes. Thus, the conventional tunnelling equation needs modification, since they are based upon fixed location of traps [106, 107].

To incorporate the mechanisms involving the charge carriers and mobile deep traps, we have constructed a simple, one-dimensional model, depicted in Figure 6.8, which can be divided into two parts. The first part relates to the carrier injection at both interfaces, and the second part relates to the movement of oxygen vacancies driven by the electric field inside the dielectric film.

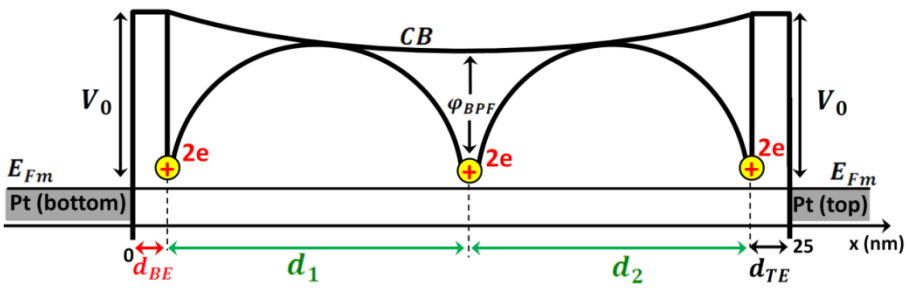

Figure 6.8: A simple model with square barriers between the oxygen vacancies and interfaces.

For tunnelling injection, the simplified approach is to assume a square potential of fixed height, V_0, and width defined by the distance from the interface to the closest deep trap, denoted d_{BE} and d_{TE} corresponding to the bottom and top electrodes, respectively. The resulting tunnelling probability is given by

$$P_{\mathrm{T}}(d) = 16\left(\frac{E}{V_0}\right)\left(1 - \frac{E}{V_0}\right)\exp(-2Kd) \tag{6.4}$$

where E is the electron energy, V_0 is the potential barrier height, d is barrier width, and

$$K = \sqrt{\frac{2m(V_0 - E)}{\hbar^2}} \tag{6.5}$$

where m is the electron effective mass. As a result of the presence of the two, in general non-equivalent junctions, the total $P_{\mathrm{injection}}$ is

$$P_{\mathrm{injection}} = P_{\mathrm{T}}(d_{\mathrm{BE}}) \times P_{\mathrm{T}}(d_{\mathrm{TE}}) \tag{6.6}$$

The barrier widths, d_{BE} and d_{TE}, are modelled by allowing a fixed number of point charges to respond to the applied electric field. Based upon the probable oxidation states of oxygen vacancies, three $+2e$ point charges [108] were allowed to move between the electrodes without any barrier (Figure 6.8). In addition, to confine the movement of charges between electrodes, two fixed small charges of $+2e/100$ were placed at the interfaces. The total distance between the electrodes was taken to be 25 nm, equal to that of the experimental sample thickness.

6.5 Charge movement calculation

In order to find the values of d_{BE} and d_{TE} at different voltage biases, a numerical method is required to calculate the charge movement upon application of a potential difference. Figure 6.9 illustrates three mobile point charges of q_2, q_3 and q_4 (yellow circles) which are confined between two fixed point charges of q_1 and q_5 (blue circles). The equilibrium location of q_2, q_3 and q_4 under an external force of F_{ext}, can be calculated by solving the following four equations in four unknowns of d_{BE}, d_1, d_2 and d_{TE},

$$\frac{q_3 \boldsymbol{q_2}}{(d_1)^2} + \frac{q_4 \boldsymbol{q_2}}{(d_1 + d_2)^2} + \frac{q_5 \boldsymbol{q_2}}{(d_1 + d_2 + d_{TE})^2} = \frac{q_1 \boldsymbol{q_2}}{(d_{BE})^2} + F_{ext} \tag{6.7}$$

$$\frac{q_4 \boldsymbol{q_3}}{(d_2)^2} + \frac{q_5 \boldsymbol{q_3}}{(d_2 + d_{TE})^2} = \frac{q_2 \boldsymbol{q_3}}{(d_1)^2} + \frac{q_1 \boldsymbol{q_3}}{(d_{BE} + d_1)^2} + F_{ext} \tag{6.8}$$

$$\frac{q_5 \boldsymbol{q_4}}{(d_{TE})^2} = \frac{q_3 \boldsymbol{q_4}}{(d_2)^2} + \frac{q_2 \boldsymbol{q_4}}{(d_1 + d_2)^2} + \frac{q_1 \boldsymbol{q_4}}{(d_{BE} + d_1 + d_2)^2} + F_{ext} \tag{6.9}$$

$$d_{BE} + d_1 + d_2 + d_{TE} = 25 \tag{6.10}$$

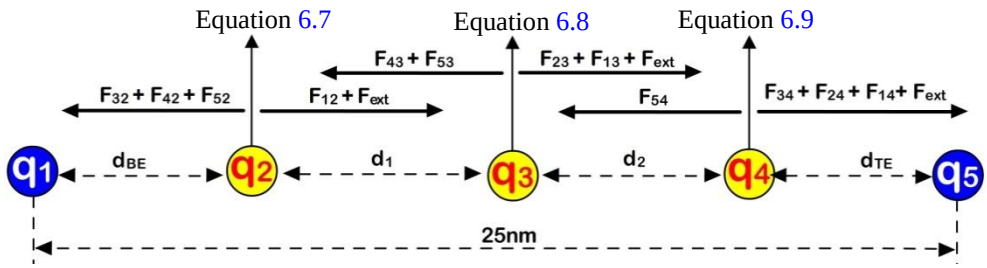

Figure 6.9: Two fixed point charges of q_1 and q_5 which confine three mobile charges of q_2, q_3 and q_4.

However, Equations 6.7, 6.8 and 6.9 are non-linear which means they cannot be solved with the conventional methods that are used for simultaneous linear equations. In order to numerically solve these four equations, three variables of RF_2, RF_3 and RF_4 are introduced which are the resultant forces on q_2, q_3 and q_4 respectively

$$RF_2 = \frac{q_3 q_2}{(d_1)^2} + \frac{q_4 q_2}{(d_1 + d_2)^2} + \frac{q_5 q_2}{(d_1 + d_2 + d_{\mathrm{TE}})^2} - \frac{q_1 q_2}{(d_{\mathrm{BE}})^2} - F_{\mathrm{ext}} \qquad (6.11)$$

$$RF_3 = \frac{q_4 q_3}{(d_2)^2} + \frac{q_5 q_3}{(d_2 + d_{\mathrm{TE}})^2} - \frac{q_2 q_3}{(d_1)^2} - \frac{q_1 q_3}{(d_{\mathrm{BE}} + d_1)^2} - F_{\mathrm{ext}} \qquad (6.12)$$

$$RF_4 = \frac{q_5 q_4}{(d_{\mathrm{TE}})^2} - \frac{q_3 q_4}{(d_2)^2} - \frac{q_2 q_4}{(d_1 + d_2)^2} - \frac{q_1 q_4}{(d_{\mathrm{BE}} + d_1 + d_2)^2} - F_{\mathrm{ext}} \qquad (6.13)$$

Firstly, it is assumed that only q_2 is a mobile charge which can move between q_1 and q_3 by variation of d_{BE} (Figure 6.10(a)). By reducing d_{BE} to zero, q_2 approaches q_1 which results to increase the magnitude of the resultant force (RF_2) to infinity. RF_2 would also increase by the movement of q_2 close to q_3. The minimum of RF_2 occurs between q_1 and q_3 which can be calculated by taking the derivative of RF_2 as follows:

$$\frac{d(RF_2)}{d(d_{\mathrm{BE}})} = 0 \qquad (6.14)$$

From Equation 6.14, d_{BE} is calculated which is the equilibrium location of q_2 when the other point charges are assumed to be fixed. After calculation of d_{BE}, q_3 is assumed to be the only mobile charge (Figure 6.10(b)) and d_1 can be calculated in a similar way to d_{BE} by finding the minimum of RF_3

$$\frac{d(RF_3)}{d(d_1)} = 0 \tag{6.15}$$

By using a similar method the equilibrium location of q_4 can be also calculated when the rest of the charges are fixed (Figure 6.10(c)). After finding the approximate values for $d_{BE,}$ d_1 and d_2, this procedure is repeated which results in new values of d_{BE}, d_1 and d_2. By repeating this procedure the difference between the new and previous values of d_{BE}, d_1 and d_2 approach to zero. As a result, the number of iterations can be limited by setting a condition that the maximum displacement of q_2, q_3 and q_4 from the previous step being smaller than desired accuracy.

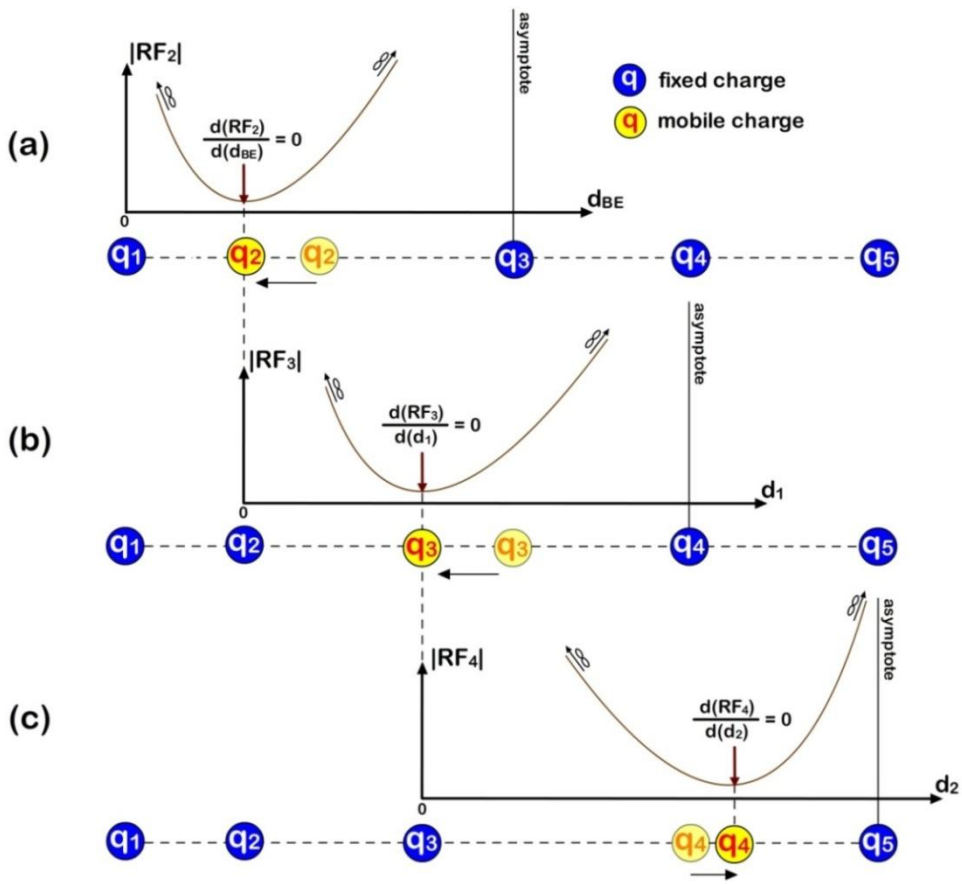

Figure 6.10: The optimum location of mobile point charge of (a) q_2, (b) q_3, and (c) q_4 where the resultant force on the point charge is minimum.

6.6 Antipolar modelling results

Based upon the simulation results, values of d_{BE} and d_{TE}, were obtained, along with the nominal distances between the point charges, d_1 and d_2, by varying the potential difference and calculating the equilibrium locations of positive charges (Figure 6.11). As would be expected, a positive voltage applied to the top electrode (bottom electrode is grounded) results in the oxygen vacancies migrating towards the bottom electrode so that d_{BE} decreases and d_{TE} increases. For a negative voltage polarity, the oxygen vacancies are attracted to the top electrode, and d_{BE} increases while d_{TE} decreases. Using the geometries obtained using this model, the current density can be expressed as

$$J = P_{\mathrm{T}}(d_{\mathrm{BE}}) \times P_{\mathrm{T}}(d_{\mathrm{TE}}) \times J_{\mathrm{PF}} \tag{6.16}$$

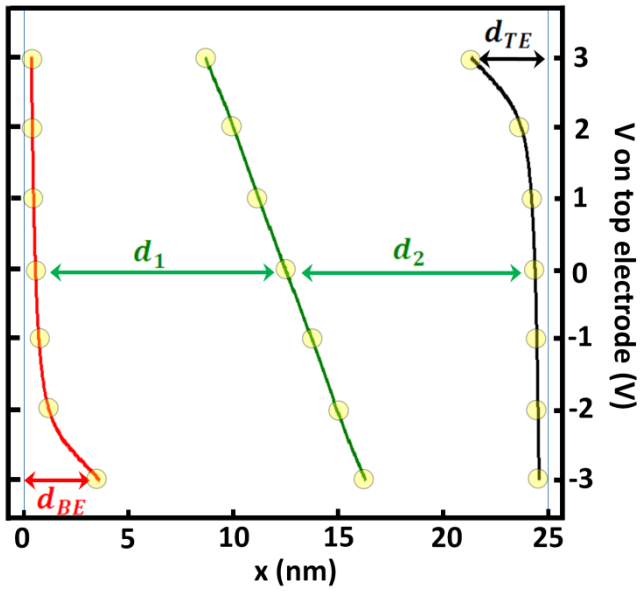

Figure 6.11: Schematic of the location of the deep traps within the oxide film under different voltage biases.

Figure 6.12 depicts the variation of injection current where the applied field results in changing d_{BE} and d_{TE}. The maximum value for $P_{injection}$ occurs at zero bias where d_{BE} and d_{TE} are equal. By increasing the magnitude of voltage, J_{PF} increases while $P_{injection}$ decreases resulting in maxima in current at ± 1 V.

In the above analysis the point charges are free to move in response to the electric field, but in real materials, in addition to the long-range electrostatic force between oxygen vacancies, there are also diffusion barriers. Over short time-scales the existence of diffusion barriers may inhibit the redistribution of the defects, and equilibration may not have sufficient time take place. As a result, the oxygen vacancies can be driven near to one electrode by increasing the bias, but they do not necessarily redistribute uniformly through the film upon removal of the bias.

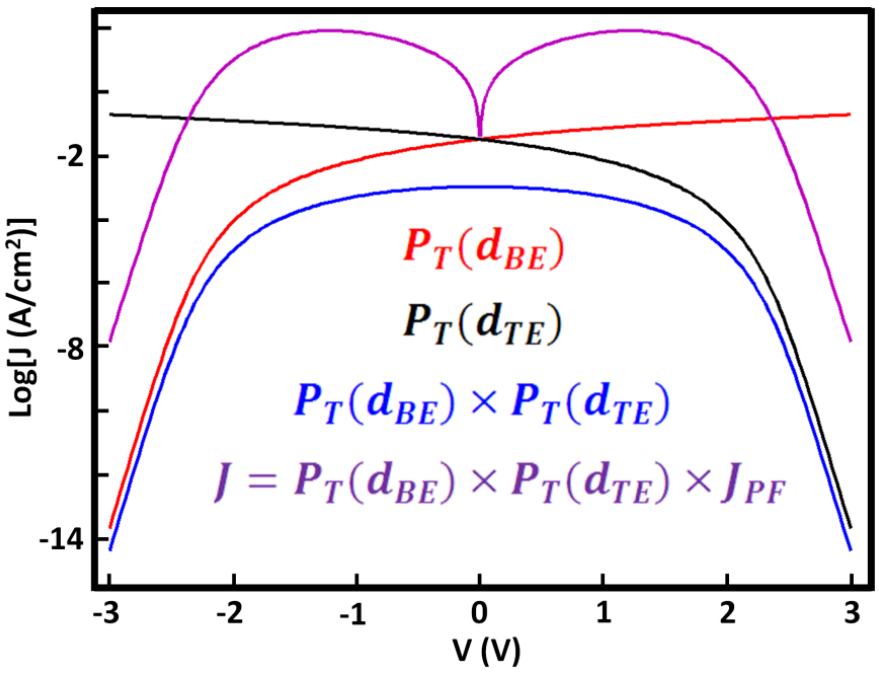

Figure 6.12: The varition of injection current due the movement of oxygen vacancies.

To include the kinetics of migration in a fashion consistent with our observations (Figure 6.4), two threshold values of bias are included. The oxygen vacancy migration towards the opposite electrode occurs when a voltage with opposite polarity is applied with an amplitude of +0.2 V, which is equal to the 'set' voltage. In addition, increasing the voltage moves the oxygen vacancies towards the bottom or top electrodes up to ±2.2 V (Figure 6.13). Above this voltage the oxygen vacancies do not move nearer to the interface and $P_{\text{injection}}$ does not change.

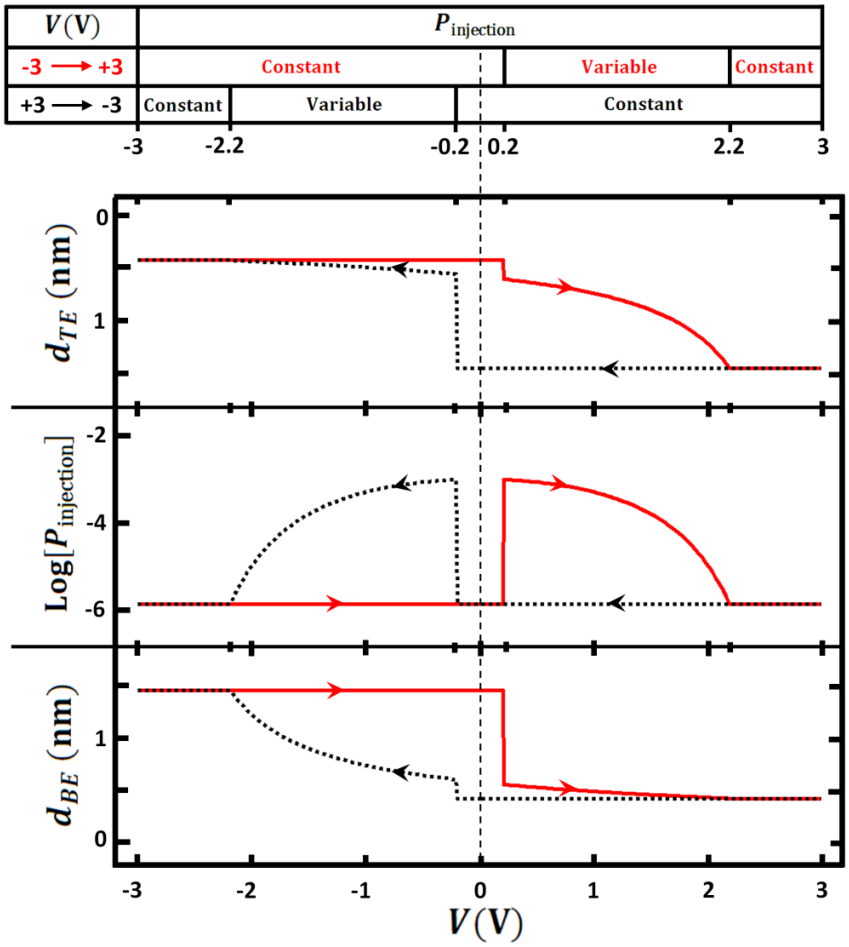

Figure 6.13: Specification of the injection probability, $P_{\text{injection}}$, as a function of the bias magnitude and polarity.

Figure 6.14 shows the simulation results by using the values of Figure 6.13 for $P_{injection}$ assuming $\varphi_T = 0.6$ eV and $V_0 = 1$ eV [109]. Figure 6.15 illustrates the movement of oxygen vacancies through the bulk at different voltage biases. A voltage of −3 V drives the oxygen vacancies close to the top electrode which results in a low concentration of oxygen vacancies at the bottom electrode (point 1). As a result, for $-3 < V < +0.2$ V (point 1 to 2) there is a low leakage current due to the low electron injection at the bottom electrode. By increasing the voltage for positive polarity ($V > +0.2$ V) the oxygen vacancies migrate towards the bottom electrode, leading to a high electron injection at both top and bottom electrode interfaces which results in a high leakage current (low resistance state, point 2 to 3).

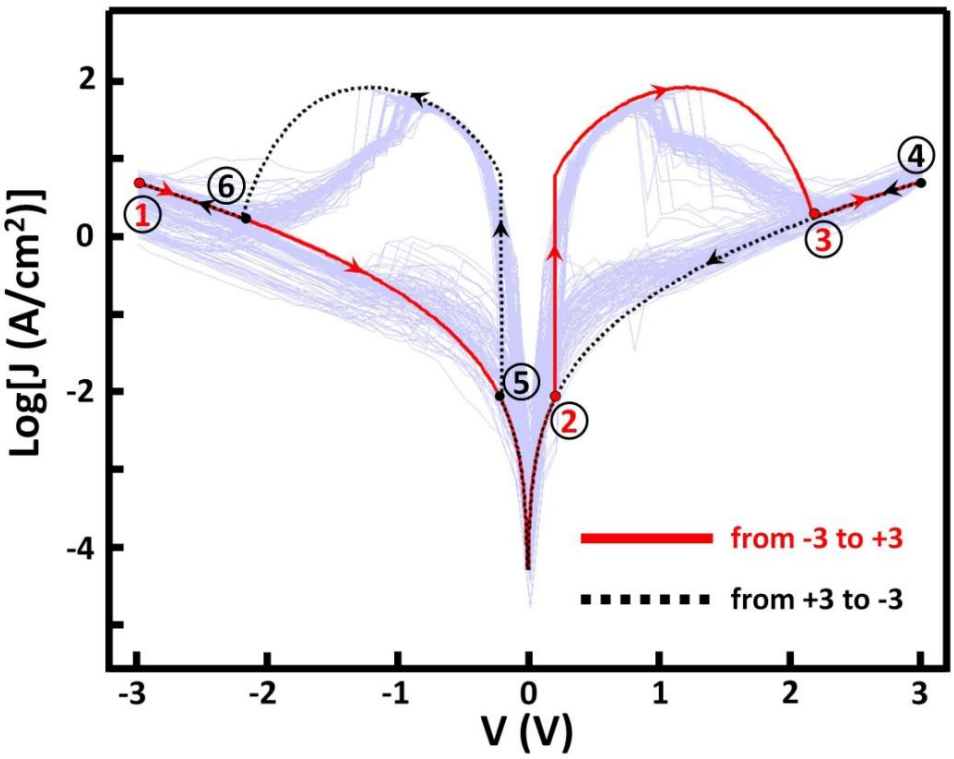

Figure 6.14: The simulation results based on the calculated values of $P_{injection}$.

However, further increasing the voltage in the positive direction drives the oxygen vacancies away from the top electrode interface. In this case, although there is a high electron injection at the bottom electron, the low concentration of oxygen vacancies at the top electrode will reduce the electron injection (point 3 to 4). The device remains in a high resistance state until a negative voltage of $V < -0.2$ V changes the resistance to the low state by driving the oxygen vacancies close the top electrode (point 5 to 6). As a result, application of a high voltage drives the oxygen vacancies away from one electrode, resulting in the high resistance state as a consequence of the low electron injection at this electrode. The low resistance state can be achieved by redistributing the oxygen vacancies through the bulk by reversing the low voltage polarity.

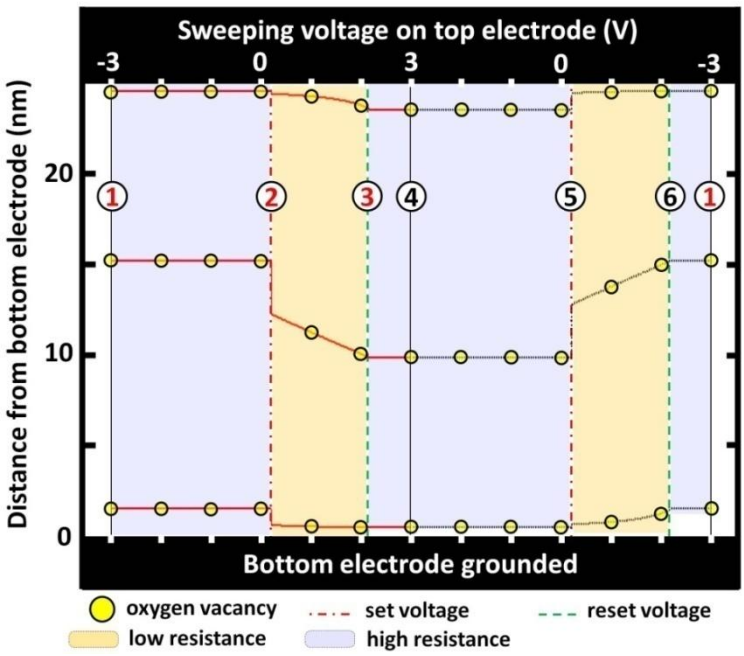

Figure 6.15: Scheme movement of oxygen vacancies through the $SrTiO_3$ at different voltage bias by including the threshold values.

6.7 Schottky and Poole-Frenkel behaviour

The antipolar behaviour presented in this chapter has been modelled based upon a Poole-Frenkel conduction mechanism. However, it should be noted that resistive switching might be due to a Schottky mechanism. Yang *et al* recently showed that the oxygen vacancies in $BiFeO_3$ can accumulate near one electrode by application of different voltage polarities [40]. Sweeping the voltage produced a hysteretic *I–V* characteristic caused by changes in the distribution of oxygen vacancies through the film.

In order to discriminate between Schottky and Poole-Frenkel mechanisms, both hysteresis switching behaviours are illustrated in Figure 6.16. For Schottky devices (Figure 6.16(a)), when a high negative voltage is applied to one electrode, the oxygen vacancies respond electrostatically and move towards this electrode, increasing the n-type carriers near the interface [40]. This would result in an increase in electrons tunnelling into the conduction band due to narrowing of the potential barrier at the Schottky contact. Driving the oxygen vacancies near one electrode also reduces the n-type carriers at the opposite electrode, which in turn yields a wider Schottky barrier at this electrode. Then, the negatively biased electrode is a more Ohmic-like contact while the grounded electrode is a Schottky contact (Figure 6.16(a)).

Therefore, upon application of a small, positive voltage, there would be low electron injection from the grounded electrode into the film due to the Schottky

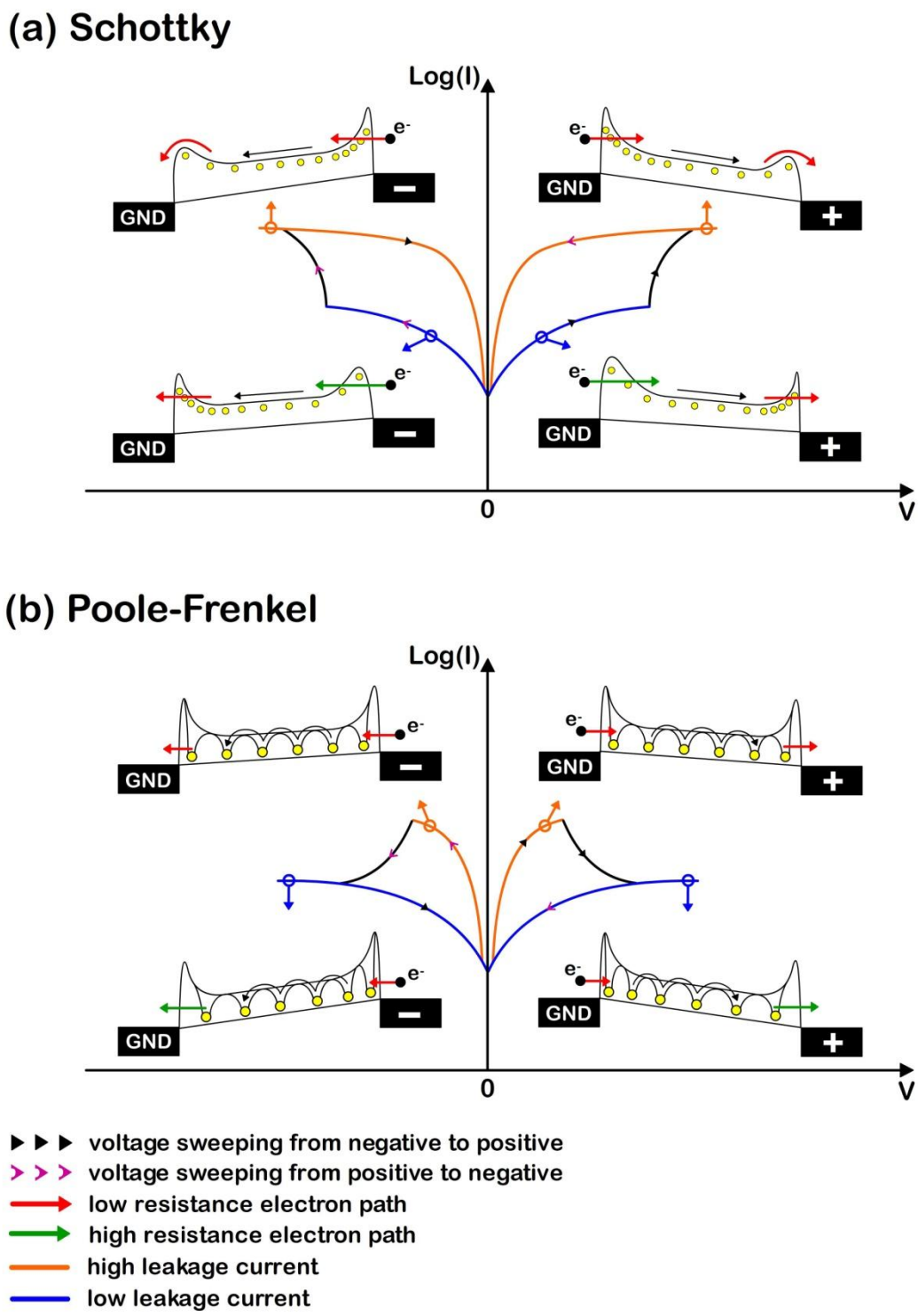

Figure 6.16: The resistive switching behaviour of metal oxides when oxygen vacancies act as the (a) mobile donors and (b) mobile traps.

contact, resulting in a low leakage current. By increasing the voltage in the positive direction, the oxygen vacancies move towards the grounded electrode and transform the contact from Schottky to Ohmic-like which increases the leakage current up to the point that the injection at the biased electrode becomes the limiting factor. Therefore, in Schottky devices, the oxygen vacancies act as the mobile donors [40], where the leakage current through the film is dominated by movement of electrons through the conduction band and not via hopping between defect states.

In contrast, in the case of Poole-Frenkel conduction (Figure 6.16(b)), the oxygen vacancies act as the traps where the leakage current occurs by electrons tunnelling from one electrode to the trap states near the interface, followed by trap and detrapping between the trap states through the bulk by thermionic emission, and tunnelling from the trap states to the opposite electrode.

As a result, in Schottky devices a high voltage bias increases the leakage current by increasing the injection of electrons from electrode to the bulk, but it reduces the leakage current in Poole-Frenkel devices by reducing the injection of electrons from the bulk to the electrode. Hence, although Schottky devices have similar hysteresis switching curves to Poole-Frenkel devices, the sense of operation with bias is reversed, allowing the mechanisms to be distinguished.

6.8 Origin of the antipolar resistive switching

A remaining question exists regarding the origin of antipolar resistive switching in $SrTiO_3$. In metal oxides, formation of oxygen vacancies at the interface is highly likely during the fabrication process, which could result in a high rate of carrier injection into the dielectric. Nevertheless, in several metal oxides, the *I–V* characteristics indicate that the injection is suppressed at the interface. This might imply a mechanism that reduces the concentration of oxygen vacancies at the interface. Understanding this mechanism plays a key role in antipolar resistive switching where a lack of oxygen vacancies at the interface is required to limit $P_{\text{injection}}$ and make it sensitive to the movement of oxygen vacancies relative to both interfaces.

In order to explain the underpinning mechanism of antipolar resistive switching, effect of carbon at the interface is considered. Carbon contamination at the $SrTiO_3$/Pt interface has been observed in XPS depth profile (section 5.3.4) where there was resistive switching under positive voltage. The existence of carbon contamination has been also reported in HfO_2 at both top and bottom electrode interfaces [62].

The role of contamination by carbon in terms of the device leakage current can be understood by examination of Equation 6.2. Here the leakage current is initiated by the injection of carriers into oxygen vacancies geometrically near the interface by tunnelling through an interface barrier. A high rate of carrier injection may occur if oxygen vacancies lie near to the interface. The carbon contamination at the interface

might modify the diffusion barriers of oxygen vacancies near the electrodes where the migration of oxygen vacancies can occur near the top and bottom interfaces (red arrows in Figure 6.17(a)). Depending on the location of oxygen vacancies relative to the electrodes, the injection rate can change between high and low values. Therefore, the MIM structure can be divided into three areas: bulk with a high concentration of oxygen vacancies (yellow area in Figure 6.17(b)), and two resistive interfaces where the conduction can increase by migration of oxygen vacancies close to the electrodes (blue area in Figure 6.17(b)). Based upon this assumption, the high and low resistance states of the MIM structure originate from resistive switching at the top and bottom electrode interfaces (Figure 6.17(a)).

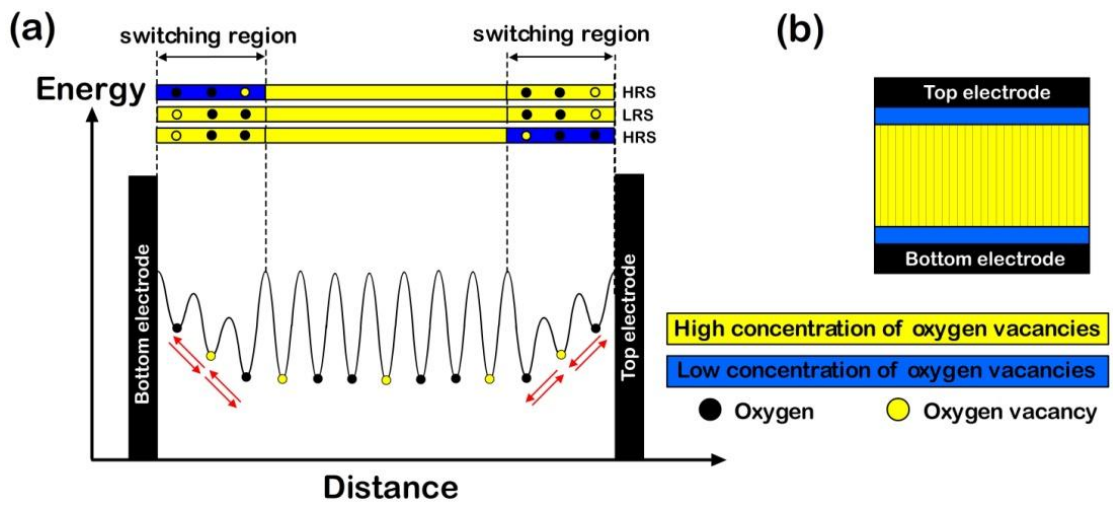

Figure 6.17: (a) Migration of oxygen vacancies near the top and bottom electrode interfaces. (b) Low concentration of oxygen vacancies near the electrodes which might be originated from the carbon contamination at the interfaces.

The migration of oxygen vacancies only in the vicinity of the top and bottom electrode interfaces could also account for the low set voltage of ±0.2 V relative to high reset voltage of ±1 V. In order to explain it, the three regions of MIM structure (Figure 6.17(b)) are modelled as follows. The top and bottom electrodes are modelled by two memristors, M_{TE} and M_{BE} (Figure 6.18). Their resistance can switch between two values of high and low resistance states. When the oxygen vacancies are located near the electrode, the resistance of that interface is low, and it is high when the oxygen vacancies are located away from the electrode. The difference between high and low resistance states is greater than two decades which can be realised from the high and low leakage current values at 0.5 V (Figure 6.18(e)). R_{Bulk} represents bulk resistance which is almost constant and independent of voltage bias. The total resistance of the MIM structure can be presented by

$$R_T = M_{BE} + R_{Bulk} + M_{TE} \tag{6.17}$$

In order to explain the resistive switching behaviour illustrated in Figure 6.19(e), it is assumed that M_{BE} is in a high resistance state (M_{BE}(high)) while M_{TE} is in a low resistance state (M_{TE}(low)). When a voltage bias is applied (Figure 6.19(a)), the

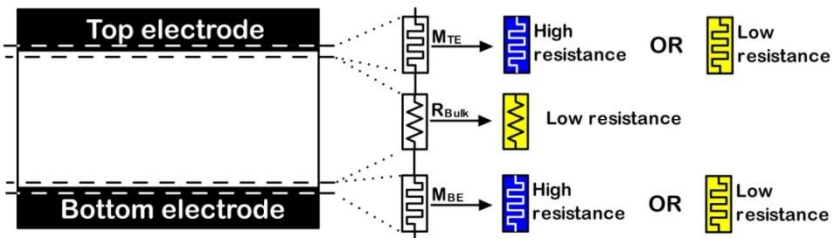

Figure 6.18: Modelling the MIM structure by two memristors of M_{BE} and M_{TE} (representing two interfaces) and R_{Bulk} which represents bulk resistance.

voltage would drop across the M_{BE} (high) as its resistance is much greater than R_{Bulk} + M_{TE}(low). By increasing the voltage above +0.2 V, the resistance of M_{BE} is changed to 'low' by migration of oxygen vacancies close to the bottom electrode (Figure 6.19(b)). Now the voltage bias is divided between the three elements of M_{BE} (low), R_{Bulk} and M_{TE} (low) where the voltage across M_{TE} is smaller than +0.2 V which is not sufficient to switch M_{TE} to the high resistance state. M_{TE} remains in the low resistance state until the voltage increases more than +1 V. Then, the potential difference across the top electrode interface is enough to repel the oxygen vacancies from the top electrode, resulting in a switch of M_{TE} to the high resistance state (Figure 6.19(c)). When the switching occurs, most of the voltage would be dropped across M_{TE} (high) due to its high resistance relative to M_{BE} (low) + R_{Bulk}. Therefore, as the voltage decreases to less than −0.2 V, the potential difference across the M_{TE} is sufficient to repel the oxygen vacancies near the top electrode and switch the M_{TE} back to the low resistance state (Figure 6.19(d)).

This kind of resistive switching cannot be explained by the assumption of continuous migration of oxygen vacancies through the bulk. In continuous migration of oxygen vacancies from one electrode to the opposite electrode, when the migration is initiated by increasing the magnitude of voltage $|V| > 0.2$, the migration will continue until it is prevented by accumulation of oxygen vacancies at the opposite electrode. As a result, the device does not maintain its low resistance state at $0.2 < |V| < 1$.

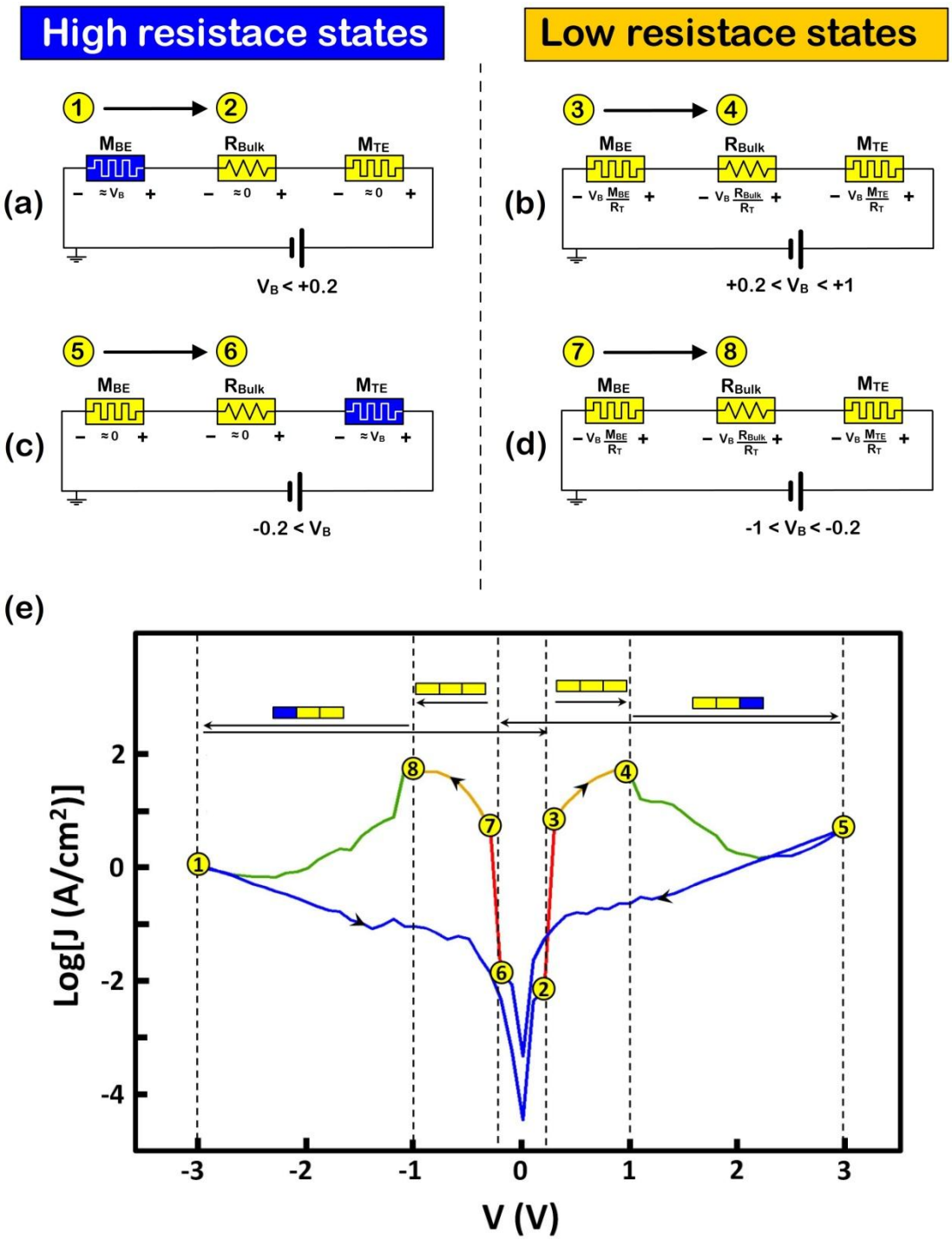

Figure 6.19: (a-d) Schematic of different states of MIM structure which depend on the resistance states of top and bottom electrodes. (e) The antipolar resistive switching of MIM structure originating from migration of oxygen vacancies in vicinity of the top and bottom electrode interfaces.

6.9 Three-state RRAM

The peculiar antipolar resistive switching behaviour might give rise to some novel applications in electronic devices. From the RRAM application view point, antipolar resistive switching exhibits three stable states. In conventional bipolar and unipolar resistive switching RRAM, data can be stored by applying different voltages to the MIM structure which result in reversible switching between low resistance state (representing digital '1') and high resistance state (representing digital '0'). In antipolar resistive switching, when both interfaces are in their low resistance state, there is a high leakage current through the bulk which can be defined as digital '1' (Figure 6.20(a)). However, the high resistance state includes two distinct states that originate from the polarity of the 'reset' voltage.

A positive 'reset' voltage drives the oxygen vacancies away from the top electrode which reduce the leakage current by decreasing the injection current at this interface (Figure 6.20(b)). By contrast, a negative 'reset' voltage drives oxygen vacancies away from the bottom electrode which results in the same low resistance state, but by reducing the injection of electrons at bottom interface (Figure 6.20(c)).

These two different high resistance states can be distinguished from each other by application of a 'set' voltage which can be either positive or negative. For instance, if the device has been reset to its high resistance state by a positive voltage, then application of a positive 'set' voltage does not switch the device to low resistance state. And if the device has been reset to its high resistance state by negative voltage,

then application of a positive 'set' voltage switches the device to the low resistance state. In other words, the device memorises the polarity of 'reset' voltage and antipolar resistive switching can be used as a device with three states of: (i) a low resistance; (ii) a positive high resistance (when $V > +V_{reset}$ has been used to 'reset' the device) and (iii) a negative high resistance state (when $V < -V_{reset}$ has been used to 'reset' the device).

It should be noted that in a three-state antipolar RRAM, detecting the state of the device is destructive to either the positive or negative high resistance state, which depends on the polarity of 'set' voltage. If a positive 'set' voltage is used to detect the device state, then the negative high resistance state must again be constructed after detection. And, for the negative 'set' voltage, the detection of positive high resistance state would be destructive.

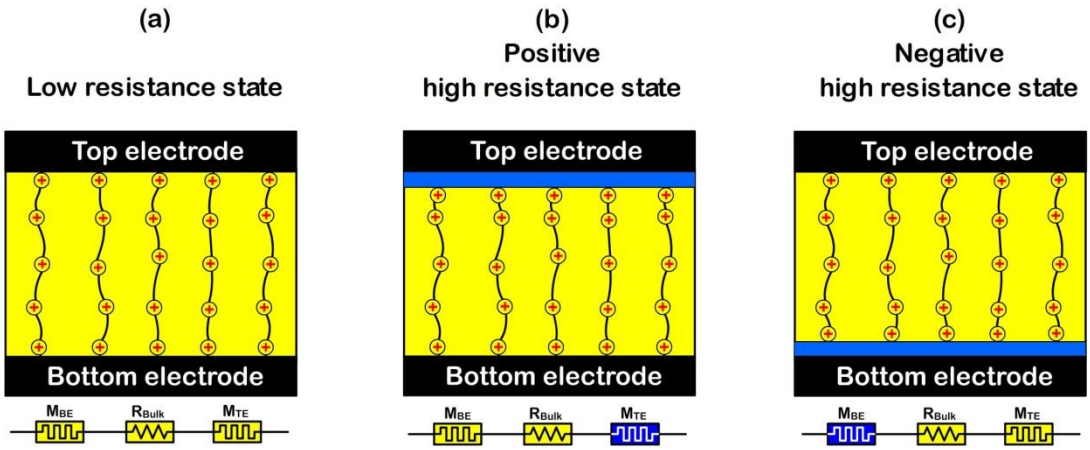

Figure 6.20: Three stable states of RRAM: (a) low resistance state, (b) positive high resistance state, and (c) negative high resistance state.

6.10 Conclusions

The resistive switching of $SrTiO_3$ presented in this chapter depends on both the amplitude and polarity of the applied voltage, and cannot be described as either bipolar or unipolar resistive switching. This behaviour has been termed antipolar resistive switching due to the opposite polarity of the 'set' voltage relative to the previous 'reset' voltage. In order to explain the antipolar behaviour, the conduction mechanism proposed in chapter 4 has been extended by considering the effect of both interfaces on the injection of electrons.

The conduction mechanism has been quantified by use of a simple mathematical equation where the barriers between the oxygen vacancies near the interfaces were assumed to be rectangular. The widths of barriers were changed by movement of oxygen vacancies upon application of a potential difference. The results of simulations have demonstrated an agreement with *J*–*V* characteristics observed experimentally, which show the sensitivity of leakage current to the location of oxygen vacancies relative to the electrodes.

In order to explain the magnitude of 'set' and 'reset' voltage, it has been hypothesised that switching only occurs by migration of oxygen vacancies in the vicinity of the top and bottom interfaces. This might have originated from the existence of carbon contamination at the interfaces which modifies the diffusion barrier of oxygen vacancies, leading to their migration only near the electrodes.

Chapter 7

Summary

> '*Science is a way to teach how something gets to be known; what is not known; to what extent things are known; how to handle doubt and uncertainty; what the rules of evidence are; how to think about things so that judgments can be made; how to distinguish truth from fraud and from show*'
>
> *Richard Feynman*

In this study, the conduction mechanisms of $SrTiO_3$ MIM structures have been investigated to elucidate underpinning mechanisms of the leakage current and the resistive switching behaviour observed in *J-V* characteristics. In chapter 4, modelling of the leakage current was carried out by mathematically match the experimental data by the conventional conduction equations presented in Chapter 3. The abrupt transition from low to high leakage current shown in Figure 4.3 can be described by tunnelling mechanisms (Figure 7.1(a)). However, this transition showed temperature dependence, which is physically inconsistent with the tunnelling equation. This counterintuitive behaviour of the leakage current reveals that it is controlled by both the interface and the bulk, and it is necessary to consider the impact of both in one

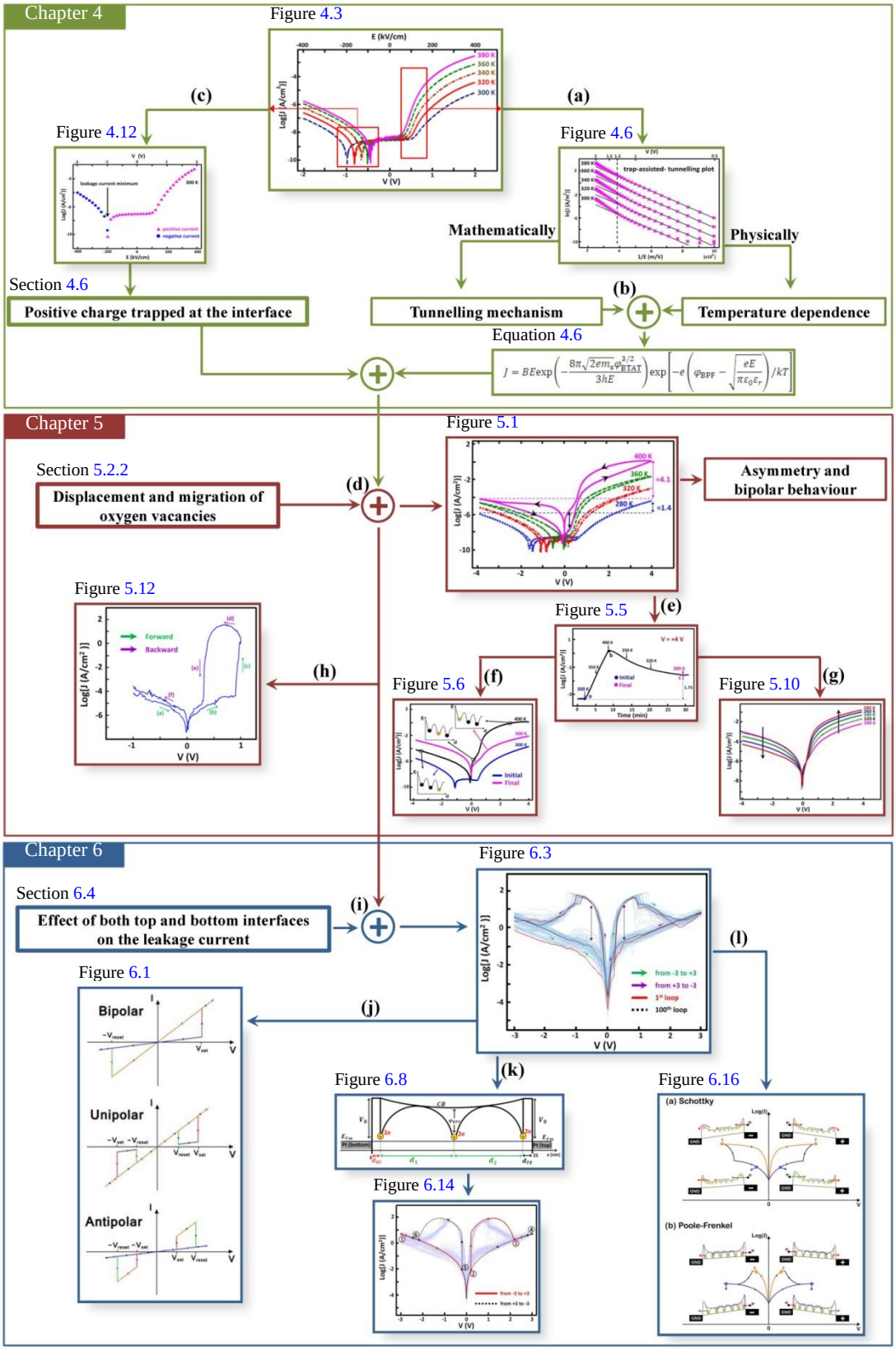

Figure 7.1: Summary of the study on leakage current and resistive switching mechanisms of $SrTiO_3$.

equation to precisely model leakage current (Figure 7.1(b)). A model has been proposed that combines both Poole-Frenkel and trap-assisted-tunnelling mechanisms in one equation. Equation 4.6 is capable of modelling the experimental data accurately. Based upon this model, the leakage current originates from the injection of electrons into the oxygen vacancies near the interface, followed by the thermionic field emission of electrons between the oxygen vacancies.

In addition, the hypothesis of trapped positive charge has been proposed to explain the observation of negative current (Figure 7.1(c)). The positive charge gives rise to an internal electric field at the interface, which combines with the applied field. At low negative bias, the internal electric field is greater than the applied electric field. As a result, the current is in the direction opposite to that which would be generated by the applied field alone.

In chapter 5, the displacement and migration of oxygen vacancies were included in the proposed conduction mechanism (Figure 7.1(d)) to explain both the asymmetry and the bipolar behaviour of the leakage current. The positively charged oxygen vacancies are electrostatically repelled by fixed positive charges at the interface. At equilibrium the oxygen vacancies are located far away from the bottom electrode, which limits the injection of electrons into the bulk by tunnelling. Therefore, the leakage current is highly sensitive to the proximity of oxygen vacancies to the bottom electrode. The application of voltage results in variation in the injection rates of electrons at the interface by changing the distance between the

oxygen vacancies and the electrode. At low temperatures, the oxygen vacancies cannot easily surmount diffusion barriers. The application of voltage only displaces the oxygen vacancies with respect to the bottom electrode, which leads to asymmetric *J*–*V* characteristics. At high temperatures, however, a voltage bias causes the migration of oxygen vacancies near or away from the bottom electrode. This results in greater asymmetry as well as the bipolar resistive switching behaviour of *J*–*V* characteristics (Figure 5.1).

The existence of a fixed positive charge at the bottom electrode interface become more evident in an experiment in which temperature was increased from 300 K to 400 K and then back to 300 K with the DC voltage fixed at +4 V (Figure 7.1(e)). After this experiment, the oxygen vacancies were located near to the interface, which resulted in symmetrical *J*–*V* characteristic at room temperature (Figure 7.1(f)). By increasing the temperature, the leakage current under negative bias decreased due to the migration of oxygen vacancies away from the electrode (Figure 7.1(g)).

Resistive switching has been also observed in a PLD $SrTiO_3$ MIM structure (Figure 7.1(h)). Here the resistive switching between high and low resistance only exists under positive voltage. The existence of fixed positive charge at the interface and the migration of oxygen vacancies in the vicinity of the interface are two key assumptions that make it possible to explain the hysteresis curve under positive voltage. With high voltage bias, the oxygen vacancies are driven close to the interface. However, by reducing the voltage, the repulsive force between the oxygen

vacancies and the fixed positive charge trapped at the interface causes the migration of oxygen vacancies away from the electrode. Variation in the distance between the oxygen vacancies and the electrode affects the injection rates of electrons at the interface, which then results in a dramatic change in the leakage current.

Finally, in chapter 6 resistive switching behaviour was observed in $SrTiO_3$, where switching depends on both the amplitude and polarity of the applied voltage as shown in Figure 6.3. This is termed antipolar behaviour, a concept introduced as a third category of resistive switching as opposed to bipolar and unipolar switching (Figure 7.1(j)). In order to explain antipolar behaviour, the conduction mechanism proposed in chapter 4 has been used to consider the effect of the interfaces on the leakage current (Figure 7.1(i)). The migration of oxygen vacancies in the vicinity of both interfaces affect the injection of electrons from an electrode to the bulk and from the bulk to the opposite electrode, which results in antipolar resistive switching behaviour. The conduction mechanism has been quantified by use of a simple mathematical equation (Figure 7.1(k)). The results of simulations have demonstrated an agreement with *J*–*V* characteristics observed experimentally. In addition, it has shown that a similar hysteresis curve is produced with the switching is in a reverse direction when the electron injection from electrode to the bulk is controlled by Schottky emission (Figure 7.1(l)).

Appendix A

Resistive switching periodic table

Table A.1: Elements that have been used as electrodes (blue), and those whose oxides have demonstrated bipolar (red) and unipolar (yellow) resistive switching behaviour.

Bipolar
Unipolar
Electrode

1 He														
3 Li	4 Be											5 B	6 C	7 N
11 Na	12 Mg											13 Al	14 Si	15 P
19 K	20 Ca	21 Sc	22 Ti	23 V	24 Cr	25 Mn	26 Fe	27 Co	28 Ni	29 Cu	30 Zn	31 Ga	32 Ge	33 As
37 Rb	38 Sr	39 Y	40 Zr	41 Nb	42 Mo	43 Tc	44 Ru	45 Rh	46 Pd	47 Ag	48 Cd	49 In	50 Sn	51 Sb
55 Cs	56 Ba	57-71	72 Hf	73 Ta	74 W	75 Re	76 Os	77 Ir	78 Pt	79 Au	80 Hg	81 Tl	82 Pb	83 Bi

57 La	58 Ce	59 Pr	60 Nd	61 Pm	62 Sm	63 Eu	64 Gd	65 Tb	66 Dy	67 Ho	68 Er	69 Tm	70 Yb	71 Lu

Table A.2: Bipolar and unipolar resistive switching behaviour in different oxides.

Atomic Number	Element	Oxide	Fabrication Method	Electrodes		RS		Reference	Year
				Top Electrode	Bottom Electrode	Bipolar Behaviour	Unipolar Behaviour		
6	C	DLC	PLD	Pt/Ti	Pt	✲		[24]	2012
		GO	Spin coating	Al	ITO	✲		[26]	2010
		a-C	Ion beam	Cu	Pt	✲		[25]	2010
11	Na	$SmCaMnO_3$	PLD	Ti	LSMO	✲		[110]	2006
12	Mg	MgO	Sputtering	Pt	Pt		✲	[111]	2012
13	Al	AlO_x	ALD	Pt	TiN	✲		[112]	2011
14	Si	SiO_x	Sputtering	ITO	Cr/Au	✲		[27]	2012
20	Ca	$PrCaMnO_3$	Sputtering	Au/Ta	Pt	✲		[113]	2012
		$PrCaMnO_3$	Sputtering	GST/Ti	Pt/TiN	✲		[114]	2011
		$PrCaMnO_3$	PLD	Au/Ti	SRO	✲		[115]	2009
		$PrCaMnO_3$	Sputtering	Pt	Pt	✲		[116]	2009
		$PrCaMnO_3$	PLD	Ag	Pt/Ti	✲		[117]	2008
22	Ti	TiO_2	PLD	Pt	Pt/Ti	✲		[118]	2011
		TiO_x	Sputtering	Pt	Pt	✲		[119]	2009
		TiO_2	Single crystals	Pt	Pt	✲		[120]	2008
		TiO_2	ALD	Pt	Pt	✲		[38]	2008
		TiO_2	Sputtering	Pt	Pt/Ti	✲		[121]	2007
		TiO_2	ALD	Pt	Pt	✲	✲	[122]	2010
		TiO_2	ALD	Pt	Pt		✲	[123]	2011
		TiO_2	ALD	Pt	Pt		✲	[66]	2010
		TiO_2	E-beam	Pt	Pt/Ti		✲	[124]	2008
		TiO_2	ALD	Pt	Pt		✲	[97]	2007
		TiO_2	ALD	Pt	Pt		✲	[125]	2007
		TiO_2	ALD	Pt, Al	Ru		✲	[65]	2005
23	V	VO	Sputtering	Al	ITO	✲		[126]	2012
24	Cr	Cr_2O_3	Sputtering	Pt	TiN	✲		[127]	2010
25	Mn	$DyMn_2O_5$	Sputtering	Pt	TiN	✲		[128]	2011
26	Fe	SiO_2/FeO_x	Sputtering	Fe	TiN	✲		[129]	2010
27	Co	CoO_x	Sputtering	Pt	Pt		✲	[130]	2010
28	Ni	NiO	Sputtering	Ni	Ni/TiN	✲	✲	[131]	2010
		NiO	Sputtering	Pt, Ti	Pt		✲	[132]	2012

		NiO	ALD	Pt	W		✡	[133]	2011
		NiO:Ti	Sputtering	Pt	Pt		✡	[134]	2010
		NiO	Sputtering	Pt	Pt/Ti		✡	[135]	2010
		NiO	Thermal	Pt	Pt		✡	[96]	2008
		NiO_x	Sputtering	Pt	Pt		✡	[136]	2007
		NiO	Sputtering	Pt	Pt/Ti		✡	[137]	2005
29	Cu	CuO_x	Thermal	Mo	Pt/Ti	✡		[138]	2007
30	Zn	ZnO	Sputtering	Cr	Al, Zn	✡		[98]	2011
		ZnO	Sputtering	Au	Steel	✡	✡	[139]	2009
		ZnO	Sputtering	Pt	Pt		✡	[140]	2012
31	Ga	GaO_x	PLD	Pt	ITO	✡		[141]	2010
32	Ge	GeO_2	PVD	Ni	TaN	✡		[28]	2012
38	Sr	$SrTiO_3$:Fe	PLD	Pt	STO:Nb	✡		[48]	2012
		$SrTiO_3$:Nb	Single crystals	Au	Au	✡		[142]	2012
		$SrTiO_3$:Nb	Single crystals	Pt	In	✡		[85]	2011
		$SrTiO_3$	PLD	Au	Pt/Ti	✡		[143]	2010
		$SrTiO_3$:Nb	Single crystals	Pt	Al	✡		[144]	2010
		$SrTiO_3$:Nb	Single crystals	Pt	Pt	✡		[145]	2010
		$SrTiO_3$:Nb	Single crystals	Pt	Au/Ti	✡		[146]	2009
		$SrTiO_3$:La	Ceramics	Pd	Pd	✡		[50]	2008
		$SrTiO_3$:Nb	Single crystals	RuO_x	Pt	✡		[147]	2008
		$BaSrTiO_3$:Mn	PLD	W	$SrRuO_3$	✡		[148]	2008
		$SrTiO_3$:Nb	Single crystals	Pt	Pt	✡		[74]	2007
		$SrRuO_3$	PLD	Au	STO:Nb	✡		[86]	2007
		$BaSrTiO_3$	PLD	Pt	$SrRuO_3$	✡		[149]	2006
		$SrZrO_3$:Cr	PLD	Au	$SrRuO_3$	✡		[31]	2000
		$BaSrTiO_3$:Mn	PLD	Pt	Pt/Ti	✡	✡	[150]	2010
		$SrZrO_3$:V	Sputtering	Al	Pt/Ti	✡	✡	[151]	2007
		$SrTiO_3$	PLD	Pt	Pt/Ti		✡	[51]	2011
39	Y	Y_2O_3	Sputtering	Al	Al		✡	[152]	2011
40	Zr	ZrO_2	Sputtering	Pt/Ti	Pt/Ti	✡	✡	[153]	2012
41	Nb	NbO_x	PLD	Pt	Pt	✡		[154]	2011
		NbO_x	PLD	Pt	Pt		✡	[155]	2010
42	Mo	MoO_x/GdO_x	Sputtering	Pt	Pt/Ti	✡		[156]	2009
		MoO_x:Cu	Sputtering	Pt	Cu	✡		[157]	2007
49	In	In_2O_3	Thermal	Al	ITO	✡		[158]	2011
50	Sn	SnO_2	PLD	Pt	Pt		✡	[159]	2009
51	Sb	Sb_2O_5	Sputtering	Pt	Pt		✡	[160]	2012
56	Ba	$BaSrTiO_3$:Mn	PLD	W	$SrRuO_3$	✡		[148]	2008
		$BaSrTiO_3$	PLD	Pt	$SrRuO_3$	✡		[149]	2006
		$BaSrTiO_3$:Mn	PLD	Pt	Pt/Ti	✡	✡	[150]	2010

57	La	$LaAlO_3$	PLD	YBCO	STO:Nb	✡		[161]	2011
58	Ce	CeO	Sputtering	Ru	TaN	✡		[162]	2012
59	Pr	PrO	Sputtering	Ru	TaN	✡		[162]	2012
		$PrCaMnO_3$	Sputtering	Au/Ta	Pt	✡		[113]	2012
		$PrCaMnO_3$	Sputtering	GST/Ti	Pt/TiN	✡		[114]	2011
		$PrCaMnO_3$	PLD	Au/Ti	SRO	✡		[115]	2009
		$PrCaMnO_3$	Sputtering	Pt	Pt	✡		[116]	2009
		$PrCaMnO_3$	PLD	Ag	Pt/Ti	✡		[117]	2008
60	Nd	Nd_2O_3	Sputtering	Ru	TaN		✡	[163]	2011
62	Sm	SmO	Sputtering	Ru	TaN	✡		[162]	2012
63	Eu	EuO	Sputtering	Ru	TaN	✡		[162]	2012
64	Gd	MoO_x/GdO_x	Sputtering	Pt	Pt/Ti	✡		[156]	2009
66	Dy	$DyMn_2O_5$	Sputtering	Pt	TiN	✡		[128]	2011
		Dy_2O_3	Sputtering	Ru	TaN		✡	[163]	2011
68	Er	Er_2O_3	Sputtering	Ru	TaN		✡	[163]	2011
71	Lu	Lu_2O_3	PLD	Pt	Pt		✡	[164]	2010
72	Hf	HfO_2	ALD	Pt/Ti	Pt/Ti	✡		[165]	2012
		HfO_2	Sputtering	TiN	Pt/Ti	✡		[166]	2012
		HfO_2	ALD	TiN/Ti	TiN	✡		[167]	2010
		HfO_2	PLD	Cr/Au	Pt/Ti	✡		[168]	2008
		HfO_2	MOCVD	Au	Pt/Ti	✡	✡	[169]	2008
		HfO_2	ALD	TiN	Ni		✡	[170]	2012
		HfO_2	ALD	TiN	TiN		✡	[171]	2012
		HfO_2	ALD	Au	Pt		✡	[172]	2011
		HfO_2	AVD	Au	TiN		✡	[173]	2010
		HfO_2	ALD	Pt	TiN		✡	[174]	2010
		HfO_2	Sputtering	Pt	Pt/Ti		✡	[175]	2008
		HfO_x	ALD	Ru	TiN		✡	[176]	2008
73	Ta	Ta_2O_5	PVD	Pt	Pt	✡		[177]	2012
		TaO_x	Sputtering	Pd	Pd	✡		[178]	2012
		Ta_2O_5	Sputtering	Pt	Pt	✡		[179]	2011
		Ta_2O_5	Sputtering	Pt	Pt	✡		[39]	2010
74	W	WO_x	Thermal	Pt	W	✡		[180]	2011
83	Bi	$BiFeO_3$:Nb	PLD	Pt	Pt/Ti	✡		[181]	2012

References

[1] G. E. Moore, "Cramming more components onto integrated circuits," *Electronics,* vol. 38, 1965.

[2] C. Choi, "Modeling of nanoscale MOSFETS," Electrical Engineering, Stanford University, 2002.

[3] A. Touhami and A. Bouhdada, "Modeling of gate-induced drain leakage current in n-type metal-oxide-semiconductor field effect transistor," *Journal of Applied Physics,* vol. 89, pp. 1880-1884, 2001.

[4] T. Yuan, D. A. Buchanan, C. Wei, D. J. Frank, K. E. Ismail, L. Shih-Hsien, *et al.*, "CMOS scaling into the nanometer regime," *Proceedings of the IEEE,* vol. 85, pp. 486-504, 1997.

[5] A. I. Kingon, J.-P. Maria, and S. K. Streiffer, "Alternative dielectrics to silicon dioxide for memory and logic devices," *Nature,* vol. 406, 2000.

[6] E. P. Gusev, E. Cartier, D. A. Buchanan, M. Gribelyuk, M. Copel, H. Okorn-Schmidt, *et al.*, "Ultrathin high-K metal oxides on silicon: processing, characterization and integration issues," *Microelectronic Engineering,* vol. 59, pp. 341-349, 2001.

[7] G. Ribes, J. Mitard, M. Denais, S. Bruyere, F. Monsieur, C. Parthasarathy, *et al.*, "Review on high-k dielectrics reliability issues," *IEEE Transactions on Device and Materials Reliability,* vol. 5, 2005.

[8] L. J. Brillson and Y. Lu, "ZnO Schottky barriers and Ohmic contacts," *Journal of Applied Physics,* vol. 109, pp. 121301-33, 2011.

[9] D. Niu, R. W. Ashcraft, M. J. Kelly, J. J. Chambers, T. M. Klein, and G. N. Parsons, "Elementary reaction schemes for physical and chemical vapor deposition of transition metal oxides on silicon for high-k gate dielectric applications," *Journal of Applied Physics,* vol. 91, pp. 6173-6180, 2002.

[10] A. Dimoulas, G. Vellianitis, A. Travlos, V. Ioannou-Sougleridis, and A. G. Nassiopoulou, "Structural and electrical quality of the high-k dielectric Y_2O_3 on Si (001): dependence on growth parameters," *Journal of Applied Physics,* vol. 92, pp. 426-431, 2002.

[11] A. Sawa, "Resistive switching in transition metal oxides," *Materials Today,* vol. 11, pp. 28-36, 2008.

[12] C. An, S. Haddad, W. Yi-Ching, F. Tzu-Ning, L. Zhida, S. Avanzino, *et al.*, "Non-volatile resistive switching for advanced memory applications," in *Electron Devices Meeting, 2005. IEDM Technical Digest. IEEE International*, 2005, pp. 746-749.

[13] W. Johnson, G. Perlegos, A. Renninger, G. Kuhn, and T. Ranganath, "A 16Kb electrically erasable nonvolatile memory," in *Solid-State Circuits Conference. Digest of Technical Papers. 1980 IEEE International*, 1980, pp. 152-153.

[14] K. Jinbong and L. Kwyro, "Three-transistor one-time programmable (OTP) ROM cell array using standard CMOS gate oxide antifuse," *IEEE Electron Device Letters,* vol. 24, pp. 589-591, 2003.

[15] T. Mikolajick, M. Salinga, M. Kund, and T. Kever, "Nonvolatile memory concepts based on resistive switching in inorganic materials," *Advanced Engineering Materials,* vol. 11, 2009.

[16] (2010). *International Technology Roadmap for Semiconductors 2010 Edition*

[17] B. N. Engel, J. Akerman, B. Butcher, R. W. Dave, M. DeHerrera, M. Durlam, *et al.*, "A 4-Mb toggle MRAM based on a novel bit and switching method," *Magnetics, IEEE Transactions on,* vol. 41, pp. 132-136, 2005.

[18] T. Kawahara, R. Takemura, K. Miura, J. Hayakawa, S. Ikeda, Y. Lee, *et al.*, "2Mb spin-transfer torque RAM (SPRAM) with bit-by-bit bidirectional current write and parallelizing-direction current read," in *Solid-State Circuits Conference, 2007. ISSCC 2007. Digest of Technical Papers. IEEE International*, 2007, pp. 480-617.

[19] K. Kohary and C. D. Wright, "Electric field induced crystallization in phase-change materials for memory applications," *Applied Physics Letters,* vol. 98, pp. 223102-3, 2011.

[20] S. Chilstedt, C. Dong, and D. Chen, "Design and evaluation of a carbon nanotube-based programmable architecture," *International Journal of Parallel Programming,* vol. 37, pp. 389–416, 2009.

[21] A. Knoll, P. Bächtold, J. Bonan, G. Cherubini, M. Despont, U. Drechsler, *et al.*, "Integrating nanotechnology into a working storage device," *Microelectronic Engineering,* vol. 83, pp. 1692-1697, 2006.

[22] L. Guo, E. Leobandung, and S. Y. Chou, "A silicon single-electron transistor memory operating at room temperature," *Science,* vol. 275, 1996.

[23] J. Borghetti, Z. Li, J. Straznicky, X. Li, D. A. A. Ohlberg, W. Wu, *et al.*, "A hybrid nanomemristor/transistor logic circuit capable of self-programming," *Proceedings of the National Academy of Sciences,* vol. 106, pp. 1699-1703, 2009.

[24] P. Peng, D. Xie, Y. Yang, Y. Zang, X. Gao, C. Zhou, *et al.*, "Resistive switching behavior in diamond-like carbon films grown by pulsed laser deposition for resistance switching random access memory application," *Journal of Applied Physics,* vol. 111, pp. 084501-4, 2012.

[25] F. Zhuge, W. Dai, C. L. He, A. Y. Wang, Y. W. Liu, M. Li, *et al.*, "Nonvolatile resistive switching memory based on amorphous carbon," *Applied Physics Letters,* vol. 96, pp. 163505-3, 2010.

[26] H. Seul Ki, K. Ji Eun, K. Sang Ouk, C. Sung-Yool, and B. Jin Cho, "Flexible resistive switching memory device based on graphene oxide," *IEEE Electron Device Letters,* vol. 31, pp. 1005-1007, 2010.

[27] A. Mehonic, S. Cueff, M. Wojdak, S. Hudziak, O. Jambois, C. Labbe, *et al.*, "Resistive switching in silicon suboxide films," *Journal of Applied Physics,* vol. 111, pp. 074507-9, 2012.

[28] A. V. Shaposhnikov, T. V. Perevalov, V. A. Gritsenko, C. H. Cheng, and A. Chin, "Mechanism of GeO_2 resistive switching based on the multi-phonon assisted tunneling between traps," *Applied Physics Letters,* vol. 100, pp. 243506-4, 2012.

[29] T. W. Hickmott, "Low-Frequency negative resistance in thin anodic oxide films," *Journal of Applied Physics,* vol. 33, pp. 2669-2682, 1962.

[30] J. F. GIBBONS and W. E. BEADLE, "Switching properties of thin NiO films," *Solid-State Electronics,* vol. 7, pp. 785-797, 1964.

[31] A. Beck, J. G. Bednorz, C. Gerber, C. Rossel, and D. Widmer, "Reproducible switching effect in thin oxide films for memory applications," *Applied Physics Letters,* vol. 77, pp. 139-141, 2000.

[32] D. B. Strukov, G. S. Snider, D. R. Stewart, and R. S. Williams, "The missing memristor found," *Nature,* vol. 453, pp. 80-83, 2008.

[33] L. O. CHUA, "Memristor-The missing circuit element," *IEEE Transactions on Circuit Theory,* vol. 18, 1971.

[34] J. J. Yang, D. B. Strukov, and D. R. Stewart, "Memristive devices for computing," *Nature Nanotechnology,* vol. 8, 2012.

[35] D. B. Strukov, "Nanotechnology: Smart connections," *Nature,* vol. 476, 2011.

[36] R. Waser, R. Dittmann, G. Staikov, and K. Szot, "Redox-based resistive switching memories – nanoionic mechanisms, prospects, and challenges," *Advanced Materials,* vol. 21, pp. 2632-2663, 2009.

[37] S. Menzel, U. Bottger, and R. Waser, "Simulation of multilevel switching in electrochemical metallization memory cells," *Journal of Applied Physics,* vol. 111, pp. 014501-5, 2012.

[38] J. J. Yang, M. D. Pickett, X. Li, A. A. OhlbergDouglas, D. R. Stewart, and R. S. Williams, "Memristive switching mechanism for metal/oxide/metal nanodevices," *Nature Nanotechnology,* vol. 3, pp. 429-433, 2008.

[39] J. H. Hur, M.-J. Lee, C. B. Lee, Y.-B. Kim, and C.-J. Kim, "Modeling for bipolar resistive memory switching in transition-metal oxides," *Physical Review B,* vol. 82, p. 155321, 2010.

[40] C. H. Yang, J. Seidel, S. Y. Kim, P. B. Rossen, P. Yu, M. Gajek, *et al.*, "Electric modulation of conduction in multiferroic Ca-doped $BiFeO_3$ films," *Nature Materials,* vol. 8, pp. 485-493, 2009.

[41] K. M. Kim, D. S. Jeong, and C. S. Hwang, "Nanofilamentary resistive switching in binary oxide system; a review on the present status and outlook," *Nanotechnology,* vol. 22, 2011.

[42] W. Wu, K. H. Wong, and C. L. Choy, "Epitaxial growth of $SrTiO_3$ films with different orientations on TiN buffered Si(001) by pulsed laser deposition," *Thin Solid Films,* vol. 360, pp. 103-106, 2000.

[43] F. M. PONTES, E. J. H. LEE, E. R. LEITE, E. LONGO, and J. A. VARELA, "High dielectric constant of $SrTiO_3$ thin films prepared by chemical process," *Journal of Materials Science* vol. 35, pp. 4783 – 4787, 2000.

[44] S. W. Lee, O. S. Kwon, J. H. Han, and C. S. Hwang, "Enhanced electrical properties of $SrTiO_3$ thin films grown by atomic layer deposition at high temperature for dynamic random access memory applications," *Applied Physics Letters,* vol. 92, pp. 222903-3, 2008.

[45] K. A. Muller and H. Burkard, "$SrTiO_3$: An intrinsic quantum paraelectric below 4 K," *Physical Review B,* vol. 19, 1979.

[46] R. C. Neville, B. Hoeneisen, and C. A. Mead, "Permittivity of strontium titanate," *Journal of Applied Physics,* vol. 43, pp. 2124-2131, 1972.

[47] R. Muenstermann, T. Menke, R. Dittmann, and R. Waser, "Coexistence of filamentary and homogeneous resistive switching in Fe-doped $SrTiO_3$ thin-tilm memristive devices," *Advanced Materials,* vol. 22, 2010.

[48] C. Lenser, A. Kuzmin, J. Purans, A. Kalinko, R. Waser, and R. Dittmann, "Probing the oxygen vacancy distribution in resistive switching Fe-$SrTiO_3$ metal-insulator-metal-structures by micro-x ray absorption near-edge structure," *Journal of Applied Physics,* vol. 111, pp. 076101-3, 2012.

[49] Y. Watanabe, J. G. Bednorz, A. Bietsch, C. Gerber, D. Widmer, A. Beck, *et al.*, "Current-driven insulator-conductor transition and nonvolatile memory in chromium-doped $SrTiO_3$ single crystals," *Applied Physics Letters,* vol. 78, pp. 3738-3740, 2001.

[50] S. Hirose, A. Nakayama, and H. Niimi, "Fabrication and characterization of colossal electroresistance chip devices composed of polycrystalline lanthanum-doped strontium titanate and palladium electrodes," *Journal of the American Ceramic Society,* vol. 91, pp. 478–484, 2008.

[51] X. B. Yan, J. Yin, Z. G. Liu, and X. Y. Xia, "Studies on the reset power needed for the unipolar resistive switching in amorphous $SrTiO_{3-\delta}$ films induced by electrical pulse," *Physics Letters A,* vol. 375, pp. 3599-3603, 2011.

[52] A. Dimoulas, G. Mavrou, G. Vellianitis, E. Evangelou, N. Boukos, M. Houssa, *et al.*, "HfO_2 high-kappa gate dielectrics on Ge (100) by atomic oxygen beam deposition," *Applied Physics Letters,* vol. 86, pp. 032908-3, 2005.

[53] H. B. Profijt, S. E. Potts, M. C. M. v. d. Sanden, and W. M. M. Kesselsa, "Plasma-assisted atomic layer deposition: basics, opportunities, and challenges," *Journal of Vacuum Science and Technology A,* vol. 29, 2011.

[54] S. Chakraborty, M. K. Bera, C. K. Maiti, and P. K. Bose, "Effects of annealing on the electrical properties of TiO_2 films deposited on Ge-rich SiGe substrates," *Journal of Applied Physics,* vol. 100, pp. 023706-6, 2006.

[55] M. Orita, H. Ohta, H. Hiramatsu, M. Hirano, S. Den, M. Sasaki, *et al.*, "Pulsed laser deposition system for producing oxide thin films at high temperature," *Review of Scientific Instruments,* vol. 72, pp. 3340-3343, 2001.

[56] P. J. Kelly and R. D. Arnell, "Magnetron sputtering: a review of recent developments and applications," *Vacuum,* vol. 56, pp. 159-172, 2000.

[57] S. Ferrari, S. Spiga, C. Wiemer, M. Fanciulli, and A. Dimoulas, "Germanium diffusion during HfO_2 growth on Ge by molecular beam epitaxy," *Applied Physics Letters,* vol. 89, pp. 122906-3, 2006.

[58] G. Dilliway, M. Oliver, K. Kwa, Z. Zhou, S. Mojarad, J. Goss, *et al.*, "Remote plasma atomic layer deposition of strontium titanate films using $Sr(iPr_3Cp)_2$ and $Ti(OiPr)_4$," *Meeting Abstracts,* vol. MA2011-01, pp. 1379-1379, 2011.

[59] C. R. CROWBLL, "The Richardson constant for thermionic emission in Schottky barrier diodes," *Solid-State Electronics,* vol. 8, 1965.

[60] S. Simeonov, I. Yourukov, E. Kafedjiiska, and A. Szekeres, "Inter-trap tunnelling in thin SiO_2 films," *physica status solidi,* vol. 201, pp. 2966–2979, 2004.

[61] S. K. Kim, G.-J. Choi, S. Y. Lee, M. Seo, S. W. Lee, J. H. Han, *et al.*, "Al-Doped TiO_2 Films with Ultralow Leakage Currents for Next Generation DRAM Capacitors," *Advanced Materials,* vol. 20, 2008.

[62] B. Miao, R. Mahapatra, N. Wright, and A. Horsfall, "The role of carbon contamination in voltage linearity and leakage current in high-k metal-insulator-metal capacitors," *Journal of Applied Physics,* vol. 104, pp. 054510-8, 2008.

[63] J. R. Yeargan and H. L. Taylor, "The Poole-Frenkel Effect with Compensation Present," *Journal of Applied Physics,* vol. 39, pp. 5600-5604, 1968.

[64] A. I. Kingon, J. P. Maria, and S. K. Streiffer, "Alternative dielectrics to silicon dioxide for memory and logic devices," *Nature,* vol. 406, pp. 1032-1038, 2000.

[65] B. J. Choi, D. S. Jeong, S. K. Kim, C. Rohde, S. Choi, J. H. Oh, *et al.*, "Resistive switching mechanism of TiO_2 thin films grown by atomic-layer deposition," *Journal of Applied Physics,* vol. 98, p. 033715, 2005.

[66] D. H. Kwon, K. M. Kim, J. H. Jang, J. M. Jeon, M. H. Lee, G. H. Kim, *et al.*, "Atomic structure of conducting nanofilaments in TiO_2 resistive switching memory," *Nature Nanotechnology,* vol. 5, pp. 148-153, 2010.

[67] S. Akihito, "Resistive switching in transition metal oxides," *Materials Today,* vol. 11, pp. 28-36, 2008.

[68] R. Muenstermann, T. Menke, R. Dittmann, S. Mi, C. Jia, D. Park, *et al.*, "Correlation between growth kinetics and nanoscale resistive switching

properties of $SrTiO_3$ thin films," *Journal of Applied Physics,* vol. 108, p. 124504, 2010.

[69] E. Peter and T. Reji, "Electrical properties of $(Ba,Sr)TiO_3$ thin films revisited: The case of chemical vapor deposited films on Pt electrodes," *Journal of Applied Physics,* vol. 99, p. 114108, 2006.

[70] H. Yang, M. Jain, N. A. Suvorova, H. Zhou, H. M. Luo, D. M. Feldmann, *et al.,* "Temperature-dependent leakage mechanisms of $Pt/BiFeO_3/SrRuO_3$ thin film capacitors," *Applied Physics Letters,* vol. 91, p. 072911, 2007.

[71] Y. Seo, S. Lee, I. An, C. Song, and H. Jeong, "Conduction mechanism of leakage current due to the traps in ZrO_2 thin film," *Semiconductor Science and Technology,* vol. 24, p. 115016, 2009.

[72] J. Sun, X. J. Zheng, W. Yin, M. H. Tang, and W. Li, "Space-charge-limited leakage current in high dielectric constant and ferroelectric thin films considering the field-dependent permittivity," *Applied Physics Letters,* vol. 97, p. 242905, 2010.

[73] A. Paskaleva, M. Lemberger, A. J. Bauer, and L. Frey, "Implication of oxygen vacancies on current conduction mechanisms in $TiN/Zr_{1-x}Al_xO_2/TiN$ metal-insulator-metal structures," *Journal of Applied Physics,* vol. 109, p. 076101, 2011.

[74] D. Seong, M. Jo, D. Lee, and H. Hwang, "HPHA effect on reversible resistive switching of Pt/Nb-Doped $SrTiO_3$ Schottky junction for nonvolatile memory application," *Electrochemical and Solid-State Letters,* vol. 10, pp. H168-H170, 2007.

[75] X. Liu, K. P. Biju, J. Lee, J. Park, S. Kim, S. Park, *et al.,* "Parallel memristive filaments model applicable to bipolar and filamentary resistive switching," *Applied Physics Letters,* vol. 99, p. 113518, 2011.

[76] W. Jiang, M. Noman, Y. M. Lu, J. A. Bain, P. A. Salvador, and M. Skowronski, "Mobility of oxygen vacancy in $SrTiO_3$ and its implications for oxygen-migration-based resistance switching," *Journal of Applied Physics,* vol. 110, pp. 034509-8, 2011.

[77] K. C. Chiang, C. H. Cheng, H. C. Pan, C. N. Hsiao, C. P. Chou, A. Chin, *et al.,* "High-temperature leakage improvement in Metal/Insulator/Metal capacitors by work-function tuning," *Electron Device Letters, IEEE,* vol. 28, pp. 235-237, 2007.

[78] H. L. Mosbacker, C. Zgrabik, M. J. Hetzer, A. Swain, D. C. Look, G. Cantwell, *et al.,* "Thermally driven defect formation and blocking layers at metal-ZnO interfaces," *Applied Physics Letters,* vol. 91, p. 072102, 2007.

[79] D. Manger, B. Kaczer, N. Menou, S. Clima, D. J. Wouters, V. V. Afanas'ev, *et al.*, "Comprehensive investigation of trap-assisted conduction in ultra-thin $SrTiO_3$ layers," *Microelectronic Engineering,* vol. 86, pp. 1815-1817, 2009.

[80] C. Hwang, B. Lee, C. Kang, J. Kim, K. Lee, H. Cho, *et al.*, "A comparative study on the electrical conduction mechanisms of $(Ba_{0.5}Sr_{0.5})TiO_3$ thin films on Pt and IrO_2 electrodes," *Journal of Applied Physics,* vol. 83, p. 3703, 1998.

[81] C. Lit Ho, M. Kanad, C. H. d. Groot, and K. Reinhard, "The structural and electrical properties of thermally grown TiO_2 thin films," *Journal of Physics: Condensed Matter* vol. 18, p. 645, 2006.

[82] R. Mahapatra, A. K. Chakraborty, N. Poolamai, A. Horsfall, S. Chattopadhyay, N. G. Wright, *et al.*, "Leakage current and charge trapping behavior in TiO_2/SiO_2 high-k gate dielectric stack on 4H-SiC substrate," *Journal of Vacuum Science and Technology B* vol. 25, p. 217, 2007.

[83] L. Sang Woon, H. Jeong Hwan, and H. Cheol Seong, "Electronic conduction ,echanism of $SrTiO_3$ thin film grown on Ru electrode by atomic layer deposition," *Electrochemical and Solid-State Letters,* vol. 12, pp. G69-G71, 2009.

[84] D. S. Shang, J. R. Sun, L. Shi, J. Wang, Z. H. Wang, and B. G. Shen, "Electronic transport and colossal electroresistance in $SrTiO_3$:Nb-based Schottky junctions," *Applied Physics Letters,* vol. 94, p. 052105, 2009.

[85] E. Lee, M. Gwon, D.-W. Kim, and H. Kim, "Resistance state-dependent barrier inhomogeneity and transport mechanisms in resistive-switching Pt/$SrTiO_3$ junctions," *Applied Physics Letters,* vol. 98, pp. 132905-3, 2011.

[86] T. Fujii, M. Kawasaki, A. Sawa, Y. Kawazoe, H. Akoh, and Y. Tokura, "Electrical properties and colossal electroresistance of heteroepitaxial $SrRuO_3/SrTi_{1-x}Nb_xO_3$ Schottky junctions," *Physical Review B,* vol. 75, p. 165101, 2007.

[87] M. Seo, S. H. Rha, S. K. Kim, J. H. Han, W. Lee, S. Han, *et al.*, "The mechanism for the suppression of leakage current in high dielectric TiO_2 thin films by adopting ultra-thin HfO_2 films for memory application," *Journal of Applied Physics,* vol. 110, pp. 024105-7, 2011.

[88] D. A. Muller, N. Nakagawa, A. Ohtomo, J. L. Grazul, and H. Y. Hwang, "Atomic-scale imaging of nanoengineered oxygen vacancy profiles in $SrTiO_3$," *Nature,* vol. 430, pp. 657-661, 2004.

[89] M. Marques, L. Teles, V. Anjos, L. Scolfaro, J. Leite, V. Freire, *et al.*, "Full-relativistic calculations of the $SrTiO_3$ carrier effective masses and complex dielectric function," *Applied Physics Letters,* vol. 82, p. 3074, 2003.

[90] G. W. Dietz, M. Schumacher, R. Waser, S. K. Streiffer, C. Basceri, and A. I. Kingon, "Leakage currents in $Ba_{0.7}Sr_{0.3}TiO_3$ thin films for ultrahigh-density dynamic random access memories," *Journal of Applied Physics,* vol. 82, pp. 2359-2364, 1997.

[91] A. Gushterov and S. Simeonov, "Extraction of trap-assisted-tunneling parameters by graphical method in thin n-Si/SiO_2 structures," *Journal of Optoelectronics and Advanced Materials,* vol. 7, pp. 1389-1393, 2005.

[92] J. Carrasco, F. Illas, N. Lopez, E. A. Kotomin, Y. F. Zhukovskii, R. A. Evarestov, *et al.*, "First-principles calculations of the atomic and electronic structure of F centers in the bulk and on the (001) surface of $SrTiO_3$," *Physical Review B,* vol. 73, p. 064106, 2006.

[93] E. A. Kotomin, V. Alexandrov, D. Gryaznov, R. A. Evarestovd, and J. Maiera, "Confinement effects for ionic carriers in $SrTiO_3$ ultrathin films: first-principles calculations of oxygen vacancies," *Physical Chemistry Chemical Physics,* vol. 13, pp. 923–926, 2011.

[94] B. P. Andreasson, M. Janousch, U. Staub, and G. I. Meijer, "Spatial distribution of oxygen vacancies in Cr-doped $SrTiO_3$ during an electric-field-driven insulator-to-metal transition," *Applied Physics Letters,* vol. 94, p. 013513, 2009.

[95] A. Kalabukhov, R. Gunnarsson, J. Börjesson, E. Olsson, T. Claeson, and D. Winkler, "Effect of oxygen vacancies in the $SrTiO_3$ substrate on the electrical properties of the $LaAlO_3$/$SrTiO_3$ interface," *Physical Review B,* vol. 75, p. 121404, 2007.

[96] C. Park, S. H. Jeon, S. C. Chae, S. Han, B. H. Park, S. Seo, *et al.*, "Role of structural defects in the unipolar resistive switching characteristics of Pt/NiO/Pt structures," *Applied Physics Letters,* vol. 93, pp. 042102-3, 2008.

[97] K. M. Kim, B. J. Choi, and C. S. Hwang, "Localized switching mechanism in resistive switching of atomic-layer-deposited TiO_2 thin films," *Applied Physics Letters,* vol. 90, p. 242906, 2007.

[98] J. Qiu, A. Shih, W. Zhou, Z. Mi, and I. Shih, "Effects of metal contacts and dopants on the performance of ZnO-based memristive devices," *Journal of Applied Physics,* vol. 110, pp. 014513-5, 2011.

[99] C. Chen, F. Pan, Z. S. Wang, J. Yang, and F. Zeng, "Bipolar resistive switching with self-rectifying effects in Al/ZnO/Si structure," *Journal of Applied Physics,* vol. 111, pp. 013702-6, 2012.

[100] K. M. A. Salam, H. Fukuda, and S. Nomura, "Reduction of defect states of tantalum oxide thin films with additive elements," *Materials Science in Semiconductor Processing,* vol. 6, pp. 531-533, 2003.

[101] J. Crawford and P. Jacobs, "Point Defect Energies for Strontium Titanate: A Pair-Potentials Study," *Journal of Solid State Chemistry,* vol. 144, pp. 423-429, 1999.

[102] K. Eshraghian, "Evolution of Nnonvolatile resistive switching memory technologies: the related influence on hetrogeneous nanoarchitectures," *Transactions on Electrical and Electronic Materials,* vol. 11, pp. 243-248,, 2010.

[103] S. D. Ha and S. Ramanathan, "Adaptive oxide electronics: A review," *Journal of Applied Physics,* vol. 110, pp. 071101-20, 2011.

[104] M. Hasan, R. Dong, D. S. Lee, D. J. Seong, H. J. Choi, M. B. Pyun, *et al.*, "A materials approach to resistive switching memory oxides," *Journal of Semiconductor Technology and Science,* vol. 8, 2008.

[105] S. M. Sadaf, E. M. Bourim, X. Liu, S. H. Choudhury, D.-W. Kim, and H. Hwang, "Ferroelectricity-induced resistive switching in $Pb(Zr_{0.52}Ti_{0.48})O_3/Pr_{0.7}Ca_{0.3}MnO_3$/Nb-doped $SrTiO_3$ epitaxial heterostructure," *Applied Physics Letters,* vol. 100, pp. 113505-4, 2012.

[106] D. S. Jeong and C. S. Hwang, "Tunneling-assisted Poole-Frenkel conduction mechanism in HfO_2 thin films," *Journal of Applied Physics,* vol. 98, pp. 113701-6, 2005.

[107] H. M. Gupta and R. J. Van Overstraeten, "Role of trap states in the insulator region for MIM characteristics," *Journal of Applied Physics,* vol. 46, pp. 2675-2682, 1975.

[108] R. Astala and P. D. Bristowe, "Ab initio study of the oxygen vacancy in $SrTiO_3$," *Modelling and Simulation in Materials Science and Engineering,* vol. 9, pp. 415–422, 2001.

[109] S. A. Mojarad, K. S. K. Kwa, J. P. Goss, Z. Zhou, N. K. Ponon, D. J. R. Appleby, *et al.*, "A comprehensive study on the leakage current mechanisms of Pt/$SrTiO_3$/Pt capacitor," *Journal of Applied Physics,* vol. 111, pp. 014503-6, 2012.

[110] A. Sawa, T. Fujii, M. Kawasaki, and Y. Tokura, "Interface resistance switching at a few nanometer thick perovskite manganite active layers," *Applied Physics Letters,* vol. 88, pp. 232112-3, 2006.

[111] F.-C. Chiu, W.-C. Shih, and J.-J. Feng, "Conduction mechanism of resistive switching films in MgO memory devices," *Journal of Applied Physics,* vol. 111, pp. 094104-5, 2012.

[112] Y. Wu, S. Yu, B. Lee, and P. Wong, "Low-power TiN/Al_2O_3/Pt resistive switching device with sub-20 uA switching current and gradual resistance modulation," *Journal of Applied Physics,* vol. 110, pp. 094104-5, 2011.

[113] Z. Liu, P. Zhang, Y. Meng, H. Tian, J. Li, X. Pan, *et al.*, "Effect of TaO_x thickness on the resistive switching of Ta/$Pr_{0.7}Ca_{0.3}MnO_3$/Pt films," *Applied Physics Letters,* vol. 100, pp. 143506-4, 2012.

[114] M. Siddik, S. Jung, J. Park, W. Lee, S. Kim, J. Lee, *et al.*, "Thermally assisted resistive switching in $Pr_{0.7}Ca_{0.3}MnO_3$/Ti/$Ge_2Sb_2Te_5$ stack for nonvolatile memory applications," *Applied Physics Letters,* vol. 99, pp. 063501-3, 2011.

[115] S. Asanuma, H. Akoh, H. Yamada, and A. Sawa, "Relationship between resistive switching characteristics and band diagrams of TiÕ$Pr_{1-x}Ca_xMnO_3$ junctions," *Physical Review B,* vol. 80, p. 235113, 2009.

[116] Z. L. Liao, Z. Z. Wang, Y. Meng, Z. Y. Liu, P. Gao, J. L. Gang, *et al.*, "Categorization of resistive switching of metal-$Pr_{0.7}Ca_{0.3}MnO_3$-metal devices," *Applied Physics Letters,* vol. 94, pp. 253503-3, 2009.

[117] S.-L. Li, J.-L. Gang, J. Li, H.-F. Chu, and D.-N. Zheng, "Reproducible low-voltage resistive switching in a low-initial-resistance $Pr_{0.7}Ca_{0.3}MnO_3$ junction," *Journal of Physics D: Applied Physics,* vol. 41, 2008.

[118] Y. M. Lu, W. Jiang, M. Noman, J. A. Bain, P. A. Salvador, and M. Skowronski, "Thermographic analysis of localized conductive channels in bipolar resistive switching devices " *Journal of Physics D: Applied Physics,* vol. 44, 2011.

[119] H. Shima, N. Zhong, and H. Akinaga, "Switchable rectifier built with Pt/TiO_x/Pt trilayer," *Applied Physics Letters,* vol. 94, pp. 082905-3, 2009.

[120] R. Dong, D. S. Lee, M. B. Pyun, M. Hasan, H. J. Choi, M. S. Jo, *et al.*, "Mechanism of current hysteresis in reduced rutile TiO_2 crystals for resistive memory," *Applied Physics A,* vol. 93, pp. 409–414, 2008.

[121] K. Tsunoda, Y. Fukuzumi, J. R. Jameson, Z. Wang, P. B. Griffin, and Y. Nishi, "Bipolar resistive switching in polycrystalline TiO_2 films," *Applied Physics Letters,* vol. 90, pp. 113501-3, 2007.

[122] M. H. Lee, K. M. Kim, G. H. Kim, J. Y. Seok, S. J. Song, J. H. Yoon, *et al.*, "Study on the electrical conduction mechanism of bipolar resistive switching TiO_2 thin films using impedance spectroscopy," *Applied Physics Letters,* vol. 96, pp. 152909-3, 2010.

[123] G. H. Kim, J. H. Lee, J. Y. Seok, S. J. Song, J. H. Yoon, K. J. Yoon, *et al.*, "Improved endurance of resistive switching TiO_2 thin film by hourglass shaped Magnli filaments," *Applied Physics Letters,* vol. 98, pp. 262901-3, 2011.

[124] S. C. Chae, J. S. Lee, S. Kim, S. B. Lee, S. H. Chang, C. Liu, *et al.*, "Random circuit breaker network model for unipolar resistance switching," *Advanced Materials,* vol. 20, pp. 1154–1159, 2008.

[125] K. M. Kim, B. J. Choi, Y. C. Shin, S. Choi, and C. S. Hwang, "Anode-interface localized filamentary mechanism in resistive switching of TiO_2 thin films," *Applied Physics Letters,* vol. 91, pp. 012907-3, 2007.

[126] F.-W. Yang, K.-H. Chen, C.-M. Cheng, and F.-Y. Su, "Bipolar resistive switching properties in transparent vanadium oxide resistive random access memory," *Ceramics International,* 2012.

[127] S.-C. Chen, T.-C. Chang, S.-Y. Chen, C.-W. Chen, S.-C. Chen, S. M. Sze, *et al.*, "Bipolar resistive switching of chromium oxide for resistive random access memory," *Solid-State Electronics,* vol. 62, pp. 40-43, 2011.

[128] Y.-T. Tsai, T.-C. Chang, W.-L. Huang, C.-W. Huang, Y.-E. Syu, S.-C. Chen, *et al.*, "Investigation for coexistence of dual resistive switching characteristics in $DyMn_2O_5$ memory devices," *Applied Physics Letters,* vol. 99, pp. 092106-3, 2011.

[129] L.-W. Feng, C.-Y. Chang, Y.-F. Chang, W.-R. Chen, S.-Y. Wang, P.-W. Chiang, *et al.*, "A study of resistive switching effects on a thin FeO_x transition layer produced at the oxide/iron interface of TiN/SiO_2/Fe-contented electrode structures," *Applied Physics Letters,* vol. 96, pp. 052111-3, 2010.

[130] J. S. Kwak, Y. H. Do, Y. C. Bae, H. Im, and J. P. Hong, "Reproducible unipolar resistive switching behaviors in the metal-deficient CoO_x thin film," *Thin Solid Films,* vol. 518, pp. 6437-6440, 2010.

[131] L. Goux, J. G. Lisoni, M. Jurczak, D. J. Wouters, L. Courtade, and C. Muller, "Coexistence of the bipolar and unipolar resistive-switching modes in NiO

cells made by thermal oxidation of Ni layers," *Journal of Applied Physics,* vol. 107, pp. 024512-7, 2010.

[132] S. W. Ryu, Y. B. Ahn, H. J. Kim, and Y. Nishi, "Ti-electrode effects of NiO based resistive switching memory with Ni insertion layer," *Applied Physics Letters,* vol. 100, pp. 133502-4, 2012.

[133] D. Ielmini, F. Nardi, and C. Cagli, "Physical models of size-dependent nanofilament formation and rupture in NiO resistive switching memories," *Nanotechnology,* vol. 22, 2011.

[134] O. Heinonen, M. Siegert, A. Roelofs, A. K. Petford-Long, M. Holt, K. d'Aquila, *et al.*, "Correlating structural and resistive changes in Ti:NiO resistive memory elements," *Applied Physics Letters,* vol. 96, pp. 103103-3, 2010.

[135] H. D. Lee and Y. Nishi, "Reduction in reset current of unipolar NiO-based resistive switching through nickel interfacial layer," *Applied Physics Letters,* vol. 97, pp. 252107-3, 2010.

[136] G.-S. Park, X.-S. Li, D.-C. Kim, R.-J. Jung, M.-J. Lee, and S. Seo, "Observation of electric-field induced Ni filament channels in polycrystalline NiO_x film," *Applied Physics Letters,* vol. 91, pp. 222103-3, 2007.

[137] S. Seo, M. J. Lee, D. H. Seo, S. K. Choi, D. S. Suh, Y. S. Joung, *et al.*, "Conductivity switching characteristics and reset currents in NiO films," *Applied Physics Letters,* vol. 86, pp. 093509-3, 2005.

[138] R. Dong, D. S. Lee, W. F. Xiang, S. J. Oh, D. J. Seong, S. H. Heo, *et al.*, "Reproducible hysteresis and resistive switching in metal-Cu_xO-metal heterostructures," *Applied Physics Letters,* vol. 90, pp. 042107-3, 2007.

[139] S. Lee, H. Kim, D.-J. Yun, S.-W. Rhee, and K. Yong, "Resistive switching characteristics of ZnO thin film grown on stainless steel for flexible nonvolatile memory devices," *Applied Physics Letters,* vol. 95, pp. 262113-3, 2009.

[140] Z.-J. Liu, J.-Y. Gan, and T.-R. Yew, "ZnO-based one diode-one resistor device structure for crossbar memory applications," *Applied Physics Letters,* vol. 100, pp. 153503-4, 2012.

[141] X. Gao, Y. Xia, J. Ji, H. Xu, Y. Su, H. Li, *et al.*, "Effect of top electrode materials on bipolar resistive switching behavior of gallium oxide films," *Applied Physics Letters,* vol. 97, pp. 193501-3, 2010.

[142] P. Zhang, Y. Meng, Z. Liu, D. Li, T. Su, Q. Meng, *et al.*, "Impact of interfacial resistance switching on thermoelectric effect of Nb-doped $SrTiO_3$ single crystalline," *Journal of Applied Physics,* vol. 111, pp. 063702-4, 2012.

[143] X. B. Yan, Y. D. Xia, H. N. Xu, X. Gao, H. T. Li, R. Li, *et al.*, "Effects of the electroforming polarity on bipolar resistive switching characteristics of $SrTiO_3$ films," *Applied Physics Letters,* vol. 97, pp. 112101-3, 2010.

[144] J. Li, N. Ohashi, H. Okushi, T. Nakagawa, I. Sakaguchi, H. Haneda, *et al.*, "Resistance switching properties in Pt/$SrTiO_3$:Nb Schottky junctions studied by admittance spectroscopy," *Materials Science and Engineering: B,* vol. 173, pp. 216-219, 2010.

[145] s.y.wang, b. l. cheng, c. wang, s. y. dai, h. b. lu, y. l. zhou, *et al.*, "Mechanisms of asymmetric leakage current in Pt/$Ba_{0.6}Sr_{0.4}TiO_3$/Nb-$SrTiO_3$ capacitor," *Applied Physics A,* vol. 81, pp. 1265–1268, 2005.

[146] H. Kim, C. Park, S. Lee, and D.-W. Kim, "Inhomogeneous barrier and hysteretic transport properties of Pt/$SrTiO_3$ junctions," *Journal of Physics D: Applied Physics,* vol. 42, 2009.

[147] M. Hasan, R. Dong, H. J. Choi, D. S. Lee, D. J. Seong, M. B. Pyun, *et al.*, "Effect of ruthenium oxide electrode on the resistive switching of Nb-doped strontium titanate," *Applied Physics Letters,* vol. 93, pp. 052908-3, 2008.

[148] W. Shen, R. Dittmann, U. Breuer, and R. Waser, "Improved endurance behavior of resistive switching in (Ba,Sr)TiO_3 thin films with W top electrode," *Applied Physics Letters,* vol. 93, pp. 222102-3, 2008.

[149] R. Oligschlaeger, R. Waser, R. Meyer, S. Karthauser, and R. Dittmann, "Resistive switching and data reliability of epitaxial (Ba,Sr)TiO_3 thin films," *Applied Physics Letters,* vol. 88, pp. 042901-3, 2006.

[150] W. Shen, R. Dittmann, and R. Waser, "Reversible alternation between bipolar and unipolar resistive switching in polycrystalline barium strontium titanate thin films," *Journal of Applied Physics,* vol. 107, pp. 094506-4, 2010.

[151] C.-C. Lin, C.-Y. Lin, M.-H. Lin, C.-H. Lin, and T.-Y. Tseng, "Voltage-polarity-independent and high-speed resistive switching properties of V-doped $SrZrO_3$ thin films," *IEEE Transactions on Electron Devices,* vol. 54, 2007.

[152] C. Pi, Y. Ren, Z. Q. Liu, and W. K. Chim, "Unipolar memristive switching in Yttrium oxide and RESET current reduction using a Yttrium interlayer," *Electrochemical and Solid-State Letters,* vol. 15, 2012.

[153] M.-C. Wu, T.-H. Wu, and T.-Y. Tseng, "Robust unipolar resistive switching of Co nano-dots embedded ZrO_2 thin film memories and their switching mechanism," *Journal of Applied Physics,* vol. 111, pp. 014505-6, 2012.

[154] K. Jung, Y. Kim, Y. S. Park, W. Jung, J. Choi, B. Park, *et al.*, "Unipolar resistive switching in insulating niobium oxide film and probing electroforming induced metallic components," *Journal of Applied Physics,* vol. 109, pp. 054511-4, 2011.

[155] K. Jung, Y. Kim, W. Jung, H. Im, B. Park, J. Hong, *et al.*, "Electrically induced conducting nanochannels in an amorphous resistive switching niobium oxide film," *Applied Physics Letters,* vol. 97, pp. 233509-3, 2010.

[156] J. Yoon, J. Lee, H. Choi, J.-B. Park, D.-j. Seong, W. Lee, *et al.*, "Analysis of copper ion filaments and retention of dual-layered devices for resistance random access memory applications," *Microelectronic Engineering,* vol. 86, pp. 1929-1932, 2009.

[157] D. Lee, D.-j. Seong, I. Jo, F. Xiang, R. Dong, S. Oh, *et al.*, "Resistance switching of copper doped MoO_x films for nonvolatile memory applications," *Applied Physics Letters,* vol. 90, pp. 122104-3, 2007.

[158] D. U. Lee, E. K. Kim, W.-J. Cho, and Y.-H. Kim, "Resistance switching properties of In_2O_3 nanocrystals memory device with organic and inorganic hybrid structure," *Applied Physics A,* vol. 102, pp. 933–938, 2011.

[159] K. Nagashima, T. Yanagida, K. Oka, and T. Kawai, "Unipolar resistive switching characteristics of room temperature grown SnO_2 thin films," *Applied Physics Letters,* vol. 94, pp. 242902-3, 2009.

[160] Y. Ahn, S. W. Ryu, J. H. Lee, J. W. Park, G. H. Kim, Y. S. Kim, *et al.*, "Unipolar resistive switching characteristics of pnictogen oxide films: Case study of Sb_2O_5," *Journal of Applied Physics,* vol. 112, pp. 104105-10, 2012.

[161] H. F. Tian, Y. G. Zhao, X. L. Jiang, J. P. Shi, H. J. Zhang, and J. R. Sun, "Resistance switching effect in $LaAlO_3$/Nb-doped $SrTiO_3$ heterostructure," *Applied Physics A,* vol. 102, pp. 939–942, 2011.

[162] T.-M. Pan and C.-H. Lu, "Switching behavior in rare-earth films fabricated in full room temperature," *IEEE Transactions on Electron Devices,* vol. 59, 2012.

[163] T.-M. Pan and C.-H. Lu, "Forming-free resistive switching behavior in Nd_2O_3, Dy_2O_3, and Er_2O_3 films fabricated in full room temperature," *Applied Physics Letters,* vol. 99, pp. 113509-3, 2011.

[164] X. Gao, Y. Xia, B. Xu, J. Kong, H. Guo, K. Li, *et al.*, "Unipolar resistive switching behaviors in amorphous lutetium oxide films," *Journal of Applied Physics,* vol. 108, pp. 074506-5, 2010.

[165] D. Panda, C.-Y. Huang, and T.-Y. Tseng, "Resistive switching characteristics of nickel silicide layer embedded HfO_2 film," *Applied Physics Letters,* vol. 100, pp. 112901-5, 2012.

[166] M. Lanza, K. Zhang, M. Porti, M. Nafria, Z. Y. Shen, L. F. Liu, *et al.*, "Grain boundaries as preferential sites for resistive switching in the HfO_2 resistive random access memory structures," *Applied Physics Letters,* vol. 100, pp. 123508-4, 2012.

[167] H. Y. Lee, Y. S. Chen, P. S. Chen, T. Y. Wu, F. Chen, C. C. Wang, *et al.*, "Low-Power and Nanosecond Switching in Robust Hafnium Oxide Resistive Memory With a Thin Ti Cap," *IEEE Electron Device Letters,* vol. 31, pp. 44-46, 2010.

[168] M. Y. Chan, T. Zhang, V. Ho, and P. S. Lee, "Resistive switching effects of HfO_2 high-k dielectric," *Microelectronic Engineering,* vol. 85, pp. 2420-2424, 2008.

[169] S. Lee, W.-G. Kim, S.-W. Rhee, and K. Yong, "Resistance switching behaviors of hafnium oxide films grown by MOCVD for nonvolatile memory applications," *Journal of The Electrochemical Society* vol. 155, pp. H92-H96, 2008.

[170] Y. Y. Chen, G. Pourtois, C. Adelmann, L. Goux, B. Govoreanu, R. Degreave, *et al.*, "Insights into Ni-filament formation in unipolar-switching Ni/HfO_2/TiN resistive random access memory device," *Applied Physics Letters,* vol. 100, pp. 113513-4, 2012.

[171] F. De Stefano, M. Houssa, J. A. Kittl, M. Jurczak, V. V. Afanas'ev, and A. Stesmans, "Semiconducting-like filament formation in TiN/HfO_2/TiN resistive switching random access memories," *Applied Physics Letters,* vol. 100, pp. 142102-3, 2012.

[172] J. Y. Son, D. Y. Kim, H. Kim, W. J. Maeng, Y. S. Shin, and Y. H. Shin, "A HfO_2 Thin Film Resistive Switch Based on Conducting Atomic Force Microscopy," *Electrochemical and Solid-State Letters,* vol. 14, pp. H311-H313, 2011.

[173] E. A. Miranda, C. Walczyk, C. Wenger, and T. Schroeder, "Model for the Resistive Switching Effect in HfO_2 MIM Structures Based on the Transmission Properties of Narrow Constrictions," *IEEE ELECTRON DEVICE LETTERS,* vol. 31, 2010.

[174] L. Goux, P. Czarnecki, Y. Y. Chen, L. Pantisano, X. P. Wang, R. Degraeve, *et al.*, "Evidences of oxygen-mediated resistive-switching mechanism in TiN\HfO_2\Pt cells," *Applied Physics Letters,* vol. 97, pp. 243509-3, 2010.

[175] Y.-M. Kim and J.-S. Lee, "Reproducible resistance switching characteristics of hafnium oxide-based nonvolatile memory devices," *Journal of Applied Physics,* vol. 104, pp. 114115-6, 2008.

[176] H. Y. Lee, P. S. Chen, T. Y. Wu, C. C. Wang, P. J. Tzeng, C. H. Lin, *et al.*, "Electrical evidence of unstable anodic interface in Ru/HfO_x/TiN unipolar resistive memory," *Applied Physics Letters,* vol. 92, pp. 142911-3, 2008.

[177] S. M. Bishop, H. Bakhru, J. O. Capulong, and N. C. Cady, "Influence of the SET current on the resistive switching properties of tantalum oxide created by oxygen implantation," *Applied Physics Letters,* vol. 100, pp. 142111-4, 2012.

[178] Y. Yang, P. Sheridan, and W. Lu, "Complementary resistive switching in tantalum oxide-based resistive memory devices," *Applied Physics Letters,* vol. 100, pp. 203112-4, 2012.

[179] C. B. Lee, D. S. Lee, A. Benayad, S. R. Lee, M. Chang, M.-J. Lee, *et al.*, "Highly Uniform Switching of Tantalum Embedded Amorphous Oxide Using Self-Compliance Bipolar Resistive Switching," *IEEE Electron Device Letters,* vol. 32, 2011.

[180] S. Kim, K. P. Biju, M. Jo, S. Jung, J. Park, J. Lee, *et al.*, "Effect of scaling WO_x-based RRAMs on their resistive switching characteristics," *IEEE Electron Device Letters,* vol. 32, 2011.

[181] W. Shen, A. Bell, S. Karimi, and I. M. Reaney, "Local resistive switching of Nd doped $BiFeO_3$ thin films," *Applied Physics Letters,* vol. 100, pp. 133505-4, 2012.